Safeguarding Special Nuclear Material by Detecting Fast Neutrons in Liquid Scintillators

by

Jennifer Lynn Dolan

A dissertation submitted in partial fulfillment
of the requirements for the degree of
Doctor of Philosophy
(Nuclear Engineering and Radiological Sciences)
in the University of Michigan
2013

Doctoral Committee:

Associate Professor Sara A. Pozzi, Chair
Staff Scientist David L. Chichester, Idaho National Laboratory
Assistant Research Scientist Marek Flaska
Professor Zhong He
Assistant Professor David D. Wentzloff

Acknowledgements

Although my name appears on the cover of this dissertation, a great many people have contributed to its production. I owe a debt of gratitude to all of those who have made this dissertation possible. I am fortunate to have worked with the very best!

I extend my deepest gratitude to my advisor, Professor Sara Pozzi for her high expectations, leadership, guidance and inspiration. Prof. Pozzi provided me with the tools to be a strong advocate and active contributor in the field of nuclear engineering. Dr. Marek Flaska's insight and high standards of excellence have been instrumental in my success. His steadfast support, integrity, and unparalleled expertise have provided me with invaluable direction and support. It has indeed been an honor and privilege to work with Dr. David Chichester. Dr. Chichester's encouragement, understanding, and intellect guided me and gave me the opportunity and perspective to enhance my research for this dissertation and prepare me for success throughout my career. It has been my good fortune to work with many extraordinary faculty and staff in the University of Michigan's Department of Nuclear and Engineering and Radiological Sciences. Their commitment to innovation in the fast-paced, ever-changing field of nuclear engineering has inspired me and will influence the next generation of Nuclear and Radiological professionals.

I greatly value and appreciate the friendship and support of many friends through these challenging years. I would like to express my heart-felt gratitude to Alexis Poitrasson-Riviere for his unwavering patience and support. Finally, none of this would have been possible without the love of my family – my father, mother, and sister. They have been a constant source of love and strength.

This work was supported by the U.S. Department of Energy's Fuel Cycle Technologies Program, in the Material Protection, Accounting, and Control Technologies (MPACT) Campaign. Idaho National Laboratory is operated for the U.S. Department of Energy by Battelle Energy Alliance under DOE contract DE-AC07-05-ID14517. This work was also supported by the National Science Foundation and the Domestic Nuclear Detection Office of the Department of Homeland Security through the Academic

Research Initiative Award # CMMI 0938909. This research was performed under the Nuclear Forensics Graduate Fellowship Program which is sponsored by the U.S. Department of Homeland Security's Domestic Nuclear Detection Office and the U.S. Department of Defense's Defense Threat Reduction Agency.

Table of Contents

Acknowledgements ..... **ii**

List of Figures ..... **vii**

List of Tables ..... **xiii**

List of Abbreviations ..... **xv**

Chapter 1. Introduction **1**
1.1. Description of the Problem 2
1.2. Significance of This Work 2

Chapter 2. Radiation Detection Instrumentation **5**
2.1. Current Nuclear Safeguards Instrumentation 5
2.2. Neutron Detection 6
2.3. ^{3}He Neutron Detection 7
2.4. Neutron-Multiplicity Counting 7
2.5. Organic Scintillators 9

Chapter 3. MCNPX-PoliMi and MPPost Instrumentation Modeling **11**
3.1. MCNPX-PoliMi 11
3.2. MPPost: An MCPX-PoliMi Post-Processing Code 12
3.3. MPPost Software Testing and Validation 13

Chapter 4. Organic Scintillator Response **15**
4.1. Detection Mechanisms 15
4.1.1. Neutron Interactions *15*
4.1.2. Photon Interactions *16*
4.2. Digital Data Acquisition 18
4.3. Neutron and Photon Discrimination 20
4.4. Detector Efficiency 23
4.4.1. Simulated Neutron Efficiency *24*
4.4.2. Measured Neutron Efficiency *27*
4.5. Neutron Energy Spectroscopy 27
4.5.1. Pulse-Height Distributions *28*
4.5.2. Neutron-Energy-Spectrum Unfolding *31*
4.5.3. Capture-Gated Spectroscopy *35*

Chapter 5. Passive Neutron-Correlation Measurements **39**
5.1. Simulation of Passive Neutron Correlations 39

5.1.1. Simulation Results *42*
5.2. Passive Measurements of Fissile Material 43
5.2.1. Passive Measurement Configurations *43*
5.2.2. Experimental Results *44*
5.3. Validation of MCNPX-PoliMi 48
5.4. Summary and Conclusions 49

Chapter 6. Active Neutron-Correlation Measurements 51
6.1. Characterizing Uranium-Oxides with Liquid Scintillators 51
6.1.1. Description of Measured LEU *52*
6.2. Active-Interrogation Simulations 52
6.2.1. Neutron Interactions in LEU *53*
6.2.2. Models for Mass and Enrichment Studies *54*
6.3. Active-Interrogation Measurements 55
6.3.1. Data Acquisition and Analyses *55*
6.4. Uranium Mass Investigation 56
6.4.1. Simulation Results *57*
6.4.2. Experimental Results *57*
6.5. Uranium-235 Enrichment Investigation 58
6.5.1. Simulation Results *58*
6.5.2. Experimental Results *59*
6.6. Validating MCNPX-PoliMi/MPPost for Active-Interrogation Applications 59
6.7. Summary and Conclusions 62

Chapter 7. Passive Neutron-Multiplicity Measurements 63
7.1. Simulating Neutron Multiplicity 64
7.2. Measurement of Fast-Neutron Coincidence with Liquid Scintillators 65
7.2.1. Description of Plutonium-Containing Materials Measured *65*
7.2.2. Measurement System *66*
7.2.3. Measurement-Data Analysis *67*
7.3. Measurement Results and Validation of MCNPX-PoliMi/MPPost 68
7.3.1. Measured and Simulated PHDs *68*
7.3.2. Neutron Coincidence *69*
7.4. FNMC Simulations for Prototype Design 71
7.5. Summary and Conclusions 74

Chapter 8. Towards a Fast-Neutron-Multiplicity Counter Prototype 76
8.1. FNMC Prototype 76
8.2. Initial ^{252}Cf Measurement and Simulation Benchmark Tests 78
8.2.1. The FNMC's Response to Background Radiation *79*
8.2.2. FNMC PSD Performance *80*
8.2.3. Simulation Validation *83*
8.2.4. Bare FNMC ^{252}Cf Neutron Multiplicity Detection Efficiency *84*
8.3. Characterizing Plutonium-Containing Materials with the FNMC Prototype 85
8.3.1. Simulated Neutron Multiplicity *89*
8.3.2. PSD Performance *90*
8.3.3. Neutron Background Detection *92*

8.3.4. Measured Neutron Multiplicity and Simulation Validation *93*
8.3.5. FNMC Detection Efficiencies *99*
8.3.6. Characterization with PHDs *100*
8.3.7. Proposed Future Work *101*
8.3.8. Summary and Conclusions *102*

Chapter 9. Summary and Conclusions 104

Appendix A – MCNPX-PoliMi Input Files 106
FNMC PuO_2 Simulation 106
Ispra PuO_2 Pellet Simulations with the Partial FNMC 112
Ispra Mixed-Oxide Fuel Example 117
INL Mixed-Oxide Fuel Example 125

References 133

List of Figures

Fig. 2-1. Photon spectroscopy for natural uranium (0.72% ^{235}U enrichment) and 90% ^{235}U-enriched uranium [8] [9]. 6

Fig. 2-2. A Rossi-alpha distribution showing the time-dependent neutron detections after an arbitrary start event. The “Reals” are shown as “R” and the “Accidentals” as “A”. The predelay gate, prompt and delayed gates, and long delay gate are defined by “P”, “G”, and “D” respectively [8]. 9

Fig. 4-1. The relevant dominance of the three primary photon interactions with relation to the atomic number (Z) of the absorber and the photon energy in MeV [7]. 16

Fig. 4-2. a) The neutron elastic-scattering cross sections on a linear scale as a function of the neutron energy for two isotopes [8]: ^{1}H, ^{12}C , which dictate the scattering signal in organic scintillators. b) The neutron-absorption cross section on a logarithmic scale as a function of the neutron energy for ^{10}B that is doped into organic scintillation detectors to provide capture-gated detection. 17

Fig. 4-3. A depiction of the dual-pulse detection scheme used to visualize the neutron energy spectrum measured by a boron-loaded liquid scintillator. 18

Fig. 4-4. Examples of accepted waveforms from a liquid scintillation detector with pulse widths on the order of 10 ns and full data acquisition windows of 400 ns. 19

Fig. 4-5. Measured ^{137}Cs Compton continua for four gain-matched EJ-309 detectors. ... 20

Fig. 4-6. Optimized integrals for a standard charge-integration PSD method for organic liquid scintillators..... 20

Fig. 4-7. Tail integrals versus total integrals with the neutron/photon discrimination line for a bare ^{252}Cf measurement with a 7.62 cm ø by 7.62 cm EJ-309 liquid scintillator. 21

Fig. 4-8. The ratio of the tail-to-total integrals for various ranges of pulse heights from a bare ^{252}Cf measurement with a 7.62 cm ø by 7.62 cm liquid scintillator. 22

Fig. 4-9. The relationship between the tail integral and total integral of a set a pulses detected with the BC-523A detector measurement of one of the MOX samples through 5 cm of lead shielding..... 22

Fig. 4-10. The simulated energy-dependent neutron-scattering efficiency of the 7.62 cm ø by 7.62 cm (left) and 12.7 cm ø by 12.7 cm (right) EJ-309 detectors for various LO thresholds. 25

Fig. 4-11. The simulated energy-dependent neutron-scattering efficiency and neutron-capture-gated efficiency for the 12.7 cm ø by 12.7 cm BC-523A detector. 26

Fig. 4-12. a) Intrinsic neutron-scattering efficiency with a 70-keVee threshold as a function of the length of two EJ-309 detectors for 2-MeV neutrons and b)

neutron-scattering efficiency and capture-gated efficiency with a 50-keVee threshold as a function of the length of the BC-523A detector for 2-MeV neutrons. 26

Fig. 4-13. Measured intrinsic-neutron-detection efficiency for two EJ-309 detectors measured with a ^{252}Cf source. 27

Fig. 4-14. Measured neutron and photon pulse-height distributions of a MOX sample measured at INL. 29

Fig. 4-15. Measured neutron pulse-height distributions (normalized to their integral) for ^{252}Cf, plutonium metal, an Am-Be source, four MOX samples, and a set of PuO_2 pellets. 30

Fig. 4-16. Simulated neutron energy distributions, tallied on the detector faces through the 5 cm of lead shielding, for the seven neutron sources studied in this work.... 30

Fig. 4-17. Four EJ-309 liquid scintillators surrounding a 1-kg MOX sample with 30 cm spacing from the center of the source to each of the detector faces. 5 cm of lead shielding is present in front of each detector. MCNPX-PoliMi was used to simulate the measurement configuration. 32

Fig. 4-18. MCNPX-PoliMi simulated detector response for an EJ-309 liquid scintillator with a 12.7 cm ø and 12.7 cm depth. 33

Fig. 4-19. a) Simulated neutron energy distributions, tallied on the detector faces with a large binning scheme that matches the current limitations of the unfolding method and b) spectrum unfolding results obtained from measured PHDs for the five neutron sources of interest. 34

Fig. 4-20. The unfolded simulated PHD of a MOX sample compared to the simulated neutron energy distribution. 35

Fig. 4-21. A comparison of the neutron scatter PHDs from the BC-523A for the four samples presented during this study. 36

Fig. 4-22. The simulated neutron energy distributions for the samples compared in this study (left) and a comparison of the capture-gated-neutron PHDs (right). The PHDs closely follow the trends of the anticipated neutron energy distributions entering the BC-523A detector. 37

Fig. 5-1. MCNPX-PoliMi simulation of four cylindrical EJ-309 liquid scintillators surrounding a MOX fuel can. Each detector is shielded by 5 cm of lead. The MOX fuel can is supported by a 7.5-cm thick styrofoam stand. 40

Fig. 5-2. Cross-sectional view of the 90-pin MOX fuel can where the MOX fuel is modeled within the cladding (stainless steel, 0.5-mm thick) and the pins are contained by a 0.16-cm thick aluminum can. 40

Fig. 5-3. Contributions (neutron emission rates) of spontaneous-fission and (α, n) sources present in the INL MOX pins to the total neutron production of fuel types #1 and #2..... 41

Fig. 5-4. Contributions to the total neutron productions by SF and (α, n) sources present in the JRC MOX powders. 42

Fig. 5-5. a) Simulated neutron energy distributions, tallied on the fuel-pin can (maintaining the pin assembly), for 90-pins of MOX fuel in comparison to the oxygen elastic scattering cross section. b) Simulated neutron energy distribution for 90-pins of Pin#1-type MOX fuel (tallied on the fuel-pin can) broken into its individual neutron source contributions..... 43

Fig. 5-6. Four EJ-309 liquid scintillators surrounding a 90-pin MOX fuel can with 40-cm spacing from the center of the source to each of the detector faces. Five cm of lead shielding is present in front of each detector to decrease the gamma-ray count rate..... 44

Fig. 5-7. MOX fuel pins of well-known composition were packaged into two cans in known quantities. 44

Fig. 5-8. Cross-correlation curves, including all possible particle combinations, discriminated into their components through a PSD processing algorithm. Measurement performed on Pin #1 (left) and Pin #2 (right) with the detectors spaced at 40 cm from the center of the source and a 75-keVee threshold..... 45

Fig. 5-9. Comparison of neutron-neutron correlations for the two INL MOX samples.. 46

Fig. 5-10. Neutron-neutron correlations for three samples measured at the JRC facility, normalized by their known neutron emission reaction rates. 47

Fig. 5-11. Comparison of neutron-neutron correlations for the 90-degree and 180-degree correlated neutron counts from Pin #2..... 48

Fig. 5-12. Absolute comparison of simulated and measured neutron PHDs for INL MOX assemblies (left) and JRC MOX/neutron sources (right)..... 49

Fig. 5-13. Absolute comparison of neutron-neutron correlation curves for all simulated and measured detector pairs for INL MOX assemblies (left) and JRC MOX/neutron sources (right)..... 49

Fig. 6-1. Neutron-induced fission cross sections for ^{235}U and ^{238}U for fast neutrons. The ^{235}U cross section increases at thermal and epithermal energies while the ^{238}U cross section decreases significantly..... 52

Fig. 6-2. Simulated neutron-interaction probabilities from the three interrogated LEU samples..... 53

Fig. 6-3. MCNPX-PoliMi model of the five liquid scintillators (~35 cm from the center of the LEU sample) measuring induced-fission neutrons for the DT interrogation case (a) and the moderated Am-Li interrogation case (b)..... 54

Fig. 6-4. The five-detector geometry positions the liquid scintillator faces at approximately 35 cm from the top of the LEU canister. The associated particle tagged DT neutrons are emitted in the direction coming out of the page. Also shown is the moderated Am-Li source placed under the LEU canister..... 55

Fig. 6-5. PSD technique applied to a) the DT interrogated LEU-3 measurements and b) the higher photon flux of the Am-Li interrogated LEU-3 measurements where the neutron events fall above the discrimination line. 56

Fig. 6-6. a) Simulated photon and neutron TOF curves for time-tagged DT interrogation of the three LEU samples with error bars that are smaller than the data point symbols, and b) the trend of the total neutron counts with uranium mass where the LEU-2 and LEU-3 points are overlapping. 57

Fig. 6-7. a) Measured neutron TOF curves for time-tagged DT interrogation of the three LEU samples and b) the trend of the total neutron counts with uranium mass. ... 58

Fig. 6-8. a) Simulated photon-triggered neutron TOF curves for the moderated Am-Li configurations and b) the trend of the total photon-neutron correlations with U-235 enrichment..... 58

Fig. 6-9. a) Measured photon-triggered neutron TOF curves for the moderated Am-Li configurations and b) the trend of the total photon-neutron correlations with ^{235}U enrichment (with error bars smaller than that data point symbols). 59

Fig. 6-10: Measured and MCNPX-PoliMi-simulated cross-correlation distributions for a single detector pair in conjunction with a bare ^{252}Cf source. 60

Fig. 6-11. Absolute comparison of measured and simulated TOF distributions for the moderated Am-Li configurations..... 61

Fig. 7-1. The neutron-source contributions for the PuO_2 pellets (a) and MOX samples (b) measured at the JRC facility. 64

Fig. 7-2. All experimental configurations included four 7.62 cm ø x 7.62 cm liquid scintillators 20 cm from the center of the measured samples. The configuration depicted includes nine PuO_2 pellets with 0.25 cm of lead shielding present, measured with a 70 keVee LO threshold. 65

Fig. 7-3. Measured neutrons (upper region) and photons (lower region) from the shielded PuO_2 source measured at a 70 keVee light-output threshold (approximately 650 keV neutron energy deposited). A discrimination curve is shown that was used the separate neutrons from photons. 67

Fig. 7-4. Measured neutron PHDs (normalized to their integral) for ^{252}Cf, MOX, and PuO_2 pellets..... 68

Fig. 7-5. Simulated and measured ^{252}Cf PHDs (left) with an average point-by-point agreement error of 6.8% and simulated and measured PuO_2 PHDs (right) with an average point-by-point agreement error of 10.6%. Statistical errors shown on the data points are smaller than the symbols used. 69

Fig. 7-6. Relationship between simulated and measured neutron doubles rates and $^{240}Pu_{eff}$ mass. Differences listed relate the simulated and measured data while statistical error bars shown on the data points are smaller than the symbols used. 69

Fig. 7-7. Examples of FNMC models: (a) UM measurement system used in the present work based on EJ-309 liquid scintillators, (b) a full ring (12 detectors) of 7.62 cm ø by 7.62 cm EJ-309s, (c) two rings of 7.62 cm ø by 12.7 cm EJ-309s, and (d) three rings of 12.7 cm ø by 5.08 cm EJ-309s. The models include the active volume of the EJ-309s, 0.25 cm of lead shielding, and PuO_2 pellets. 71

Fig. 7-8. The trend of simulated doubles rates with plutonium mass for 21 FNMC designs. The number of detectors and the detector size were varied. Each figure

shows the response for one, two, or three detector rings where the statistical errors are smaller than the symbols used. 72

Fig. 7-9. The trend of simulated triples rates with plutonium mass for 21 FNMC designs. The number of detectors and the detector size were varied. Each figure shows the response for one, two, or three detector rings where the statistical errors are smaller than the symbols used. 72

Fig. 8-1. Measurements with the FNMC prototype, including two rings of eight 7.62 cm ø by 7.62 cm EJ-309 liquid scintillators, a) a bare ^{252}Cf fission source, and b) a bare ^{137}Cs photon source in the UM laboratory. 77

Fig. 8-2. Two CAEN V1720 12-bit, 250 MHz, 8-channel time-synchronized digitizers are connected to a Linux workstation via two optical links. 77

Fig. 8-3. Compton edge matching at 0.3 V for 100,000 photon pulses from all sixteen EJ-309 detectors with 0.0439 V (70 keVee) thresholds. 78

Fig. 8-4. Measured neutron multiplicity for measurements of ^{252}Cf #1, ^{252}Cf #2, ^{252}Cf #1 and ^{137}Cs, ^{137}Cs alone, and the UM laboratory background. 79

Fig. 8-5. a) Photon and neutron PHDs for all 16 liquid scintillators and b) neutron-multiplicity results from a 13-hour background measurement. 80

Fig. 8-6. The neutron PHDs for the measurements of ^{252}Cf and the combination of ^{252}Cf and ^{137}Cs when (a) doubles pulses at 10% of the pulse maximum and (b) 5% of the pulse maximum are cleaned. 81

Fig. 8-7. The fractional increase in the neutron PHD when a ^{137}Cs source is added to a ^{252}Cf measurement at two different intensities of pulse-pileup cleaning. 82

Fig. 8-8. Measured and simulated neutron multiplicities for two ^{252}Cf sources; statistical uncertainty error bars are included but appear smaller than the symbols that are used. 84

Fig. 8-9. (a) Linear and (b) logarithmic plots of the absolute detection efficiency for neutron singles, doubles, triples, and quadruples from ^{252}Cf, measured and simulated for two sources. 85

Fig 8-10. The sixteen-detector FNMC setup at the JRC facility in Ispra. 86

Fig. 8-11. The origin of neutron emission for a) the two MOX samples of identical isotopic composition, b) the two PM samples of similar isotopic composition, c) the PuO_2 #1, d) the PuO_2 #2, e) the PuO_2 #3, and f) the PuO_2 #4. 88

Fig. 8-12. Simulated singles, doubles, and triples for fictitious PM and PuO_2 samples of increasing $^{240}Pu_{eff}$ mass and consistent isotopic composition, based on JRC standards. Simulated results are also included for models with voided material matrices to study the effect of matrix attenuation and multiplication. 89

Fig. 8-13. Shows the optimized PSD discrimination line for 200,000 waveforms from the four measured material types with 1 cm of lead shielding: a) ^{252}Cf, b) PuO_2, c) PM, and d) MOX. 91

Fig. 8-14. Slices of the PSD tail versus total distributions plotted along the slice to find the minimum between the photon and neutron distributions. 92

Fig. 8-15. Neutron multiplicity measured from a 2.5 day background measurement, values on the plot represent the singles, doubles, and triples rates from background alone. 93

Fig. 8-16. Neutron singles (a and b), doubles (c and d), and triples (e and f) rates as a function of $^{240}Pu_{eff}$ mass measured with the FNMC with 1 cm of lead shielding for three material types: PuO_2, PM, and MOX. Two viewpoints are shown for each curve in order to focus in on the small PuO_2 and PM samples. 94

Fig. 8-17. Linear and quadratic fits to the PuO_2 doubles rate versus $^{240}Pu_{eff}$ mass data with R^2 values of 0.9945 and 0.998 respectively. 96

Fig. 8-18. The measurement time necessary to achieve 5% and 10% uncertainty on $^{240}Pu_{eff}$ mass determination with the FNMC prototype. 97

Fig. 8-19. Linear fit to four of five PuO_2 doubles rates versus $^{240}Pu_{eff}$ mass data points and the fifth point that is used for systematic uncertainty analysis. 98

Fig. 8-20. The probability of a single, double, triple, or quadruple detection event per ^{252}Cf fission event. 99

Fig. 8-21. Normalized PHDs for seven of the plutonium measurement configurations, showing oxide versus metal characterization abilities. 101

List of Tables

Table 3-1. Five parameters for the measured exponential relationship between neutron energy deposited on hydrogen and light output for two cylindrical EJ-309s owned by the DNNG. 13

Table 4-1. Atomic Composition of an EJ-309 Scintillator. The density of the material is 0.957 g/cm^3. 24

Table 4-2. Atomic Composition of a BC-523A Scintillator. The density of the material is 0.916 g/cm^3. 24

Table 4-3. Average measured pulse heights and simulated average incident neutron energies for select sources. 31

Table 4-4. Intrinsic efficiency values compared for a boron-loaded liquid scintillator (BC-523A with a 50 keVee threshold), a standard liquid scintillator (EJ-309 with a 70 keVee threshold), and an NPOD ^{3}He detector array for the ^{252}Cf and Am-Be measured samples. 38

Table 5-1. Isotopic composition of MOX fuel pins used for this work at INL [23] (age corrected to the June 2009 measurement date). 40

Table 5-2. Isotopic composition of MOX powder used at the JRC (age corrected to the June 2010 measurement date). 42

Table 5-2. Calculated neutron emission rate from spontaneous fission, measured neutron count rate, and measured correlated neutron count rate for the two MOX fuel-pin assemblies. 46

Table 5-3. Averaged differences between PHD simulated and measured values for data collected at INL and JRC. 48

Table 6-1. Material specifications for the three LEU samples studied at the JRC. 52

Table 7-1. Isotopic masses for the measured PuO_2 pellet combinations and MOX samples. 66

Table 7-2. Difference between the data points and the linear fits. 70

Table 7-3. The sensitivity of each design portrayed in Fig. 9. 73

Table 8-1. ^{252}Cf multiplicity simulation validation for two sources. 84

Table 8-2. Measured and simulated ^{252}Cf fission detection efficiency for neutron singles, doubles, and triples from two independent ^{252}Cf sources. 85

Table 8-3. The aged material composition of seven plutonium samples investigated at the JRC. 86

Table 8-4. The percent difference between simulated and measured neutron multiplicity for the nine plutonium measurement configurations and ^{252}Cf. 95

Table 8-7. The absolute total neutron detection efficiency and the absolute fission detection efficiency for singles, double, triples, and quadruples. 100

List of Abbreviations

AFP – Atoms for Peace

(α, n) – Alpha-n reaction

Am-Be – Americium Beryllium

AmO_2 – Americium Oxide

Am-Li – Americium Lithium

CCF – Cross-Correlation Function

DNNG – Detection for Nuclear Nonproliferation Group

DT – Deuterium Tritium

FNMC – Fast-Neutron-Multiplicity Counter

HLNC – High-Level Neutron Coincidence

IAEA – International Atomic Energy Agency

INL – Idaho National Laboratory

JRC – Joint Research Centre

LEU – Low-Enriched Uranium

MCNPX-PoliMi

MPPost – MCNPX-PoliMi Post-Processing Code

MOX – Mixed Oxide

NMC – Neutron-Multiplicity Counter

nn – neutron-neutron correlation (neutron double)

nnn – neutron triple

np – neutron-photon correlation

NPT – Treaty on the Nonproliferation of Nuclear Weapons

PHD – Pulse-Height Distributions

PM – Plutonium Metal

pn – photon-neutron correlation

pp – photon-photon correlation

PSD – Pulse-Shape Discrimination

PuO_2 – Plutonium Oxide

SF – Spontaneous Fission

SNM – Special Nuclear Material

TOF – Time-of-Flight

UM – University of Michigan

YAP – Yttrium Aluminum Perovskite

Chapter 1. Introduction

The extraordinary source of energy that is contained within the nuclear fission chain reaction can solve energy crises across the globe in the form of nuclear power. Unfortunately, for the same scientific reasons, nuclear fission poses a serious global threat in the form of nuclear weapons. The U.S. president Dwight D. Eisenhower gave the renowned “Atoms for Peace” (AFP) speech in 1953 to address the “fearful atomic dilemma” [1] we faced after World War II and in the development of the Cold War. Within his address, he stated that we must “find the way by which the miraculous inventiveness of man shall not be dedicated to his death, but consecrated to his life.” This speech subsequently led to the AFP program which laid the groundwork for the nuclear nonproliferation agreements we have today [2].

The AFP address called for an international body to regulate fissile material and nuclear technologies, while promoting peaceful use of fissile material through safe nuclear technologies including nuclear power production. As a result, the International Atomic Energy Agency (IAEA) was founded in 1957. By 1970, the Treaty on the Nonproliferation of Nuclear Weapons (NPT) was entered into force with the objective to prevent the spread of nuclear weapons and their technology, while encouraging the peaceful use of nuclear technology [3]. Through the NPT, today’s nuclear safeguards system was established. Nuclear safeguards are defined as the effort to prevent diversion of fissile material. Such endeavors are the responsibility of the IAEA and are supported by diplomatic and economic means.

Given the growing complexity of nuclear facilities and current proliferation threats across the world, new technologies are needed to maintain successful international safeguards efforts. Specifically, technologies that can aid direct, fast, and robust detection of fissile material diversion are crucial to this effort. Additionally, safeguards designed into new facilities will be essential to international safeguards success.

1.1. Description of the Problem

At nuclear facilities, domestically and internationally, many measurement systems used for nuclear materials' control and accountability rely on helium-3 (^{3}He) detectors. These systems depend on well-established relationships to interpret multiplicity-type measurements for verifying quantities of special nuclear material (SNM). SNM is defined by Title I of the Atomic Energy Act of 1954 as plutonium, uranium-233, or uranium enriched in isotopes uranium-233 or uranium-235. ^{3}He is ideal for neutron detection and has found its way into many areas of nuclear material control and accountability. This rare-earth isotope is primarily produced through the decay of tritium involved in nuclear weapons production. Throughout the Cold War and for almost two decades afterwards ^{3}He was viewed as waste, sold at a low rate, and thus not conserved [4]. For these reasons, a serious resource shortage has arisen, and alternatives to ^{3}He systems are urgently needed. Additionally, in the near term, the cost of current ^{3}He-based systems continues to increase as the supply cannot meet the demand.

This mission also presents the opportunity to broaden the capabilities of such measurement systems to improve current multiplicity techniques. With long dead times associated with neutron thermalization necessary in ^{3}He systems and the detector electronics, measuring advanced nuclear fuels and spent nuclear fuels with high fission rates can be a challenge. A system that operates faster has the potential to solve this problem. Development of advanced nuclear safeguards systems can solve current resource shortage problems and expand the scope of such systems to encompass a broader range of SNM.

1.2. Significance of This Work

The primary goal of this work is to design an advanced nuclear safeguards measurement system in the form of a fast-neutron-multiplicity counter (FNMC) with organic-liquid scintillators to quantify fissile material mass. With the excellent timing properties of liquid scintillators in conjunction with excellent neutron/photon pulse-shape discrimination (PSD), a multiplicity system is being designed that can perform characterization within reasonable uncertainty on gram levels of plutonium in short times. Such a system will also be less prone to detection/characterization errors for high-activity

nuclear materials. Due to the direct measurement of fast neutrons from fission, supplementary quantities related to the fission neutron's energy can also be utilized. Also, an organic-liquid scintillation multiplicity system can make use of photon and joint neutron/photon multiplicities to solve for additional unknowns.

The tools present within the Detection for Nuclear Nonproliferation Group (DNNG) for this multi-disciplinary design effort include: state-of-the-art neutron/photon PSD techniques, advances in digital data-acquisition systems, and novel data-processing systems and techniques. The efforts were focused on designing a passive low-plutonium-mass characterization system. When designing a neutron-multiplicity counter (NMC) there are a number of standard goals that need to be kept in mind. First of all, the system efficiency must be sufficient enough to measure not only neutron singles and doubles, but also triples. For traditional ^{3}He systems, 40-60 % absolute neutron-counting efficiency is a common range to aim for [5], while many systems have efficiencies on the order of 10-30% [6]. Similarly, another goal is minimizing electronic dead-time losses and detector die-away times in order to maintain an efficient system [5]. A fast neutron multiplicity system with fast liquid scintillation detectors is inherently advantageous regarding these two issues.

Next, to develop a system that can quantify plutonium mass in a wide array of material types and composition, it is important that the efficiency is consistent across a reasonable range of neutron energies [5]. Neutrons are particularly interesting as the number of neutrons emitted strongly depends on the decay type. Neutrons emitted from SNM are the result of spontaneous and induced fission events, which have quite similar neutron-energy distributions. Neutrons are also emitted from alpha-n events (α, n) which can vary significantly in neutron-energy emission. Lastly, the material matrix will self-attenuate emitted neutrons and alter the neutron energy distribution, based on the matrix's neutron scattering cross section. A fast-neutron system does not require optimized moderation for neutrons across a wide range of energies, which is an additional benefit. Liquid scintillation detectors are conveniently consistent over the range of most neutron energies from fission and (α, n) neutrons.

Throughout this work, efforts are made to present the vast capabilities of liquid scintillators. Research pursuits were concentrated on simulation and experimental studies

of various types of nuclear material with a focus on plutonium-containing samples. Investigations include efficiency studies, neutron energy spectroscopy, passive and active coincidence detection, and neutron multiplicity. Results portray the potential for liquid scintillator measurement systems to characterize SNM. This work concludes with the development of a FNMC prototype and preliminary measurement results from a variety of plutonium samples.

Chapter 2. Radiation Detection Instrumentation

2.1. Current Nuclear Safeguards Instrumentation

The implementation of nuclear safeguards in nuclear facilities depends on a multidisciplinary set of equipment. Many types of nuclear safeguards instrumentation exist, including: physical seals, video surveillance, and laser range finders. Information and data from each of these sources is compiled during facility inspections and is used to draw conclusions on compliancy with safeguards protocols and verification of facility declarations. The type of instrumentation studied in this work relies on radiation detection. Such instrumentation is designed to characterize SNM by detecting radiation emission from radioactive decay and spontaneous fission.

The most standard form of safeguards confirms or disproves the presence and type of materials from a facility's declarations. The technologies used to verify the material declarations include both destructive and nondestructive assay. Nondestructive assay is a preferred method of investigation and can include technologies based on neutron, photon, or calorimetric measurements.

Photon measurements are convenient considering radioactive decay of key isotopes in SNM emit mono-energetic characteristic photons. Many photon detectors are available that directly measure these characteristic photons into individual, completely resolved photopeaks [7]. Figure 2-1 shows a measured photon spectrum for uranium isotopes. By counting the abundance of detections in certain photopeaks, masses can be determined, and by using ratios of counts within these key photopeaks, enrichment information can be determined. The downside of photon measurements lies in the high probability of material self-shielding. Knowledge gained from such photon spectroscopy is applicable to only the outer layers of the nuclear material (this is on the order of a couple of cm for the least dense uranium materials and a fraction of a cm for uranium metals [8]). Additionally, photons have a high presence in background radiation which can lead to complexity in data analysis and a relatively high chance for errors.

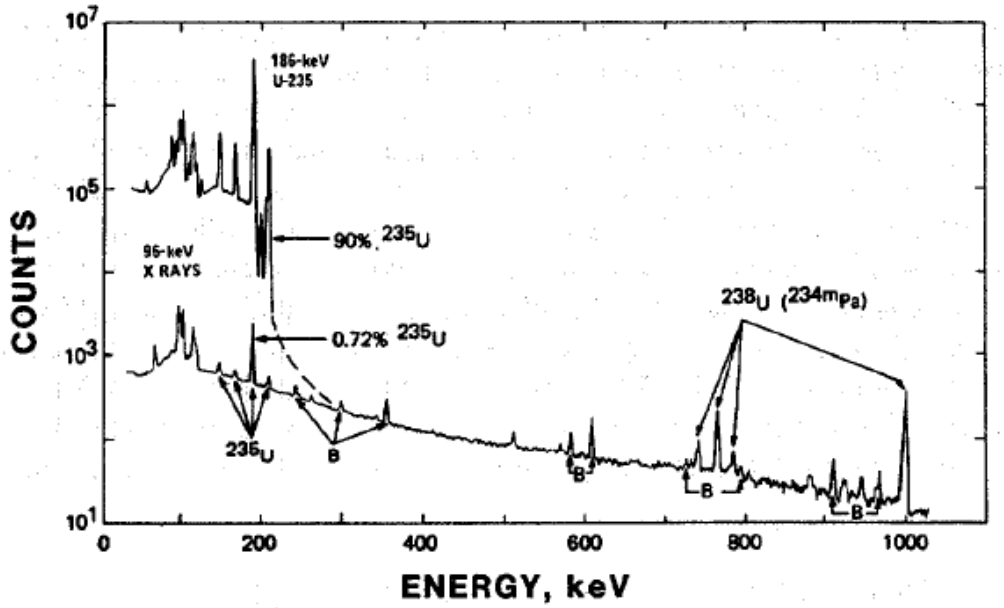

Fig. 2-1. Photon spectroscopy for natural uranium (0.72% ^{235}U enrichment) and 90% ^{235}U-enriched uranium [8] [9].

Calorimetric instrumentation measures heat emitted from the absorption of alpha particles in SNM. Alpha decay is probable with uranium and plutonium isotopes and the stopping distance for alpha particles is on the order of micrometers. The specific power of each nuclide is unique and by measuring the total power (heat) created, with knowledge of a sample's isotopic composition its mass can be quantified. Of all non-destructive material assay techniques used in safeguards, calorimetry is the most accurate and precise, considering the matrix of the material does not affect the transmission of the signal in the same way it does for photons and for neutrons. However, calorimetry requires long measurement times (on the order of 4-8 hours) and is not contained in a portable geometry and thus is not practical for most safeguards inspection scenarios [10].

All of these mentioned concepts have positive and negative attributes, but neutron measurements remain to be a leading method.

2.2. Neutron Detection

Neutrons are more penetrating than other forms of radiation and are less prevalent in radiation background and naturally occurring radioactive materials. Basic neutron counting is utilized in many nuclear nonproliferation applications, such as portal monitors, as neutron detection systems are less susceptible to false alarms caused by

background and few commonly traded goods emit neutrons. An added benefit of neutron measurements exists due to the emission of multiple neutrons spontaneously from a single reaction, which is unique to fission. Neutron-multiplicity distributions are characteristic of specific fissile isotopes. Therefore, neutron-multiplicity measurements, where the neutron multiplicity distributions are measured, have continued to rise to the top for characterizing fissile materials in nuclear accountancy applications.

2.3. ^{3}He Neutron Detection

Current neutron detecting field instrumentation utilized in domestic and international nuclear safeguards relies on ^{3}He detectors. Neutron detectors containing ^{3}He have a high efficiency for neutron detection via neutron capture when neutrons are moderated to thermal energies. Well established theory to analyze the signals (neutron coincidence or multiplicity) that come from systems containing many ^{3}He detectors can provide values such as the mass of SNM.

2.4. Neutron-Multiplicity Counting

Early characterization systems measured only the neutron rate, which was applicable to only a few types of plutonium containing materials, considering there are other neutron emitting reactions present in many plutonium containing materials. Further developments extended systems into neutron coincidence counters, which provided a method to isolate only the measurement of neutrons from fission and has been extensively applied in safeguards. With the measurement of the neutron fission rate and knowledge of the neutron-multiplicity distribution, the mass of certain plutonium isotopes can be identified.

Neutron coincidence counting has not been as applicable to domestic accountability considering that only two parameters are measured (singles and doubles) and therefore the system's neutron detection efficiency must be known. For impure plutonium samples, the neutron detection efficiency of the system may change and become a variable due to large amounts of neutron scattering or moderation within the sample. To solve this problem, assumptions must be made regarding the amount of (α, n) neutrons or the sample multiplicity. For greater accuracy and the minimization of

assumptions, neutron-multiplicity systems were developed that provide three measured parameters: singles, doubles, and triples. With a neutron-multiplicity system, the goal is to be able to correctly characterize any nuclear fuel cycle material without any knowledge of the material's matrix. [5]

Currently available multiplicity systems are categorized based on the range of plutonium mass they are designed to quantify. For lower masses of plutonium (0.1 to 500 g of plutonium) low-level inventory sample coincidence counters are available from companies like Canberra. High-level systems measure up to several kilograms of plutonium. Both low and high level systems contain just fewer than twenty ^{3}He tubes. These systems rely on spontaneous fission from the even numbered isotopes of plutonium. Similar systems, such as active-well coincidence counters, can quantify uranium as well, but require a neutron active-interrogation source and more than twice as many ^{3}He tubes. Other systems are designed to measure specific nuclear fuels such as neutron coincidence collars (PWR, BWR, CANDU assemblies), fast breeder reactor subassembly counters (single or groups of fast breeder fuel pins), and plutonium scrap counters (impure plutonium samples or mixed-oxide fuels). A FNMC described and discussed in this report is applicable for all of these measurement scenarios [6].

A common method for identifying correlated events is through shift-register circuits based on the concept of a Rossi-alpha distribution [5]. The Rossi-alpha distribution, shown in Fig. 2-2, is the time distribution of events that occur after a randomly chosen start event. This distribution will be uniform with time if only uncorrelated events are detected; therefore it will have features when correlated events are present. The distribution is defined by the constant uncorrelated events plus the exponentially decaying "Reals" events. Time gates are then defined to isolate the "Reals + Accidentals" portion and the "Accidentals" portion of the distribution. The "Reals + Accidentals" gate will be on the order of tens of microseconds, and then there will be a long delay (on the order of thousands of micro-seconds) before the "Accidentals" gate is opened for a time more similar to the initial gate [5]. An actual measured distribution will not increase exponentially as you take the limit to zero, due to pulse pile-up and electronic dead-time effects [5]. Therefore, a "pre-delay" time gate is also specified to correct for these limiting effects.

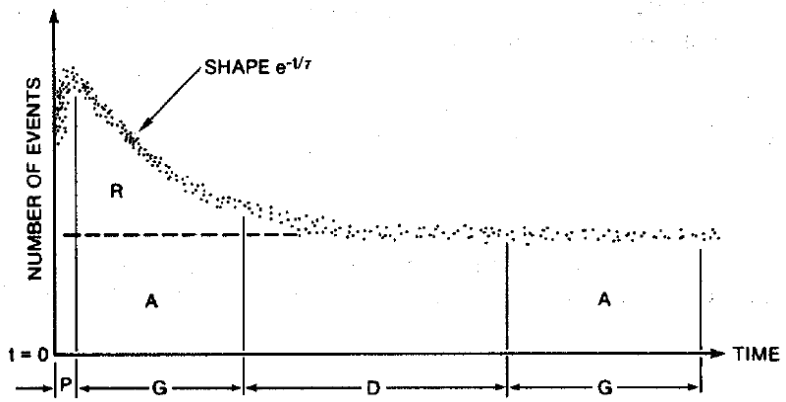

Fig. 2-2. A Rossi-alpha distribution showing the time-dependent neutron detections after an arbitrary start event. The "Reals" are shown as "R" and the "Accidentals" as "A". The predelay gate, prompt and delayed gates, and long delay gate are defined by "P", "G", and "D" respectively [8].

Identification of only the "Reals" leads to the indication of the multiplicity distribution and furthermore the fission rate, which is necessary to eventually determine the plutonium mass [5]. Specialized electronics exist to take the mentioned stream of pulses and isolate the mentioned time-gates to identify the neutron-multiplicity distributions for both the "Reals + Accidentals" and "Accidentals" gates [5]. The result of analyzing and unfolding both sets of data is the singles, doubles, and triples values needed for eventual mass quantification [5]. A FNMC can directly provide these three parameters without the circuitry and unfolding.

2.5. Organic Scintillators

Organic liquid scintillators are not traditionally used in the nuclear safeguards field due a variety of reasons. These detectors are sensitive to both neutrons and photons and have reasonable efficiency over the energy range of interest (500 keV to 10 MeV) for fission neutron detection [7]. Additionally, organic scintillators and photo-multiplier tubes (needed to correctly amplify the light created in the scintillator) have fast response times (within 1 ns) which are good for SNM characterization applications. The neutron absorption cross section for ^{3}He rivals all other neutron interaction cross sections that are easily accessible for neutron detectors; therefore it previously was not necessary to innovate measurements systems utilizing new neutron detectors. Additionally, organic scintillators had insufficient photon discrimination, challenging toxicity, and low flashpoint in some cases.

Detector developments have improved the fieldability of liquid scintillators by raising their flash-point temperature. Technological developments in digital data acquisition electronics has allowed more detailed data analysis and improved neutron and photon discrimination. In today's world with the rising need for novel nuclear safeguards instrumentation, organic scintillation detectors are a promising candidate for innovative neutron measurement systems. The remainder of this work will study organic scintillators in detail and discuss their applicability for use in nuclear safeguards and nuclear nonproliferation applications.

Chapter 3. MCNPX-PoliMi and MPPost Instrumentation Modeling

Research and development in the area of nuclear safeguards instrumentation often requires the use of simulation tools. Testing of potential SNM characterization instrumentation components (radiation detectors) and data analysis techniques is difficult, expensive, and sometimes practically impossible due to the sensitivity of the materials that must be measured. Therefore, having a sound simulation package that can accurately replicate instrumentation response is paramount. Through detailed testing and validation I have found MCNPX-PoliMi [11] (a Monte Carlo code) and MPPost [12] (an MCNPX-PoliMi post-processing code) to be essential in liquid-organic-scintillator instrumentation research and development.

3.1. MCNPX-PoliMi

Many Monte Carlo simulations of nuclear processes utilize interaction physics in conjunction with stochastic particle transport. Examples are the MCNP codes. However, MCNP does not correctly incorporate the correlated particle detection required in several SNM-characterization applications. MCNPX-PoliMi is a modified version of the MCNPX code developed in order to obtain time-correlated quantities – specifically the correlation between neutron interactions and their consequent photon production. MCNPX-PoliMi utilizes a unique event-by-event modeling technique that uses analog physics to simulate physical reality in a correct manner.

The use of organic scintillation detectors were investigated with MCNPX-PoliMi and MPPost for several nuclear safeguards applications [13]. Both MCNPX-PoliMi and MPPost are available through the Radiation Safety Information Computation Center at Oak Ridge National Laboratory [11]. The design process to develop nuclear safeguards instrumentation is further expedited with the UM parallelized version of MCNPX-PoliMi coupled with UM advanced computing resources.

MCNPX-PoliMi is an ideal tool for designing neutron detection systems (specifically regarding neutron multiplicity) due to its: capability of realistically

simulating correlated source events, detailed particle interaction output, and availability of SNM sources with accurately sampled energy, number of particles emitted, and angular distributions. MCNPX-PoliMi incorporates the ability of simulating all standard MCNP sources with additional custom sources. These novel sources (commonly found in SNM) include spontaneous-fission distributions with specific multiplicity distributions for ^{238}U, ^{238}Pu, ^{240}Pu, ^{242}Pu, ^{242}Cm, and ^{244}Cm. Additionally, (α, n) distributions are source options for samples involving plutonium isotopes in oxides: ^{238}Pu, ^{239}Pu, ^{240}Pu, and ^{241}Am [11].

It is important that the physics of particle emission (specifically fission) are accurate when modeling coincidence/multiplicity measurements [13]. MCNPX-PoliMi incorporates neutron and photon multiplicity distributions with correlated neutron and photon production [11]. After the production of all source particles, detailed interaction information on an event-by event basis is recorded within all volumes of interest (typically detectors). This detailed information is then processed to develop detector and measurement system response.

3.2. MPPost: An MCPX-PoliMi Post-Processing Code

MPPost (an MCNPX-PoliMi post-processing code) processes the MCNPX-PoliMi data file into both individual detector and total system design responses. MPPost requires the data output file from MCNPX-PoliMi and the definition of various detector and measurement system parameters. For an organic liquid scintillation detector system, some of these parameters include: energy deposition to light-output conversion functions, detector pulse generation time, detection thresholds, dead-times, and coincidence time windows. The measured relationship for neutron energy deposition (E_p in MeV) and detector light output (LO in MeVee) is given in Eq. 3-1 with a, b, c, and d dependent on the detector type [14].

$$\boldsymbol{LO = aE_p - \ b\left(1 - e^{c(E_p)^d}\right)} \tag{3-1}$$

For the liquids used throughout this work, values are shown in Table 3-1. MPPost uses the above LO relationship to create “pulse heights” in the detector. For example, to create a single neutron pulse, the energy deposition for each neutron interaction is converted to light using Eqn. 3-1, and all the light created within the given pulse

generation time (pulse rise time) (~10 ns for the liquid scintillators) is summed up into a single light pulse. If the amount of light is above the specified keVee threshold and below the upper limit of the data acquisition then the pulse is accepted and tallied towards various requested outputs. The order of scattering events on hydrogen (H) and carbon (C) within the organic material (H-H-C or H-C-H for example) affect the amount of light collected in each pulse because neutron interactions on carbon transfer less energy and emit a very small amount of light; for this reason MCNPX-PoliMi's event-by-event simulation methodology is important for accurate pulse reproduction. Outputs from MPPost include pulse-height distributions (PHDs), correlated particle analysis such as time-of-flight (TOF) and cross-correlation functions (CCFs), and neutron and photon multiplicities. The neutron multiplicity algorithm takes into account data acquisition dead times and gives results for multiples measured within a specified time window.

Table 3-1. Five parameters for the measured exponential relationship between neutron energy deposited on hydrogen and light output for two cylindrical EJ-309s owned by the DNNG.

	a	b	c	d
7.62 cm ø x 7.62 cm	0.81723	2.6290	-0.29686	1
12.7 cm ø x 12.7 cm	0.74787	2.4077	-0.29866	1

3.3. MPPost Software Testing and Validation

It is important to use measurements to verify the validity of the Monte Carlo simulation methodology. Simulations are a key component in the development of radiation detection measurement systems; agreement between the measured and simulated results builds confidence in the ability to develop such systems in this particular manner.

Throughout all studies included within this work, the simulation tools helped better design and understand measurement systems and results. After each measurement investigation, simulations were performed to replicate all of the details of the measurements and comparisons of the results were undertaken. Many comparisons are made including PHDs to help verify the built-in source energy distributions and the energy to LO relationships. CCFs are compared to test the accuracy of the simulated correlated timing and reconstruction of pulses. Lastly, multiplicity measurement validation assures correct modeling of fissile isotope energy-dependent-multiplicity

distributions [13]. Throughout all of the validation efforts described in this work, feedback was continuously provided for the development of the latest MCNPX-PoliMi release and the overall development of the MPPost code to improve the end product.

Chapter 4. Organic Scintillator Response

Organic scintillation detectors are being increasingly used in systems that are developed to simultaneously measure neutrons and photons from fissile materials. These detectors function at an appropriate range of energy for neutron detection within this application (the typical neutron-energy range for this work is between 500 keV and 10 MeV), allowing fast-neutron detection with nanosecond accuracy. In addition to neutron detection, organic scintillators are sensitive to photons, providing an additional source of information. Furthermore, liquid scintillators offer the capability to utilize PSD processing techniques on measured data, providing an accurate method for distinguishing between neutrons and photons [15]. This dual mode of detection makes organic scintillators useful for applications requiring the detection and/or characterization of SNM.

4.1. Detection Mechanisms

4.1.1. Neutron Interactions

Neutron interactions in materials are dictated by their energy-dependent interaction cross sections. Neutrons partake in two different types of interactions: scattering and capture. When a neutron elastically scatters on a nucleus, the energy and direction of the neutron changes and the target nucleus recoils with transferred kinetic energy, but the nucleus is unchanged with regards to its proton and neutron count. With neutron capture, the target nucleus in fact changes, and a number of different types of radiation can be emitted as a result: examples include protons, alpha particles, multiple neutrons, and fission neutrons and photons [8].

Elastic scattering is the primary neutron detection mechanism in organic scintillators. In elastic-scattering events, the total kinetic energy of the incident neutron is divided between the target nucleus and the scattered neutron. On average, the fraction of the incident neutron energy (f) that is transferred to the target nucleus is defined in Eqn.

4-1 where *A* is the target nuclei's atomic weight: 0.5 for hydrogen and 0.14 for carbon. This relationship illustrates that a low-A medium will quickly decrease an incident neutron's energy in a few interactions [8].

$$\boldsymbol{f = 2A/(A+1)^2} \tag{4-1}$$

4.1.2. Photon Interactions

Three major types of photon reactions take place in matter: photoelectric absorption, Compton scattering, and pair production [7]. The dominance of the three interaction types is shown in Fig. 4-1, where Compton scattering is the dominant interaction for mid-range photon energies (0.5 to 10 MeV) across all absorption mediums and for all photon energies with low-atomic numbers (low-Z). Compton scattering is a photon interaction where an incident photon scatters on an electron, transfers a portion of its energy to the electron (always less than its full energy), and travels in an altered direction with its remaining energy.

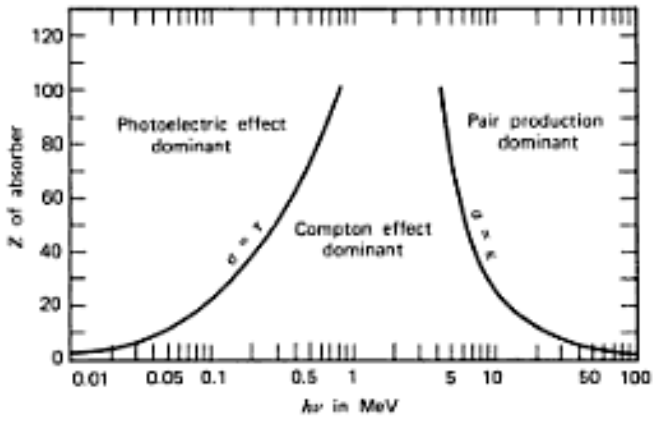

Fig. 4-1. The relevant dominance of the three primary photon interactions with relation to the atomic number (Z) of the absorber and the photon energy in MeV [7].

The low-Z material of organic hydrocarbon scintillators has a high cross section for elastic scattering of neutrons across all energies, shown in Fig. 4-2a. Compton scattering is the prominent photon interaction for SNM emitted photons in such a low-Z material, with little photoelectric effect present. Proton and electron recoil lead to the excitation and light emission that is collected and converted into an electronic pulse. Scattering events in the scintillator occur within nanoseconds and the majority of the light is collected within a single waveform. A good choice for standard liquid scintillators is

Eljen Technology's EJ-309 (H_5C_4) [16] as these liquids have been manufactured to have a higher flash point than older liquids while preserving light emission.

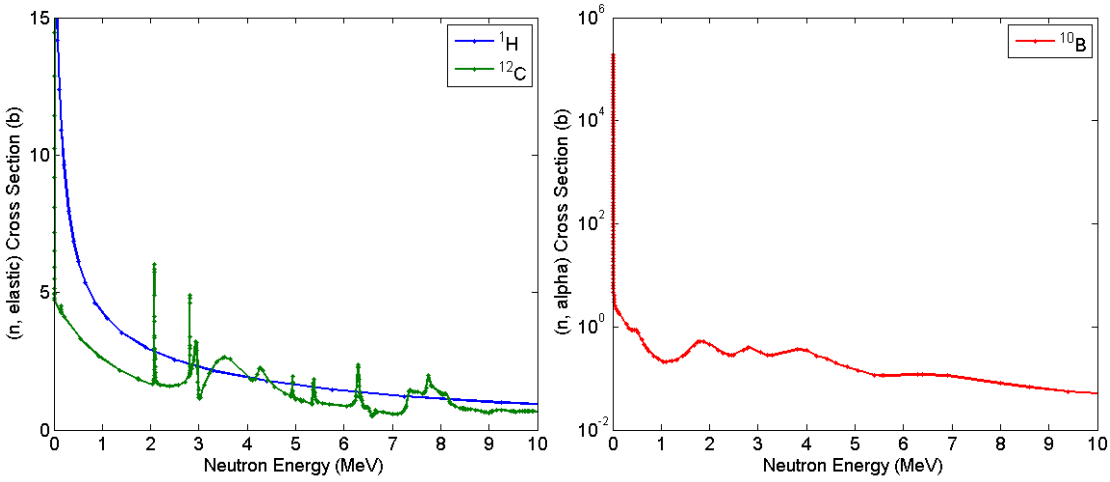

(a) (b)

Fig. 4-2. a) The neutron elastic-scattering cross sections on a linear scale as a function of the neutron energy for two isotopes [8]: ^{1}H, ^{12}C , which dictate the scattering signal in organic scintillators. b) The neutron-absorption cross section on a logarithmic scale as a function of the neutron energy for ^{10}B that is doped into organic scintillation detectors to provide capture-gated detection.

Some detectors are based on organic scintillators with added components that yield high neutron-capture properties. These so called capture-gated detectors are operated in a dual-pulse mode, resulting in the same general information as from standard liquids (using only neutron-scatter events) with added neutron spectroscopy information (when also using neutron-capture events). An incoming neutron will undergo multiple scattering events on the hydrogen and carbon present in the scintillation material; after the neutron has lost most of its energy a capture will occur. Therefore, two signals are typically detected for each fully absorbed neutron: the initial scattering pulse and the subsequent capture pulse. A graphic example of this dual-pulse scheme is displayed in Fig. 4-3. The time between the two pulses depends on the geometry and composition of the detector but is typically on the order of several hundreds of nanoseconds. The amplitude of the scattering pulse is strongly correlated to the incident-neutron energy. This work contains results from a ^{10}B-loaded liquid scintillator, Saint-Gobain's BC-523A [17].

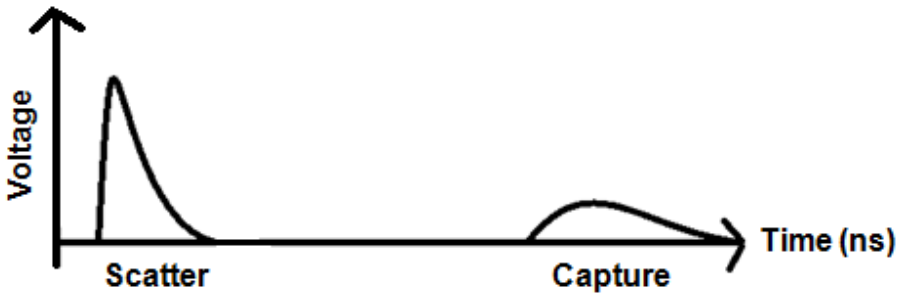

Fig. 4-3. A depiction of the dual-pulse detection scheme used to visualize the neutron energy spectrum measured by a boron-loaded liquid scintillator.

Figure 4-2a shows the neutron-scattering cross sections for the hydrogen and carbon that are present in organic scintillators, allowing detection in organic detectors and supplying the initial signal in capture-gated detectors. Figure 4-2b provides the ^{10}B neutron-capture cross section. In the BC-523A detector, the neutron-capture on ^{10}B results in an alpha particle that generates the neutron-capture pulses as shown in Eq. 4-1. In addition to the alpha particle, a high-energy capture photon is often (approximately 94% of the time) coincidentally detected with the charged particle. Also, ^{7}Li ions contribute to the detected capture pulse.

$$^{10}_{5}B + ^{1}_{0}n \rightarrow ^{4}_{2}He + ^{7}_{3}Li^{*} \quad (4\text{-}1)$$

4.2. Digital Data Acquisition

DNNG measurement systems include commercially available waveform digitizers paired with custom data-acquisition software. Acquiring digital data allows detailed and accurate data analysis, including sub-nanosecond timing and advanced neutron/photon PSD techniques. It has been found that 12-bit vertical resolution (11-bit effective) and 250 MHz sampling frequency is sufficient to pick up pulse-shape differences that are typically present between the neutron and photon interactions in a liquid scintillator [18].

Digital data acquisition allows a plethora of offline data analysis algorithms and their development. Initial data analysis includes cleaning of the digitized liquid scintillator data to remove pile-up and saturation. Examples of good pulses are shown in Fig. 4-4. In order to remove saturation, pulses are removed that do not peak within the digitizer's dynamic range of 2 V. All four detectors are gain-matched using a ^{137}Cs photon source. Fig. 4-5 shows the Compton continuum for the ^{137}Cs 662 keV mono-

energetic photons. The 2-V upper level limit will fall at varying LO values depending on the detector gain. For the settings involved in Fig. 4-5, the upper limit falls at 1.91 MeVee which equates to approximately 6-MeV neutron-energy deposition. Next, the removal of pulse pile up is an important step considering the results have an effect on PSD performance [18]. An incremental data point fraction is used (with 0.2 as the fraction) to identify waveforms that contain double pulses, where an incremental data point increases beyond the specified fraction of the first pulse's height. Photon rejection is the next step, using a PSD method described in Sect. 4.3 [15]. After PSD, many forms of data analysis are performed including pulse-height analysis, cross-correlation functions, and multiplicity.

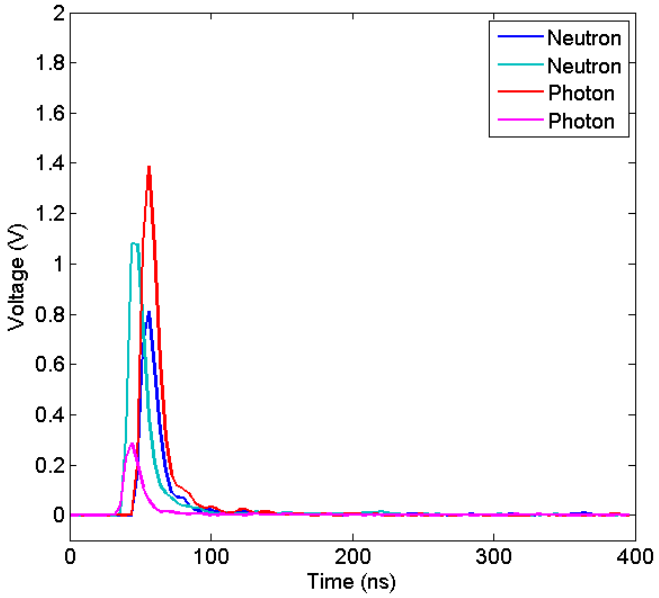

Fig. 4-4. Examples of accepted waveforms from a liquid scintillation detector with pulse widths on the order of 10 ns and full data acquisition windows of 400 ns.

Capture-gated detectors are treated very similarly when it comes to data acquisition. Neutron scatter and neutron capture events generally occur with enough time between pulses (due to the moderation of the fast neutron in the detector) that the dual-pulse mode can be acquired in two digitized waveforms by triggering on both pulses individually. Waveforms are cleaned and PSD is performed. Accepted scattering and capture pulses are then correlated to one another and the scattering pulses are used for spectroscopy.

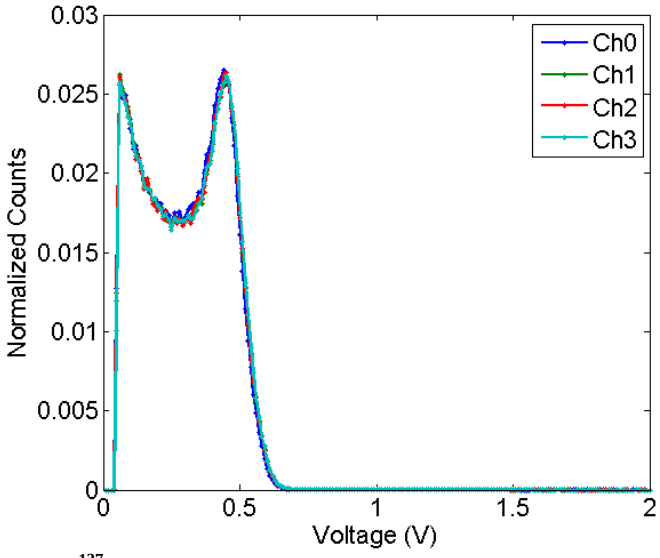

Fig. 4-5. Measured ^{137}Cs Compton continua for four gain-matched EJ-309 detectors.

4.3. Neutron and Photon Discrimination

The PSD method that is used throughout this work has been established in the past and is based on a standard charge-integration method [15]. Specifically, two integrals are calculated for each measured pulse: an integral of the pulse tail and an integral of the total pulse (Fig. 4-6). The two range-optimized integrals allow the calculation of a ratio to accurately distinguish the interacting particle type.

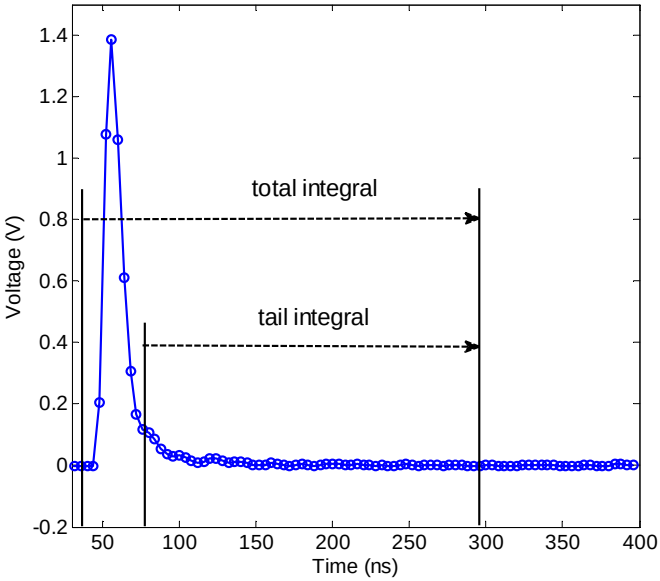

Fig. 4-6. Optimized integrals for a standard charge-integration PSD method for organic liquid scintillators.

Figure 4-7 shows the relationship between the two mentioned integrals where the separation between neutrons and photons is given by the discrimination line. Neutrons have more light in the tail of their pulses due to the mass of the recoil proton as opposed to the recoil electron involved in a photon event. The performance of the PSD algorithm varies as a function of pulse height [19] (with poorer performance at lower pulse heights). Figure 4-8 demonstrates the quality of the PSD at various pulse-height ranges where better PSD corresponds to better separation between the neutron and photon distributions. Future Chapters show this PSD distribution for a variety of nuclear materials including plutonium metal and plutonium-oxide.

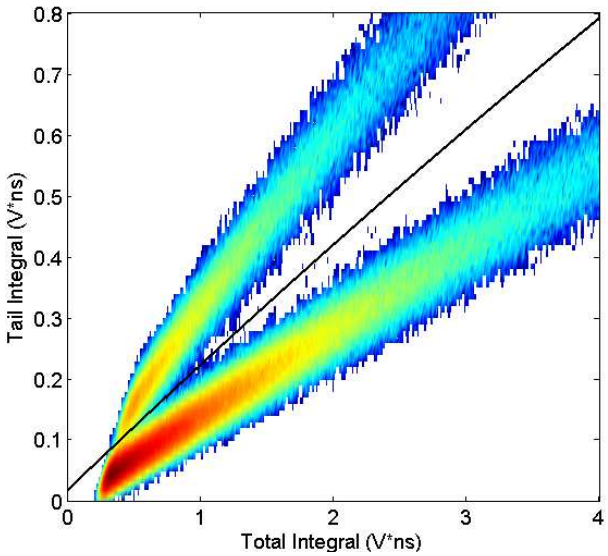

Fig. 4-7. Tail integrals versus total integrals with the neutron/photon discrimination line for a bare ^{252}Cf measurement with a 7.62 cm ø by 7.62 cm EJ-309 liquid scintillator.

^{3}He detectors used in safeguards today have ensured the ability to reject photon detection. Therefore, the PSD algorithm is one of the most crucial data analysis steps to justify the use of organic scintillators for neutron detection. SNM often emits far more photons than neutrons and therefore the effect of misclassification on neutron detection data analysis can be significant. As a general rule, we expect a photon misclassification rate on the order of 1/1000 over all pulse heights with a 70 keVee threshold. This is a very conservative rate and with extra efforts can undoubtedly be improved.

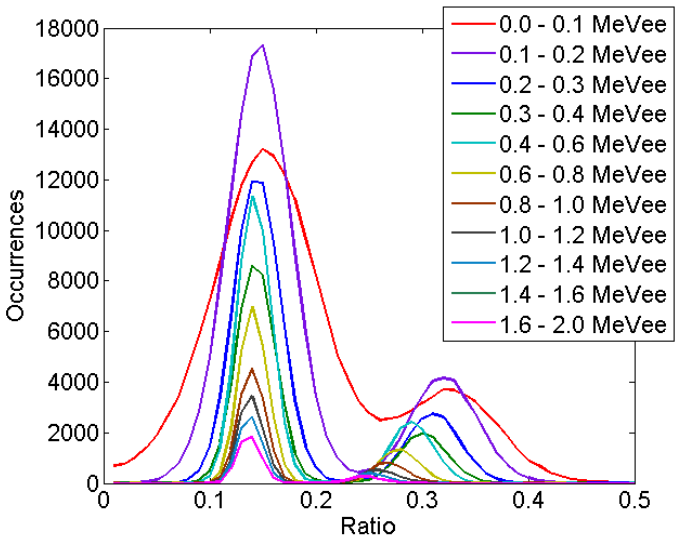

Fig. 4-8. The ratio of the tail-to-total integrals for various ranges of pulse heights from a bare ^{252}Cf measurement with a 7.62 cm ø by 7.62 cm liquid scintillator.

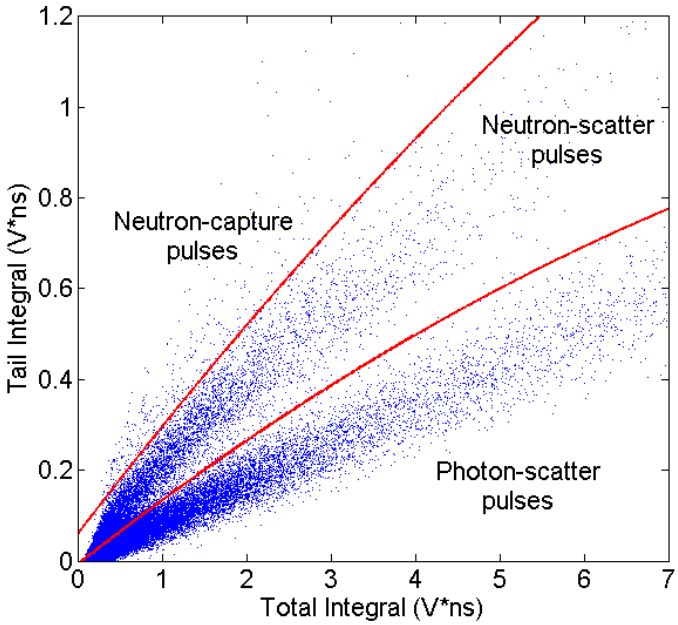

Fig. 4-9. The relationship between the tail integral and total integral of a set a pulses detected with the BC-523A detector measurement of one of the MOX samples through 5 cm of lead shielding.

In addition to standard liquid scintillators, capture-gated organic scintillators also benefit from PSD algorithms. Specifically in boron-loaded liquid scintillators, PSD is used to classify each detected event as a photon scattering event, neutron scattering event, or a neutron-capture event (generally marked by an alpha pulse). The PSD method is similar to the method used for the standard liquid scintillator data. The presence of ^{10}B in

the BC-523A liquid allows for neutron capture in the scintillation material. The neutron capture results in an alpha particle which is then stopped in the organic material, providing a pulse that has a longer decay time than the neutron and photon pulses (due to the greater mass of the alpha particle). This different pulse-shape results in a third region when visualized on the tail versus total integral plot shown in Fig. 4-9.

4.4. Detector Efficiency

The intrinsic efficiency of neutron and photon radiation detectors is an important parameter for the development of new nuclear nonproliferation techniques. For many detectors commonly used in the area of nuclear nonproliferation and nuclear safeguards, this information is also crucial for the accurate characterization of the properties of nuclear materials. Although many of these detectors provide similar information on the neutron and photon fields, their detection efficiency is not always consistent, especially as a function of energy. The efficiency for each detector may differ based on various factors in its detection mechanisms. Accurate knowledge of the detection efficiencies for various detectors can help to choose the detector type that best suits the given application.

Intrinsic efficiency describes the relationship between the number of pulses that are detected and the number of radiation quanta that are incident on the detector, as defined in Equation 4-2 [7]. This parameter provides a method of comparison that is dependent on the detector's material and geometry, on the data-acquisition system, and on the incident radiation energy. Furthermore, knowing the efficiency of a detector lends the ability to determine the absolute activity of a source.

$$\varepsilon_{int} = \frac{\textbf{number of pulses recorded}}{\textbf{number of radiation quanta incident on detector}} \tag{4-2}$$

As discussed previously within this Chapter, organic scintillators boast many positive attributes for use in measurement systems to characterize fissile material. Within the category of organic scintillators, liquid scintillators provide the most tools to be successful in nuclear safeguards applications. Another organic detector type is the capture-gated organic scintillator which adds additional neutron energy spectroscopy abilities. The detection efficiencies of both types of detectors rely on neutron elastic scattering in the organic material. For capture-gated events, the efficiency also is greatly affected by the probability of subsequent neutron capture in the detector. The following

results focus on neutron detection efficiency. Conveniently, energy dependent neutron detection efficiency can be thoroughly investigated in the simulation realm.

4.4.1. Simulated Neutron Efficiency

Three DNNG detectors were modeled to determine their intrinsic neutron scattering efficiencies. Two cylindrical standard liquid scintillation detectors (EJ-309) were modeled: 7.62 cm diameter (ø) by 7.62 cm depth and 12.7 cm ø by 12.7 cm depth. One cylindrical capture-gated detector, a boron-loaded liquid scintillator (BC-523A), was modeled: 12.7 cm ø by 12.7 cm depth. The material compositions for the standard liquid and the boron-loaded liquids are outlined in Tables 4-1 and 4-2.

Table 4-1. Atomic Composition of an EJ-309 Scintillator. The density of the material is 0.957 g/cm^3.

Active Volume Component	Isotope	Atomic Composition (%)
Liquid Scintillator	^{1}H	55.5
	C	44.5

Table 4-2. Atomic Composition of a BC-523A Scintillator. The density of the material is 0.916 g/cm^3.

Active Volume Component	Isotope	Atomic Composition (%)
Liquid Scintillator	^{1}H	55.8
	C	32.1
	O	9.1
	^{10}B	2.7
	^{11}B	0.3

Each simulation consisted of a mono-energetic, mono-directional, surface source of either neutrons or gamma rays of various energies, impinging perpendicularly on the front face of the detector where each particle immediately enters the active volume. The radius of the source matches the radius of the detectors. MPPost was used to create pulses and simulate each detector's response. Neutron-scattering signals were considered only when exceeding the applied LO threshold which was varied between 10 and 100 keVee. The relationship between the energy deposited by neutrons and the scintillator's LO is exponential, as discussed in Sect. 3.2. The capture pulses are considered ideal (it is assumed each capture event creates a measurable pulse). This assumption was made due to lack of accurate information about the amount of light created in the individual capture events.

In capture-gated detectors there are two separate intrinsic neutron efficiencies that are studied: neutron-scattering efficiency and neutron-capture-gated efficiency. Scattering efficiency characterizes the sensitivity of the organic liquid or plastic scintillator, while the neutron-capture-gated efficiency characterizes the neutron absorbing material – ^{10}B. The neutron-capture-gated efficiency describes the detector's overall ability to collect full-energy spectroscopic information. Standard liquid scintillators will only produce scatter pulses, as they do not contain any materials with high neutron absorption cross sections. Figure 4-10 shows the energy-dependent neutron-scattering detection efficiency for both the 7.62 cm ø by 7.62 cm and 12.7 cm ø by 12.7 cm EJ-309 detectors. Figure 4-11 shows the scattering detection efficiency and the neutron-capture-gated efficiency of the 12.7 cm ø by 12.7 cm BC-523A detector operated with a 50 keVee threshold (highest possible threshold to detect the capture events).

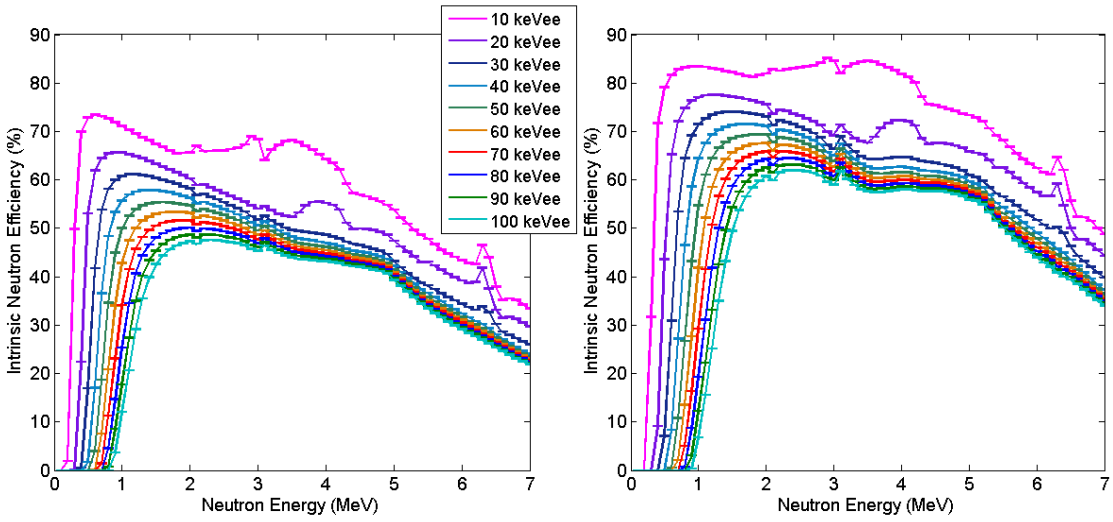

Fig. 4-10. The simulated energy-dependent neutron-scattering efficiency of the 7.62 cm ø by 7.62 cm (left) and 12.7 cm ø by 12.7 cm (right) EJ-309 detectors for various LO thresholds.

For all of the curves shown in the maximum efficiency can generally be found between the threshold and 2 MeV, which conveniently aligns with the most probable energy region for neutrons emitted from fission. As the threshold increases, the intrinsic efficiency decreases. Therefore, choosing a threshold is a compromise between neutron detection efficiency and photon misclassification as discussed in Sect. 4.3. Many features in the carbon-neutron-scattering cross section (Fig. 4-2) are only visible when the threshold is low enough to detect the low-light emission from carbon recoil.

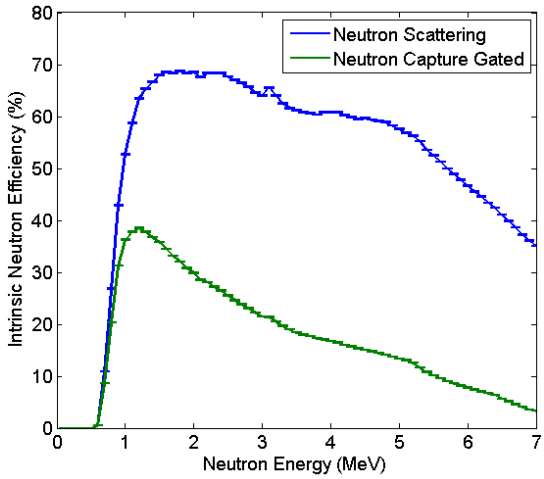

Fig. 4-11. The simulated energy-dependent neutron-scattering efficiency and neutron-capture-gated efficiency for the 12.7 cm ø by 12.7 cm BC-523A detector.

Figure 4-12a relates the depth (in the direction of the incident radiation field) of the two EJ-309 detectors (diameters of 7.62 cm and 12.7 cm) to the intrinsic neutron-scattering efficiency of 2-MeV incident neutrons. No large gains in efficiency result in detectors greater than ~10 cm. This is expected considering the mean free path of a 2-MeV neutron in the EJ-309 material is approximately 4 cm, the neutron will lose most of its energy in the first collision, and there are three to four neutron collisions per accepted pulse on average for these two detectors. Figure 4-12b relates the depth of the BC-523A detector (12.7 cm ø) to the intrinsic neutron-scattering efficiency and capture-gated efficiency of 2-MeV incident neutrons.

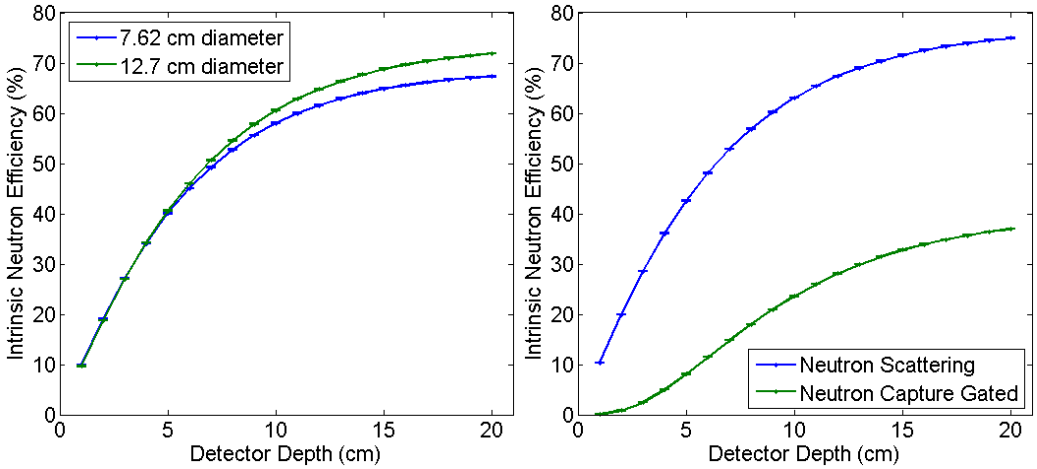

Fig. 4-12. a) Intrinsic neutron-scattering efficiency with a 70-keVee threshold as a function of the length of two EJ-309 detectors for 2-MeV neutrons and b) neutron-scattering efficiency and capture-gated efficiency with a 50-keVee threshold as a function of the length of the BC-523A detector for 2-MeV neutrons.

4.4.2. Measured Neutron Efficiency

Measuring energy-dependent neutron-detection efficiency is not a trivial task considering there are no radioisotope sources that naturally emit mono-energetic neutrons. Therefore, techniques can be used to isolate individual neutron energies such as using accelerators to induce nuclear reactions and/or using TOF measurements to identify the energy of a measured neutron from a continuous source [20]. A basic method for measuring efficiency that has been used by the DNNG includes TOF and a ^{252}Cf source: triggering on a fission event in the start detector, using TOF in stop detector (the detector under investigation) to label the neutron's energy, tallying the detection of neutrons in the stop detector as a function of energy, and then determining the detector's energy-dependent efficiency based on knowledge of neutron emission from ^{252}Cf. Fig. 4-13 shows the measured results for the 7.62 cm ø by 7.62 cm and the 12.7 cm ø by 12.7 cm detectors with 50 keVee thresholds, the setup is detailed in [14].

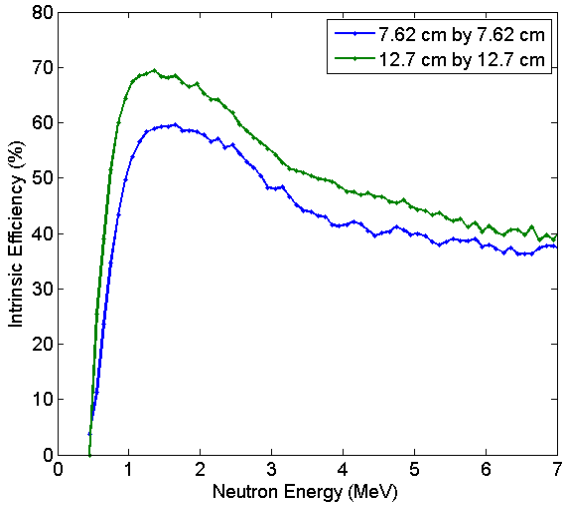

Fig. 4-13. Measured intrinsic-neutron-detection efficiency for two EJ-309 detectors measured with a ^{252}Cf source.

4.5. Neutron Energy Spectroscopy

The ability to acquire the neutron energy distribution for a given fissile source is a much sought after commodity. Current neutron detection technologies for nuclear nonproliferation applications use thermal neutron capture as the main detection mechanism, specifically with ^{3}He-gas tubes. These technologies are highly efficient and robust, but are incapable of providing in-depth information about the nuclear material's

neutron energy distribution. Organic scintillators have the potential to provide spectroscopic information as the amplitude of the PSD-attributed neutron pulses is related to the deposited neutron energy. Moderation is not necessary for detection in organic scintillators; therefore the deposited neutron energy is more closely related to the energy of the neutron emitted from the source.

Mixed-oxide (MOX) samples were measured at Idaho National Laboratory (INL) and the Joint Research Centre (JRC) in Ispra, Italy. Details regarding these measurement campaigns are described in detail in future Chapters. MOX has significant amounts of the isotope ^{240}Pu which is notable for its high spontaneous fission activity; as a result, passive measurements are possible. Additionally, due to the presence of oxygen with plutonium, (α, n) neutrons are emitted as a consequence of plutonium-isotope alpha decay, followed by alpha-particle capture on oxygen, with neutron emission as the result. Measurement results show that the use of liquid organic scintillators enables the user to distinguish pure fission sources, such as ^{252}Cf and plutonium metal, from plutonium-oxide sources (such as MOX fuel), and (α, n) sources (such as Am-Be) based on their neutron energy spectra [21].

4.5.1. Pulse-Height Distributions

To gain an understanding of the energy distribution of neutrons emitted from the measured nuclear materials, the shapes of PHDs are studied. The neutron energy distribution is of interest in nuclear safeguards as it can help characterize the type of neutron emitting material being measured. Methods used for quantifying mass, such as neutron multiplicity, often need to be calibrated based on the type of plutonium-containing material that is measured. Although PHDs do not give detailed information, the general shape of the PHD could contribute to this task.

After cleaning the digitized data, the pulse heights of all PSD-attributed neutrons and photons over the measurement threshold are histogrammed into keVee bins (commonly 10 keVee). Figure 4-14 shows an example of neutron and photon PHDs from the measurement of MOX fuel pins. Characteristic mono-energetic photons are emitted from the MOX samples and represent the significant amount of radioactive decay taking

place in the sample. Specific photon energies from abundant decays in the MOX samples will show their presence in the photon PHD as Compton edges.

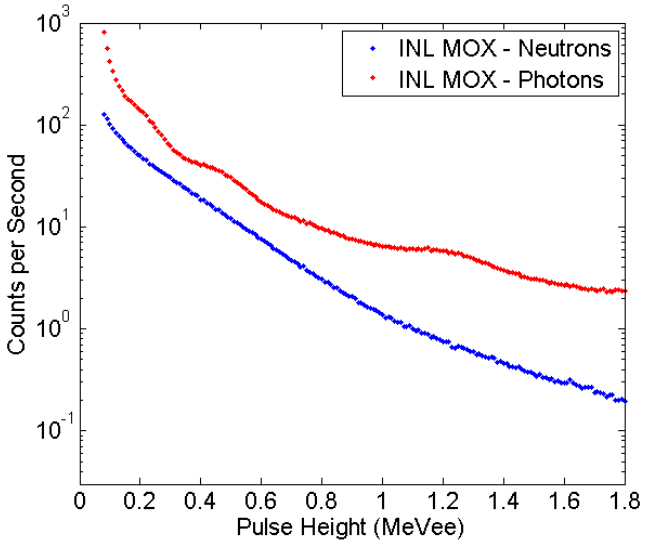

Fig. 4-14. Measured neutron and photon pulse-height distributions of a MOX sample measured at INL.

The Fig. 4-14 photon PHD shows three edges that are likely from the ^{241}Pu photons at 375 and 414 keV together, the ^{137}Cs fission fragment at 662 keV, and the common 1460 keV background photon from ^{40}K. The maximum Compton scattering energy deposition (the Compton edge) can be calculated using Eq. 4-3 where *E* equals the energy of the incident photon.

$$E_{Compton}(max) = \frac{2E^2}{(m_e c^2 + 2E)} \tag{4-3}$$

Considering that neutron scatter deposits a uniform distribution of energies from zero to its incident energy, PHDs from continuous energy sources are expected to be quite featureless, as seen in Fig. 4-14. Despite the lack of detail, the PHDs still carry useful information regarding trends in the incident neutron energy distribution [21]. Figure 4-15 shows a normalized comparison of PHDs measured from a variety of neutron sources that emit fission neutrons, (α, n) neutrons, or both.

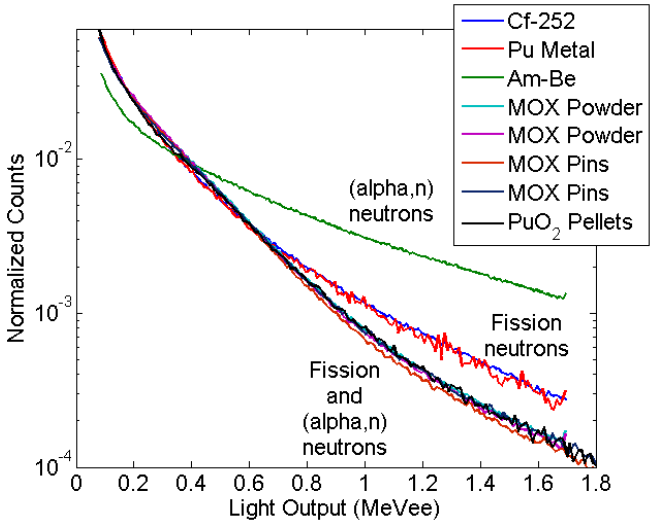

Fig. 4-15. Measured neutron pulse-height distributions (normalized to their integral) for ^{252}Cf, plutonium metal, an Am-Be source, four MOX samples, and a set of PuO_2 pellets.

The shapes of the PHDs approximately follow the average energy of the measured neutron energy distributions. The PHDs in Fig. 4-15 clearly provide the ability to distinguish between different categories of sources: (α, n) neutrons from Am-Be, fission neutrons from ^{252}Cf and plutonium-metal, and a combination of fission and (α, n) neutrons from MOX and PuO_2. Figure 4-16 displays the simulated neutron energy spectra, through 5 cm of lead, and incident on the detector face for a number of sources measured at the INL and JRC facilities. For comparison, a few measured average neutron pulse heights and simulated average neutron energies for the nuclear materials measured in Fig. 4-15 are shown in Table 4-3.

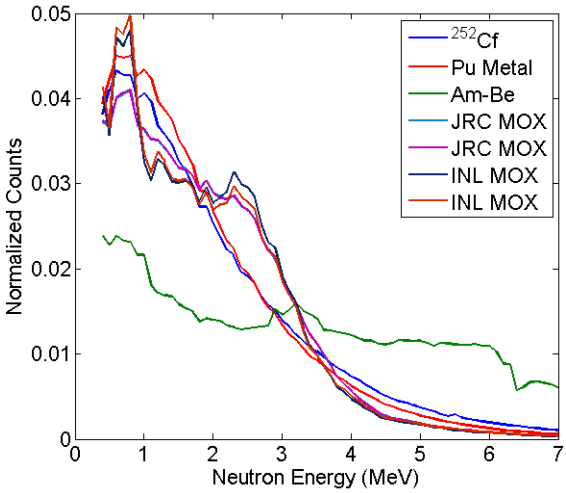

Fig. 4-16. Simulated neutron energy distributions, tallied on the detector faces through the 5 cm of lead shielding, for the seven neutron sources studied in this work.

The EJ-309 PHDs showed clear identification capabilities between different categories of neutron sources. This proves that organic scintillation detectors can provide identification of sources based on neutron energy information. Techniques such as neutron-energy-spectrum unfolding have the potential to uncover more information about the neutron-energy distribution.

Table 4-3. Average measured pulse heights and simulated average incident neutron energies for select sources.

Sample	Average Measured Pulse Height (MeVee)	Average Incident Neutron Energy (MeV)
INL MOX	0.29	1.91
JRC MOX	0.29	1.95
^{252}Cf	0.30	2.08
Am-Be	0.49	3.70

4.5.2. Neutron-Energy-Spectrum Unfolding

Spectrum unfolding can be used on organic scintillator PHDs to obtain estimations of incident neutron energy spectra. As mentioned previously, the amplitude of neutron pulses is related to the deposited neutron energy. Despite this relationship, when using organic scintillation detectors, the resulting PHDs require the use of unfolding techniques to obtain the incident neutron energy information. MCNPX-PoliMi/MPPost is used to accurately model the neutron source from materials such as MOX, and provide the neutron energy distribution for comparison to the experimental estimations. Additionally, the simulation package can be used to develop the organic scintillator's three-dimensional detector response as a function of incident-neutron energy and the LO response.

Two varieties of MOX at the JRC were measured, which are composed of various uranium, plutonium, and oxygen isotopes, leading to neutron emission from spontaneous fission, induced fission, and (α, n) reactions. The plutonium-metal samples' neutron emission is exclusively from the spontaneous fission of ^{240}Pu. The Am-Be provides a unique spectrum from (α, n) reactions that allows good comparison to the rest. Figure 4-16 includes the shapes of the neutron energy distributions for the discussed sources. Figure 4-17 shows the measurement set up and its simulated counterpart including four 12.7 cm ø by 12.7 cm EJ-309 detectors, with 5 cm of lead shielding, and located 30 cm from the sample's center axis.

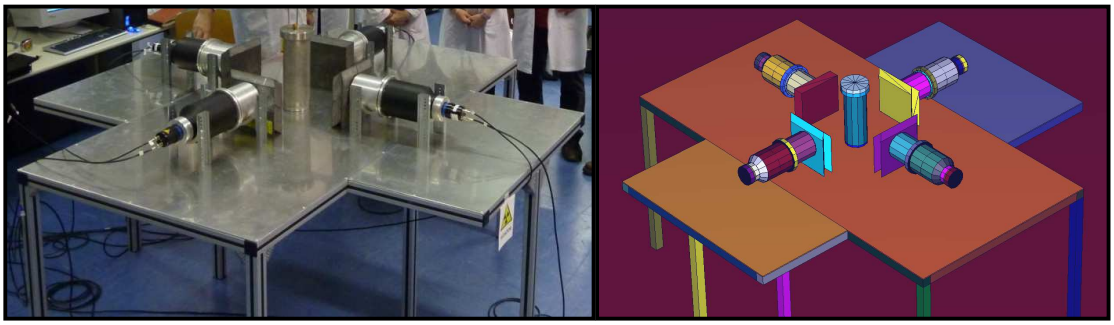

Fig. 4-17. Four EJ-309 liquid scintillators surrounding a 1-kg MOX sample with 30 cm spacing from the center of the source to each of the detector faces. 5 cm of lead shielding is present in front of each detector. MCNPX-PoliMi was used to simulate the measurement configuration.

The estimation of neutron energy spectra, specifically through unfolding methods that involve the solution of inverse problems, requires detailed knowledge of the detector's response for individual neutron energies incident on the detector. This response is packaged into a matrix that is obtained through a series of simulations. This routine can be easily repeated and allow comparison of neutron spectrum estimation for a variety of organic scintillation detectors.

Neutron-spectrum unfolding is a process that includes solving an inverse problem in order to acquire the incident neutron energy from the combination of the measured result and a detailed detector response. This problem is outlined in Eq. 4-4, where we are solving for $\Phi(E_n)$. The response matrix, R, is a function of the measured LO, L, and single neutron energy, E_n. The count-rate density N is what is measured and is only a function of L. The response matrix must be formed for a particular detector in advance. As previously described, simulations were used to acquire the response matrix for this study.

$$N(L) = \int R(L, E_n)\,\Phi(E_n)\,dE_n \tag{4-4}$$

The solution to direct inversion of this problem is ill-conditioned. Thus, inversion can result in nonphysical results and has a great sensitivity to statistical uncertainty in the measurements or errors that develop during the measurement process (noise for example). Therefore, in this unfolding example, a sequential least-squares method is used [22]. At each iterative step (solution approaching the estimated spectrum), a quadratic sub-problem is solved with realistic boundaries. The subsequent solutions are still

considered to be rough estimations as they strongly rely on uncertainties in both the detector response matrix and the measurement itself.

Figure 4-18 displays the simulated detector response matrix that was used to develop the estimated neutron energy spectra shown in this work. With the knowledge of the amount of LO that is produced by neutron interactions in a hydrocarbon scintillator (such as EJ-309), we can simulate PHDs for various mono-energetic neutron beams incident on the detector. After running a wide range of simulations, each of the resulting PHDs can be combined into an overall detector response. If the LO dimension were to be collapsed, the result would be an efficiency curve as shown in Sect. 4.4. The estimated neutron energy spectra appear to be greatly sensitive to the accuracy of this response, thus accurate simulation of detector response is crucial.

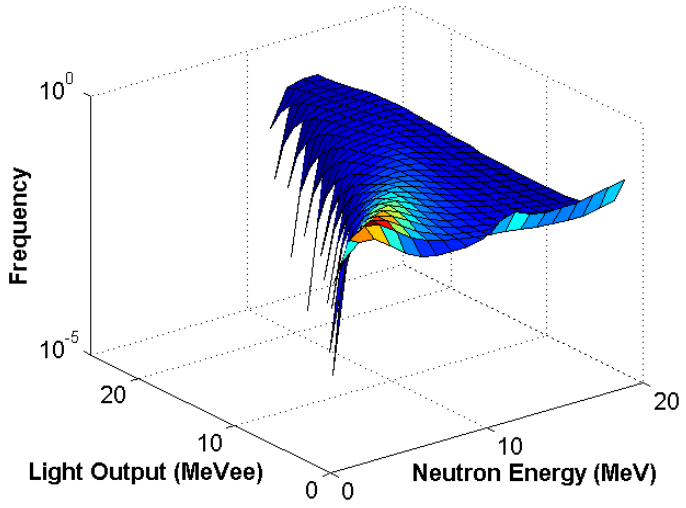

Fig. 4-18. MCNPX-PoliMi simulated detector response for an EJ-309 liquid scintillator with a 12.7 cm ø and 12.7 cm depth.

It was determined that measured neutron PHDs provided the capacity to clearly distinguish between different source categories, such as purely fissile sources or those that also involve neutron emission from (α, n) reactions. Although, more detail of the neutron energy spectrum is desired. Therefore, efforts have turned towards unfolding neutron energy spectra estimations from PHDs.

Figure 4-19a shows the simulated neutron energy distributions of the neutrons incident upon the four liquid detectors, through the 5 cm of lead shielding, displayed in a course binning scheme. The ^{252}Cf and the plutonium-metal simulations depict the

expected fission Watt spectra. The two MOX sources are very similar to each other in their combination of the Watt spectra from spontaneous and induced fission reactions plus the additional knee contributed by neutrons that are a result of (α, n) reactions. The Am-Be source, as expected, provides a broad distinct shape that is vastly different from the other measured sources.

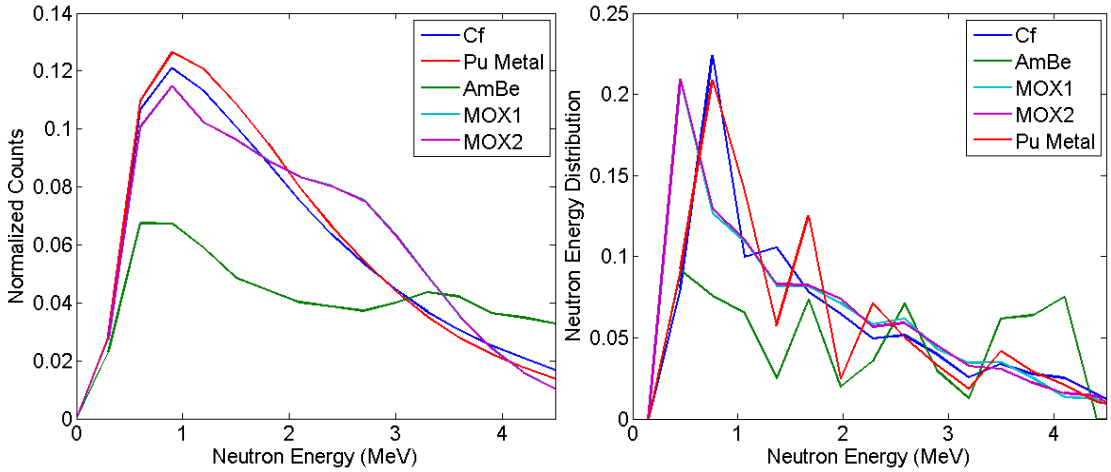

Fig. 4-19. a) Simulated neutron energy distributions, tallied on the detector faces with a large binning scheme that matches the current limitations of the unfolding method and b) spectrum unfolding results obtained from measured PHDs for the five neutron sources of interest.

Figure 4-19b shows a comparison of the unfolded measured PHDs for all five sources. The same conclusions can be drawn from Fig. 4-19b as for the measured PHDs: characterization of neutron sources into various categories. Therefore, it can be said that neutron spectrum unfolding with this particular algorithm and parameters does not provide an advantage over the study of basic PHDs alone.

An improvement in unfolding results is seen when inputting a "simulated" neutron PHD into the algorithm, as shown in Fig. 4-20. This can be considered as a limit to the unfolding abilities with this specific algorithm and its configuration, which revolves around a simulated detector response matrix.

The estimation of neutron energy spectra, through unfolding did not provide results that would give an advantage over studying differences portrayed in the PHDs alone. This work did provide a good starting point with much room for improvement in the data analysis algorithm designed to perform spectrum unfolding. One of the largest areas for improvement is in the development of the accurate detector response matrix.

Improved knowledge of the energy deposited to LO relationship and optimization of the binning scheme used in the detector response matrix had a significant impact on the unfolded results in subsequent efforts. Additionally, expanding the investigation to novel organic detectors promises to provide much insight into the task of accurately measuring neutron energy spectra.

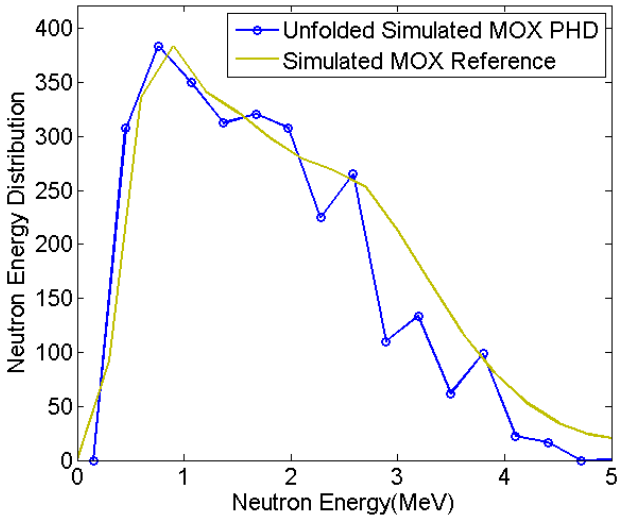

Fig. 4-20. The unfolded simulated PHD of a MOX sample compared to the simulated neutron energy distribution.

Potential spectroscopy in organic scintillators provides yet another tool that these detectors bring to the table for nuclear nonproliferation and safeguards applications. Additional pieces of information only solidify these detectors as good candidate for advanced system design.

4.5.3. Capture-Gated Spectroscopy

Additional spectroscopy information is available in organic scintillators that combine neutron-capture capabilities with their usual neutron scatter mechanisms: "capture-gated detectors". Such detectors can be analyzed utilizing a dual-pulse detection scheme as discussed in Sect. 4.2. This work focuses on the neutron spectroscopic abilities of a boron-loaded liquid scintillator (BC-523A [17]) in comparison to a standard liquid scintillation detector (EJ-309 [16]). These spectral results will be demonstrated through measured neutron-capture-gated PHDs. Classification of neutron-scatter pulses and neutron capture pulses using the PSD algorithm is crucial in order to obtain these results [15].

Data were collected with the BC-523A during the measurements performed at the JRC facility in Ispra. Figure 4-21 shows the neutron-scattering PHDs for four sources measured with the BC-523A detector. The amplitude of the PSD-attributed neutron pulse is related to the energy the scattered neutron deposited in the liquid, resulting in a unique PHD for each sample. Figure 4-22 shows the neutron-capture-gated PHDs for the four neutron sources. Because the incident neutron must thermalize before it captures on ^{10}B, we anticipate the preceding neutron scatter pulse to contain the majority of the initial neutron energy, assuming that it completely thermalized in the hydrocarbon organic material. Therefore, the capture-gated PHD omits neutron-scatter pulses from neutrons that escape the scintillator. As a result, we see the capture-gated PHDs to relate more closely in shape than the scattering PHDs to the expected energy distribution of the neutrons entering the detector (shown in Fig. 4-22).

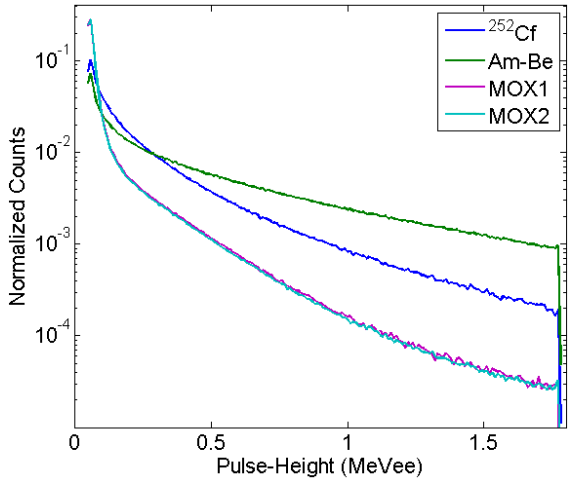

Fig. 4-21. A comparison of the neutron scatter PHDs from the BC-523A for the four samples presented during this study.

There are a few challenges present when using this dual-particle detection mode that must be considered. Primarily, the pulses produced when detecting an alpha particle yield very little light, therefore the measurement threshold must be set relatively low. A lower threshold gives way to poorer PSD, as previously discussed. The next challenge is determining the time window in which to correlate alpha events with neutron scattering events. For these results, all alpha events were matched with the proceeding neutron scatter event, but the use of a well-chosen time window will minimize accidental correlations.

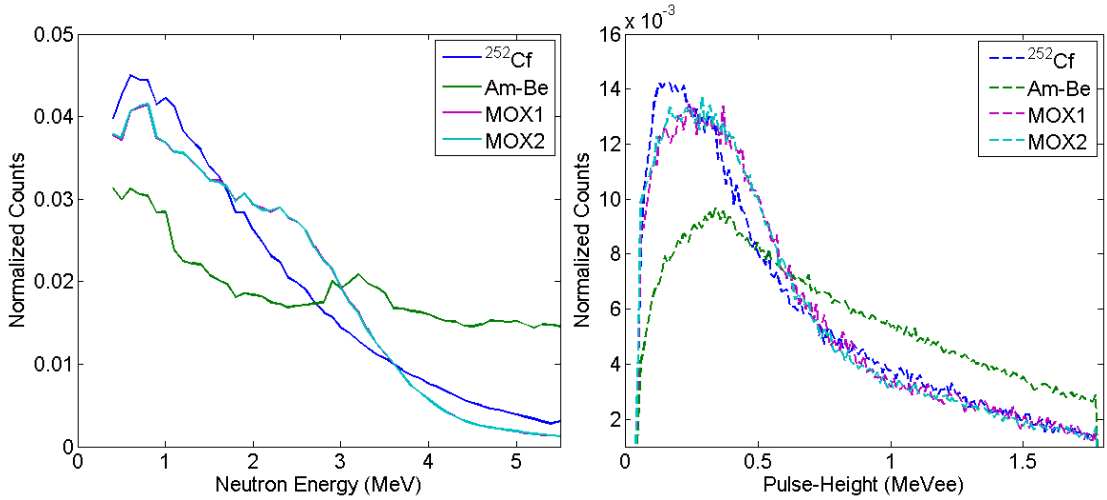

Fig. 4-22. The simulated neutron energy distributions for the samples compared in this study (left) and a comparison of the capture-gated-neutron PHDs (right). The PHDs closely follow the trends of the anticipated neutron energy distributions entering the BC-523A detector.

The neutron scatter PHDs alone allow the categorization of the measured nuclear materials. The PHDs that are developed through the neutron capture dual-pulse detection mode achieve the same goal, while providing more insight into the shape of the incident neutron energy distribution. The improved characterization ability that is gained using the dual-pulse detection mode results in a decrease in detection efficiency. Table 4-4 summarizes the measured efficiencies and compares them to an EJ-309 detector and an NPOD ^{3}He detector array.

The measured detection efficiency for the standard liquid detectors used in this investigation was 45.47%, similar to the neutron scatter intrinsic efficiency for the BC-523A detector (58.34%) prior to the pairing of alpha and neutron scatter pulses. The BC-523A detector has a higher scattering detecting efficiency only because a lower threshold was used to detect the low-light alpha-particle pulses. Once pairing capture pulses to scattering pulses for the neutron-capture-gated efficiency, the intrinsic efficiency decreases to nearly 3% for the ^{252}Cf case. Despite the cut in efficiency present when pairing with capture-pulses, the capture-gated intrinsic efficiencies for the BC-523A were still acceptable when compared to the NPOD system, a portable multiplicity counter, developed by Los Alamos National Laboratory, containing fifteen ^{3}He tubes moderated by polyethylene.

Table 4-4. Intrinsic efficiency values compared for a boron-loaded liquid scintillator (BC-523A with a 50 keVee threshold), a standard liquid scintillator (EJ-309 with a 70 keVee threshold), and an NPOD ^{3}He detector array for the ^{252}Cf and Am-Be measured samples.

Detector	^{252}Cf		Am-Be	
	Neutron Scatter (organic)/Capture (^{3}He) Intrinsic Eff.	Neutron Capture-Gated Intrinsic Eff.	Neutron Scatter (organic)/Capture (^{3}He) Intrinsic Eff.	Neutron Capture-Gated Intrinsic Eff.
BC-523A	58.34	2.72	51.50	1.98
EJ-309	45.47	--	35.48	--
NPOD	20.51	--	14.67	--

In conclusion, capture-gated detectors such as the BC-523A have potential for SNM characterization, specifically spectroscopy beyond the capabilities of standard liquid scintillators. When considering the use of these detectors for safeguards and nonproliferation application, the low efficiency of getting spectral information must be kept in mind.

Chapter 5. Passive Neutron-Correlation Measurements

Because MOX contains a significant amount of ^{240}Pu (strong spontaneous fission source; ~1000 neutrons per second per gram) and alpha-emitting isotopes, a variety of passive neutron measurements are possible. Non-destructive passive assay of SNM requires much development but is a technique that is usually preferred to non-destructive active interrogation methods and destructive assay methods.

Methods for passive fuel characterization include the analysis of neutron energy distributions, time-of-flight distributions, cross-correlation functions, and neutron and photon multiplicity distributions. Measuring MOX fuel pins located at INL and MOX powder at the JRC in Ispra, Italy provided the opportunity to develop faster and more robust methods for characterization of SNM, with correlated neutron detection. Passive measurements were performed on a variety of neutron sources, including: a large number of fuel pins (totaling approximately 1 kg of plutonium) with varying isotopic composition, 1 kg of MOX powder, ^{252}Cf, and Am-Be. The primary objective of these measurements was to differentiate and characterize the mentioned sources based on the analysis of neutron cross-correlation functions.

5.1. Simulation of Passive Neutron Correlations

Monte Carlo simulations were performed to study methods of using cross-correlation functions to characterize MOX fuel. This approach allows development of accurate nuclear material characterization schemes, providing detailed insights into the sensitivity of nuclear materials and measurement approaches. The simulations include basic tallied neutron energy distributions, PHDs, and time-correlated particle detections.

The MCNPX-PoliMi model of the measurement set-up, as shown in Fig. 5-1, includes four lead-shielded EJ-309 liquid scintillation detectors placed around the axis of the MOX fuel pin set-up (Fig. 5-2), with each detector equidistant from the source. Each detector was 12.7 cm ø and depth and each lead shield is 5-cm thick. The composition of

the fuel pins was varied during the simulations to model two fuel-pin types, see Table 5-1. A LO threshold of 75 keVee (75 keV electron equivalent) is used in post processing.

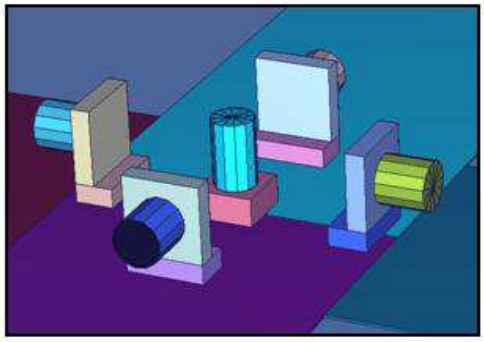

Fig. 5-1. MCNPX-PoliMi simulation of four cylindrical EJ-309 liquid scintillators surrounding a MOX fuel can. Each detector is shielded by 5 cm of lead. The MOX fuel can is supported by a 7.5-cm thick styrofoam stand.

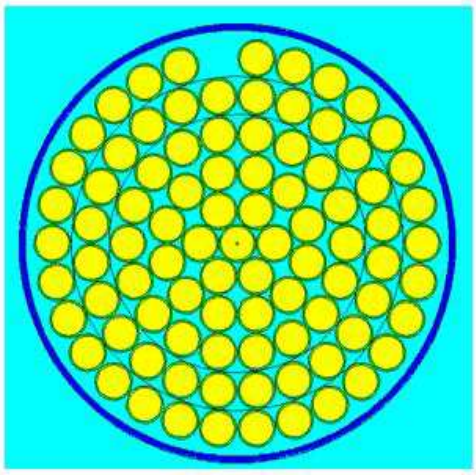

Fig. 5-2. Cross-sectional view of the 90-pin MOX fuel can where the MOX fuel is modeled within the cladding (stainless steel, 0.5-mm thick) and the pins are contained by a 0.16-cm thick aluminum can.

Table 5-1. Isotopic composition of MOX fuel pins used for this work at INL [23] (age corrected to the June 2009 measurement date).

Isotope	Pin #1 (wt. %)	Pin #2 (wt. %)
^{235}U	0.17	0.16
^{238}U	74.78	72.13
^{238}Pu	0.01	0.01
^{239}Pu	11.42	10.98
^{240}Pu	***1.53***	***4.10***
^{241}Pu	0.17	0.58
^{242}Pu	0.02	0.02
^{241}Am	0.06	0.16
O	11.85	11.86

MCNPX-PoliMi was used to model the spontaneous-fission (SF) and (α, n) sources that are common in MOX fuel. Two well-defined fuel-pin types were available for measurement at INL. Both pin types are composed of various uranium, plutonium, and oxygen isotopes. The primary difference in the materials is in the mass of the ^{240}Pu isotope. This detail is significant as ^{240}Pu is the primary neutron contributor for this type of advanced fuel. Table 5-1 shows the composition of the INL fuel pins. Fig. 5-3 shows what sources were simulated and their contributions to the total neutron production rate. The SF of ^{238}Pu, as well as the (α, n) sources ^{235}U, ^{238}U, and ^{241}Pu were omitted due to their negligible contributions to the total neutron source. The total neutron multiplication values for the two fuel-pin assemblies were 1.13 and 1.14, respectively.

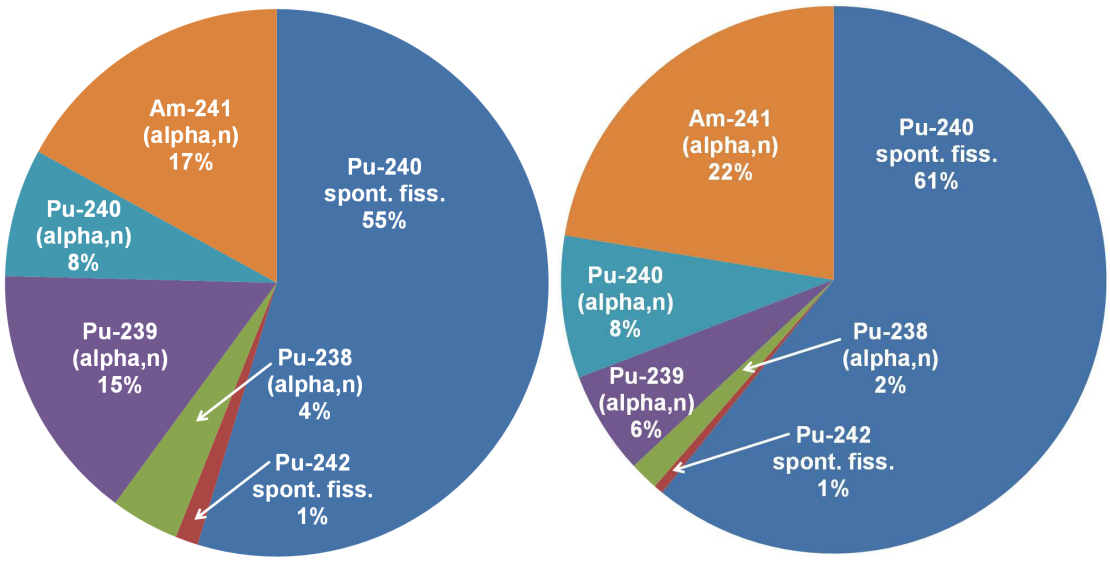

Fig. 5-3. Contributions (neutron emission rates) of spontaneous-fission and (α, n) sources present in the INL MOX pins to the total neutron production of fuel types #1 and #2.

MOX was also measured at the JRC in the form of two powder samples of identical isotopic composition. Table 5-2 contains the MOX isotopic for the JRC powder samples and Fig. 5-4 describes the neutron source. Also measured at the JRC were a ^{252}Cf SF source and an Am-Be (α, n) source.

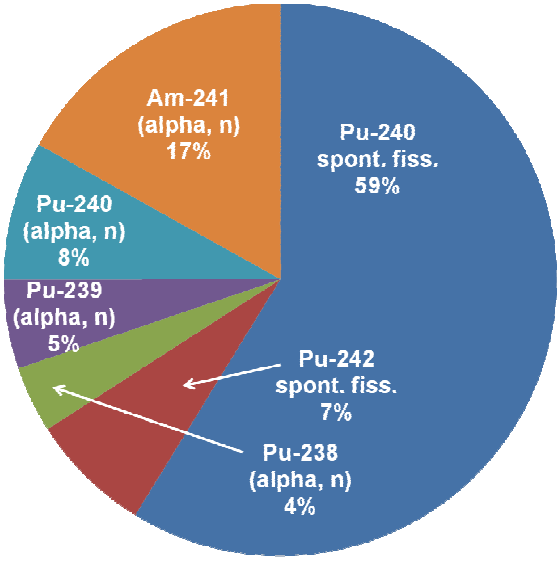

Fig. 5-4. Contributions to the total neutron productions by SF and (α, n) sources present in the JRC MOX powders.

Table 5-2. Isotopic composition of MOX powder used at the JRC (age corrected to the June 2010 measurement date).

Sample: Isotope	MOX-1 (g)	MOX-2 (g)
^{234}U	0.05	0.06
^{235}U	4.79	5.50
^{236}U	0.05	0.06
^{238}U	670.50	769.48
^{238}Pu	0.24	0.27
^{239}Pu	111.81	127.02
^{240}Pu	***47.00***	***53.39***
^{241}Pu	1.67	1.90
^{242}Pu	3.38	3.84
^{241}Am	5.12	5.82
O	166.22	184.00
Total	1010.83	1151.33

5.1.1. Simulation Results

Fig. 5-5a shows the simulated energy distributions of the neutrons emitted from the two 90-pin MOX fuel assemblies. The valleys located in the lower energy region of both spectra, specifically near 0.5, 0.1, and 1.3 MeV, are due to resonances in the neutron elastic scattering cross section of ^{16}O, which is also shown in Fig. 5-5a [24]. Fig. 5-5b shows the individual neutron source contributions (SF and AN) to the total neutron energy distribution of the Pin#1 MOX fuel assembly.

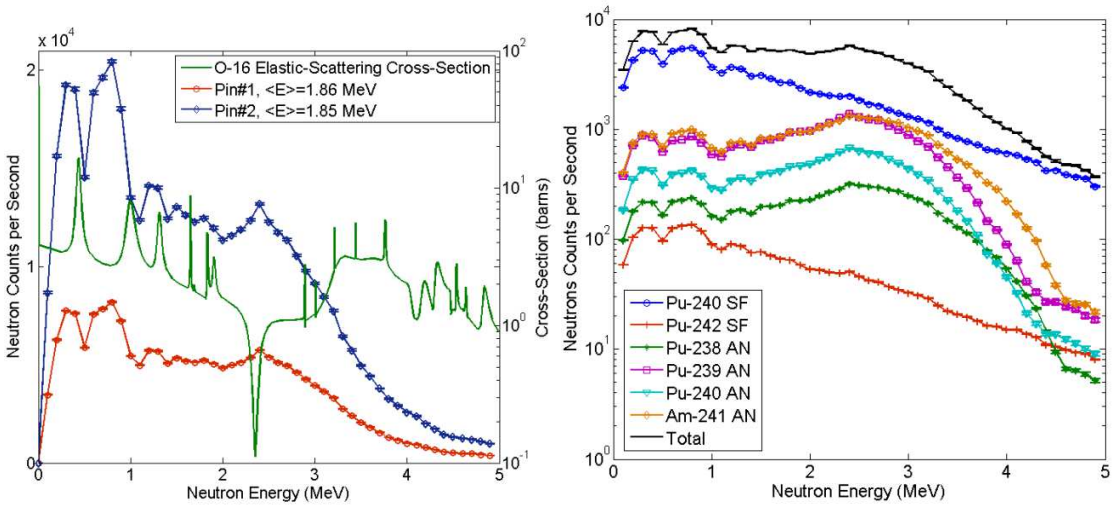

Fig. 5-5. a) Simulated neutron energy distributions, tallied on the fuel-pin can (maintaining the pin assembly), for 90-pins of MOX fuel in comparison to the oxygen elastic scattering cross section. b) Simulated neutron energy distribution for 90-pins of Pin#1-type MOX fuel (tallied on the fuel-pin can) broken into its individual neutron source contributions.

Currently, the measurement of neutron energy distributions of fissile materials is an area of much needed development. If the detection of these oxygen related spectral features were possible, SNM containing oxides would be identifiable. Additionally, the neutron energy distributions of Fig. 5-5 display both the fission neutron distributions and the (α, n) distributions. The detection of these regions can also point to the presence of MOX. These effects were apparent when studying the PHDs in Sect. 4.5.1.

5.2. Passive Measurements of Fissile Material

5.2.1. Passive Measurement Configurations

The UM measurement system consisted of four cylindrical EJ-309 liquid scintillation detectors (12.7 cm ø by 12.7 cm), a fast digitizer, and data-acquisition and data-analysis algorithms. In the measurements, the detectors were placed horizontally in 90° intervals around a can of MOX fuel pins, with each detector equidistant from the sample, as shown in Fig. 5-6 for the INL measurements and Fig. 4-18 for the JRC measurements. Detector pairs (at 90° or 180°) are used for time-correlated neutron and photon detections. Lead bricks (5-cm thick) were used to shield the face of each detector as necessary to appropriately attenuate the fuel assembly's photon background.

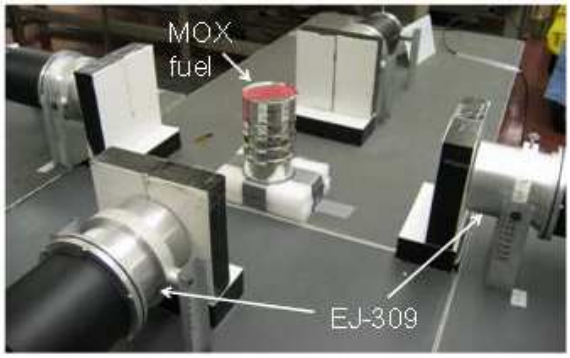

Fig. 5-6. Four EJ-309 liquid scintillators surrounding a 90-pin MOX fuel can with 40-cm spacing from the center of the source to each of the detector faces. Five cm of lead shielding is present in front of each detector to decrease the gamma-ray count rate.

The data acquisition system contained a 12-bit, 250-MHz, 8-channel, CAEN V1720 digitizer used to sample and store measured pulses. The experimental configurations included the two pin types (#1 and #2), packaged in 90-pin quantity canisters (as shown in Fig. 5-7). The MOX powder was contained in a stainless steel cylinder. Measurement times varied based on the emission rate of the samples, ranging from 10 minutes to an hour. Cross-correlation functions are obtained from differences between the arrival times of two correlated detection events [25], within ± 50 ns.

Fig. 5-7. MOX fuel pins of well-known composition were packaged into two cans in known quantities.

5.2.2. Experimental Results

The primary goal of this study was to develop methodologies to characterize SNM. Cross-correlation functions are suitable for such characterization, specifically for cases with a well-controlled geometry. Fig. 5-8 provides a comparison between 90 pins of the two fuel pin types in terms of separated correlations (neutron-neutron, neutron-photon, photon-neutron, and photon-photon correlations). The ability to distinguish

between neutron and photon events allows more detailed study of those correlations which provide us with information about the source.

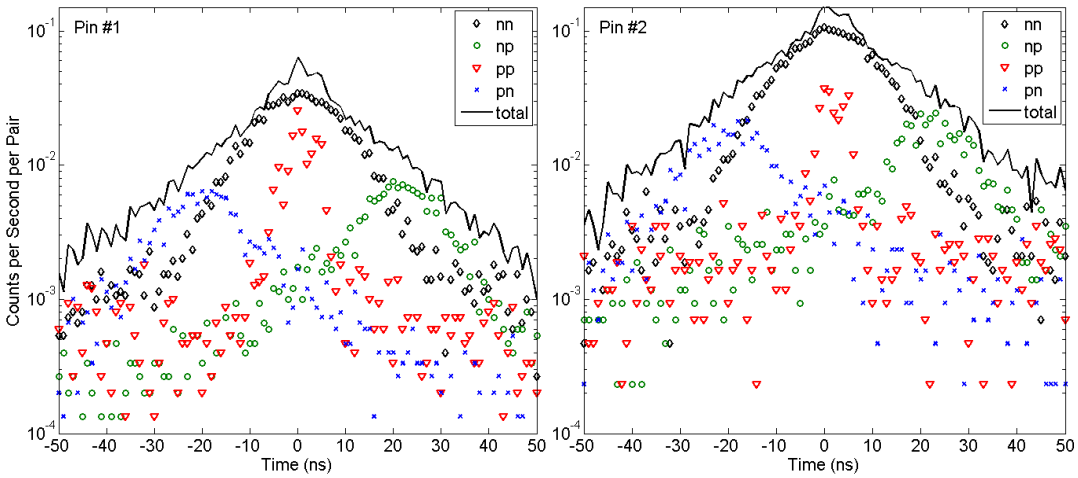

Fig. 5-8. Cross-correlation curves, including all possible particle combinations, discriminated into their components through a PSD processing algorithm. Measurement performed on Pin #1 (left) and Pin #2 (right) with the detectors spaced at 40 cm from the center of the source and a 75-keVee threshold.

Fission is one of the few reactions that results in more than one neutron per decay. Thus, the analysis of neutron-neutron correlations provides valuable information on the presence of fissile material in an unknown sample. The increased presence of the ^{240}Pu isotope in Pin #2 (and therefore expected increase in fission neutrons) is observed when comparing the neutron-neutron correlation curves in Fig. 5-9. Between –20 ns and 20 ns Pin #1 provided 4.59 ± 0.04 correlated neutron counts per second and Pin #2 provides 14.02 ± 0.14 correlated neutron counts per second (values are summarized in Table 5-2). The difference in these count rates (~ a factor of 3) is very similar to the difference in the amount of ^{240}Pu (a factor of 2.7). This technique is promising in terms of characterizing a sample's fissile content and separating out the neutron detection that is caused by (α, n) reactions occurring in the presence of oxygen, when a measurement configuration is well controlled.

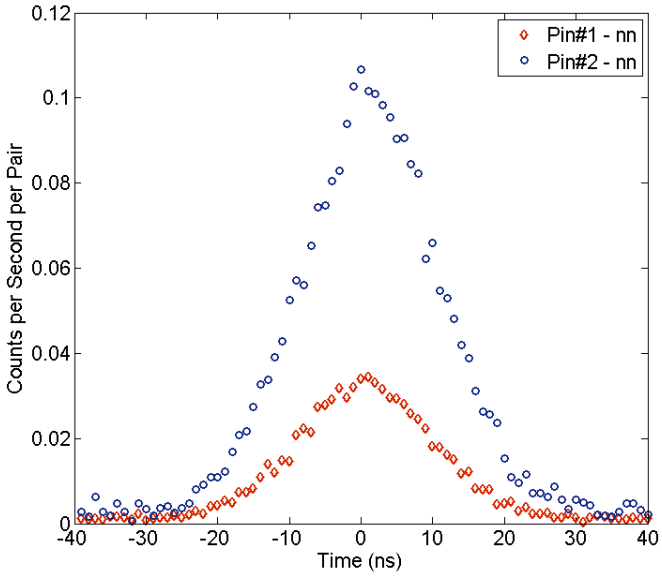

Fig. 5-9. Comparison of neutron-neutron correlations for the two INL MOX samples.

Table 5-2. Calculated neutron emission rate from spontaneous fission, measured neutron count rate, and measured correlated neutron count rate for the two MOX fuel-pin assemblies.

	Pin #1 Assembly	Pin #2 Assembly	Pin #2/Pin #1
SF Neutron Emission Rate	1.28E5	3.39E5	2.65
Neutron Count Rate	2049.14 ± 0.91	4977.80 ± 2.59	2.43
Correlated Neutron Count Rate	4.59 ± 0.04	14.02 ± 0.14	3.05

Neutron-neutron correlations indicate the percentage of neutron emitting reactions that are a result of spontaneous or induced fission. Figure 5-10 shows the nn-correlation curves normalized by the known neutron-emission reaction rates for ^{252}Cf, Am-Be, and MOX measured at the JRC. The magnitude the nn-correlation curves depicted in this manner increases with the percentage of spontaneous fission reactions: ^{252}Cf is 100% SF, MOX is ~42% SF, and Am-Be is 100% AN. The nn-correlation curves are made up of correlated neutron detections from true correlated-neutron events, correlations from cross talk, and accidentals. Cross-talk events occur when a single neutron interacts in one detector, creates a recordable pulse, escapes the detector, interacts in a second detector, and has enough remaining energy to create a second pulse over threshold. Cross-talk events are false coincidence events that are often difficult to distinguish from true events. For this reason, the non-fissile Am-Be source has false correlated-neutron events, and their location helps identify them as primarily cross-talk events due to the large time-

differences compared to the zero centered distribution that is seen from fission. Cross-talk events are present in the ^{252}Cf and MOX measurements, but are more prevalent in the Am-Be measurement due to its higher average neutron energy, making it more probable for neutrons to have enough remaining energy after the first detected pulse, to create a second one in a different detector.

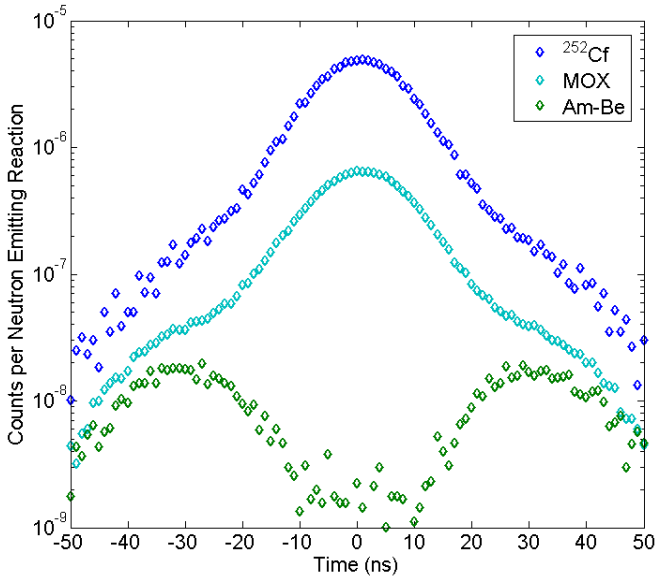

Fig. 5-10. Neutron-neutron correlations for three samples measured at the JRC facility, normalized by their known neutron emission reaction rates.

Additionally, comparisons can be made between the nn-correlation integrals (between -20 and 20 ns), for 180-degree and 90-degree detector pairs for each measurement, as shown in Fig. 5-11. These comparisons depict the anisotropy of fission neutrons, theoretically and experimentally observed [26]. For Pin #1 the ratio of 180-degree/90-degree correlated neutrons is 1.02 ± 0.02 while Pin #2 has a ratio of 1.12 ± 0.02. The simulations predict this ratio to be 1.03 for both measurement configurations. The 90-degree neutron correlations are artificially increased by the presence of cross talk in the system (which contributes approximately 6% of the correlations in the 90-degree pairs and only about 2% in the 180-degree pairs). Therefore, the effect of anisotropy is higher than shown in the ratios, and a cross-talk correction on the data would lead to more accurate results. We expect this ratio to be nearer to 6.0 for 2-MeV neutrons in an unshielded case [27]. The simultaneous detection of time-correlated neutrons and the measured anisotropy further proves the detection of fission neutrons from the sample.

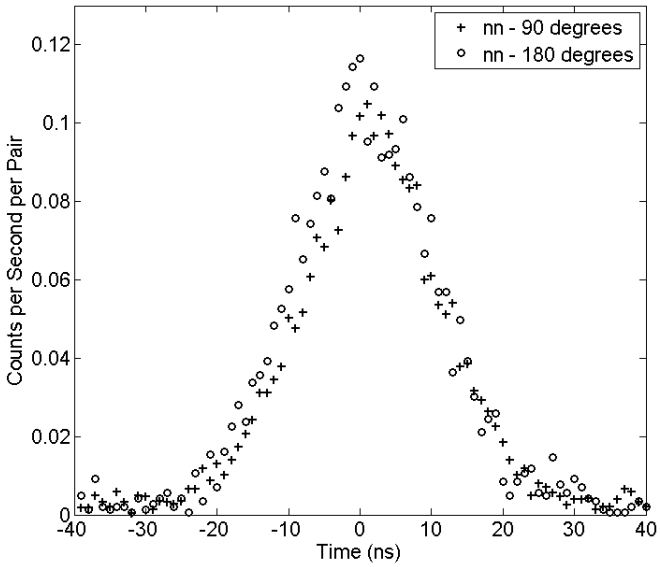

Fig. 5-11. Comparison of neutron-neutron correlations for the 90-degree and 180-degree correlated neutron counts from Pin #2.

5.3. Validation of MCNPX-PoliMi

In addition to understanding the measured results, it is important to use the measurements to verify the validity of the Monte Carlo simulation methodology. MCNPX-PoliMi and its post-processing algorithm are able to simulate realistic detector response.

Table 5-3. Averaged differences between PHD simulated and measured values for data collected at INL and JRC.

Sample	PHD Average Absolute Difference (%)	Cross-correlation Average Absolute Difference (%)
MOX Pin#1	13.0	19.3
MOX Pin#2	20.0	35.0
MOX Powder	22.6	30.0
^{252}Cf	1.4	19.3
Am-Be	15.4	11.0

Fig. 5-12 is an absolute comparison between measured and simulated neutron PHDs. Good agreement is noted between the two curves: average differences are shown in Table 5-3 ranging from 1.4 to 22.6 %. This comparison confirms MCNPX-PoliMi's ability to provide not only accurate simulation of the detector response but also of the SF and AN reactions present in MOX fuel. Fig. 5-13 shows a measurement and simulation of

the neutron-neutron correlation curves for all measured samples discussed in this section. Similar agreement between the correlation curves is observed for the measurement and the simulation (between 11.0 and 35.0 % on average).

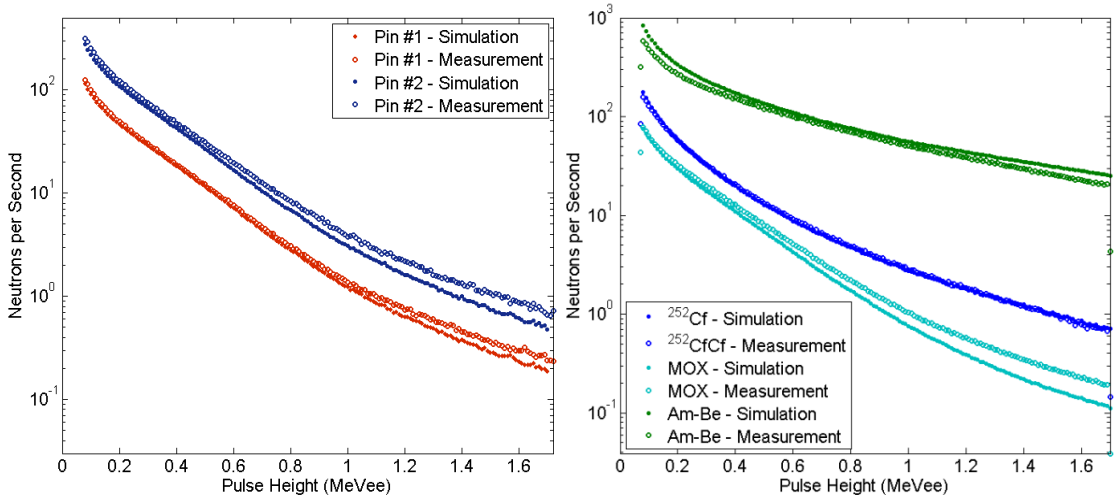

Fig. 5-12. Absolute comparison of simulated and measured neutron PHDs for INL MOX assemblies (left) and JRC MOX/neutron sources (right).

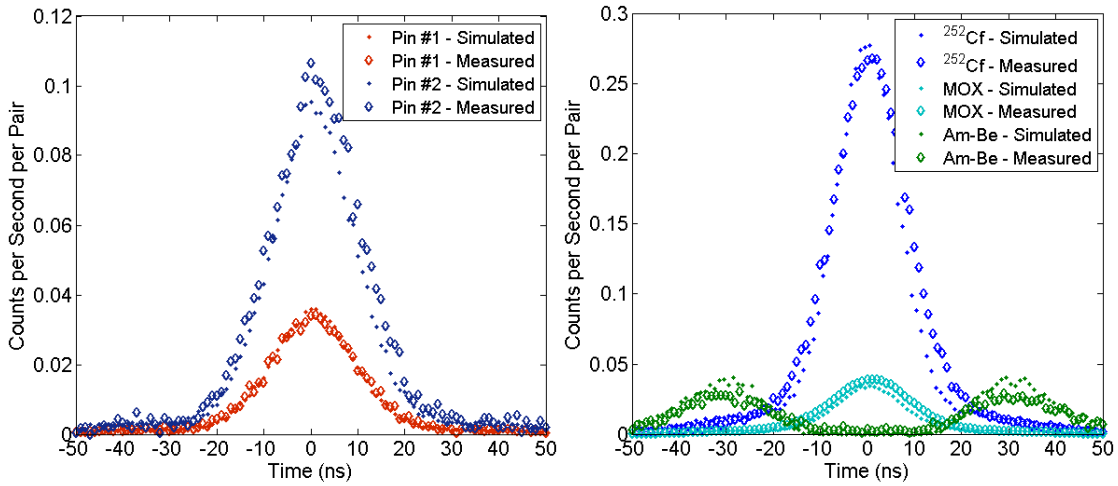

Fig. 5-13. Absolute comparison of neutron-neutron correlation curves for all simulated and measured detector pairs for INL MOX assemblies (left) and JRC MOX/neutron sources (right).

5.4. Summary and Conclusions

This work was a result of detailed simulation and experimental efforts to study MOX samples and standard neutron emitting isotopic sources located at INL and the JRC in Ispra, Italy. The experimental set-ups were derived from detailed Monte Carlo

modeling which incorporated accurate detector response functions. Detailed models of the neutron source from MOX fuels were presented, which included two SF and four AN contributions. The neutron energy spectrum incident on the detectors was determined and studied for its features that may lead to characterization of SNM such as MOX.

Neutron and photon cross-correlation functions were measured for the various experimental configurations. The separate contributions to these functions were discussed and analyzed. The results show that this type of measurement can be used to identify the presence of fission neutrons from MOX fuel and distinguish them from AN neutrons. The ability to differentiate photon and neutron time-correlated events is a novel approach to SNM characterization. Future efforts would benefit from comparing plutonium containing materials with larger variation in isotopic composition and neutron emission.

The Monte Carlo particle transport code MCNPX-PoliMi has the capability to accurately model interactions that are necessary for both of these measurement techniques. Good agreement was obtained between the simulated and measured neutrons. In addition to contributing to the development of an experimental methodology, this study worked as a basis for the validation of the MCNPX-PoliMi code for the development of measurement systems to characterize MOX type fuel assemblies.

Chapter 6. Active Neutron-Correlation Measurements

Fissile materials are of interest in the nuclear safeguards field because they help provide energy across the world, but can also be used in nuclear weapons. Methods of verifying the peaceful use of these materials rely on measuring the presence of fissile material and/or confirming that no significant quantities of known materials have been diverted. When it comes to measuring plutonium, the material's spontaneous fission probability is quite high allowing passive neutron measurements for material characterization. Contrarily, passive measurements are often impractical when quantifying uranium, considering the spontaneous fission yield of all uranium isotopes is quite low; therefore we must rely on measuring induced fission. As a result, active-interrogation techniques are required for characterizing nuclear fuels containing only uranium, as is common in many nuclear facilities around the world [28].

6.1. Characterizing Uranium-Oxides with Liquid Scintillators

Using the simulation tool MCNPX-PoliMi, a detection system was designed to measure induced-fission neutrons from ^{235}U and ^{238}U. Measurements were then performed in the summer of 2011 at the JRC in Ispra, Italy. Low-enriched uranium (LEU) samples were interrogated and induced-fission neutrons were measured to characterize the samples in terms of their uranium mass and enrichment. The measurement system included high-energy neutron (14.1 MeV; deuterium-tritium reaction) and low-energy neutron (0.23 MeV; moderated Am-Li source) active-interrogation sources. The purpose of the measurement campaign was to investigate the potential applicability of using organic liquid scintillators with active-interrogation techniques to characterize uranium containing materials. Additionally, MCNPX-PoliMi simulation results will be compared to the measured trends to validate the MCNPX-PoliMi code when used for active-interrogation simulations.

6.1.1. Description of Measured LEU

Three well-characterized LEU samples were available for experiments at the JRC. Table 6-1 outlines the variation of these samples in terms of their uranium mass and enrichment. Through the use of active interrogation, we see the differences in uranium mass and ^{235}U enrichment by inducing fission in these three materials. The neutron-induced fission cross sections for ^{235}U and ^{238}U are shown in Fig. 6-1 [24]. Based on these cross sections, a varying induced fission response is seen by probing the three LEU samples separately with both slow and fast neutrons.

Table 6-1. Material specifications for the three LEU samples studied at the JRC.

Sample	Uranium Mass [g]	Uranium-235 Mass [g]	Enrichment [%]
LEU-1	1691.93	16.60	1
LEU-2	2374.40	73.83	3.1
LEU-3	2374.96	118.19	5

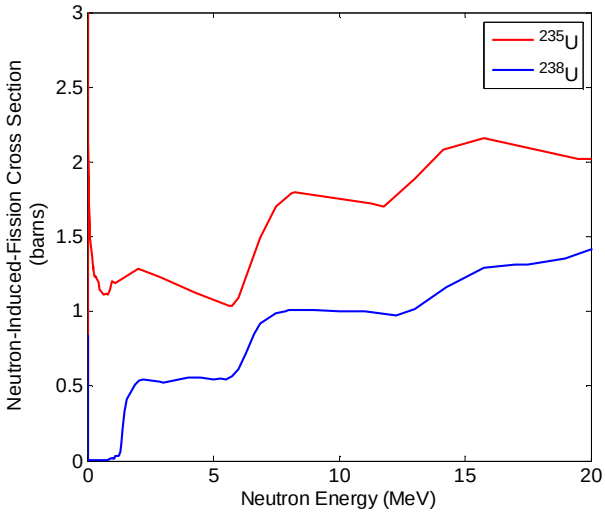

Fig. 6-1. Neutron-induced fission cross sections for ^{235}U and ^{238}U for fast neutrons. The ^{235}U cross section increases at thermal and epithermal energies while the ^{238}U cross section decreases significantly.

6.2. Active-Interrogation Simulations

Using MCNPX-PoliMi, a system was designed to measure induced-fission neutrons from ^{235}U and ^{238}U. The system made use of a deuterium-tritium (DT) neutron generator for inducing fission in the uranium. The generator was equipped with an alpha detector to determine the time and direction of neutron emission. The liquid scintillators

then measured the emitted fission neutrons while minimizing the measurement of transmitted and scattered DT neutrons. As shown in Fig. 1, the DT neutrons will induce fission in both ^{235}U and ^{238}U, providing information on the overall amount of uranium present. DT neutron generators always emit some neutrons at 2.45 MeV due to deuterium impurities in the tritium target leading to deuterium-deuterium fusion. In addition, the actual DT-neutron energy depends on the angle of the emitted neutron. These lower energy (yet still fast) neutrons still arrive in a region of the induced-fission cross sections where there is a large separation between ^{235}U and ^{238}U. To learn about the enrichment of the uranium, we must probe the source at very low neutron energies (ideally thermal) to study only the ^{235}U presence in the LEU. To do this, a high-density polyethylene moderated Am-Li source (0.23 MeV neutrons on average after moderation) was used as an additional interrogation source.

6.2.1. Neutron Interactions in LEU

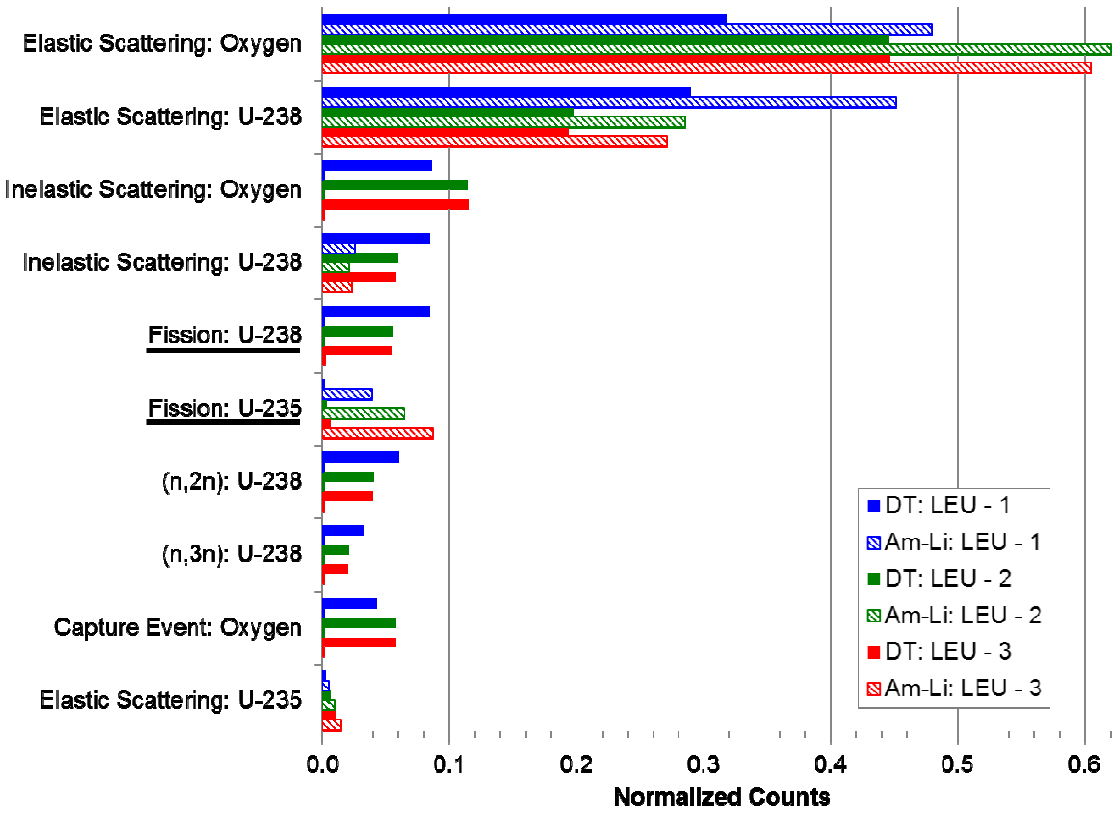

Fig. 6-2. Simulated neutron-interaction probabilities from the three interrogated LEU samples.

MCNPX-PoliMi output includes a detailed history of all of the interactions that happen within a volume of interest, including all of the histories of subsequent particles that are created. By simulating active-interrogation cases and specifying the LEU sample as the volume of interest, we can gauge the usefulness of different active sources to characterize a particular quantity of interest. Fig. 6-2 depicts the types of interaction a DT neutron source and an Am-Li neutron source induce within the three LEU samples that were measured.

6.2.2. Models for Mass and Enrichment Studies

The DT generator emits neutrons in a 'time-tagged cone' at the side of the LEU canister. The detectors were placed directly above the LEU sample outside of the cone of 'timed-tagged' neutrons. Five detectors were used to maximize the measurement statistics while keeping detectors spaced far enough apart to decrease the detector cross-talk. Fig. 6-3a shows the MCNPX-PoliMi model for the DT interrogation case. For the Am-Li interrogation case, the radionuclide source was surrounded by polyethylene moderator and placed under the LEU sample in order to minimize the direct contribution of Am-Li neutrons and primarily measure photons and neutrons that are created in the LEU from the incident Am-Li particles, as shown in Fig. 6-3b.

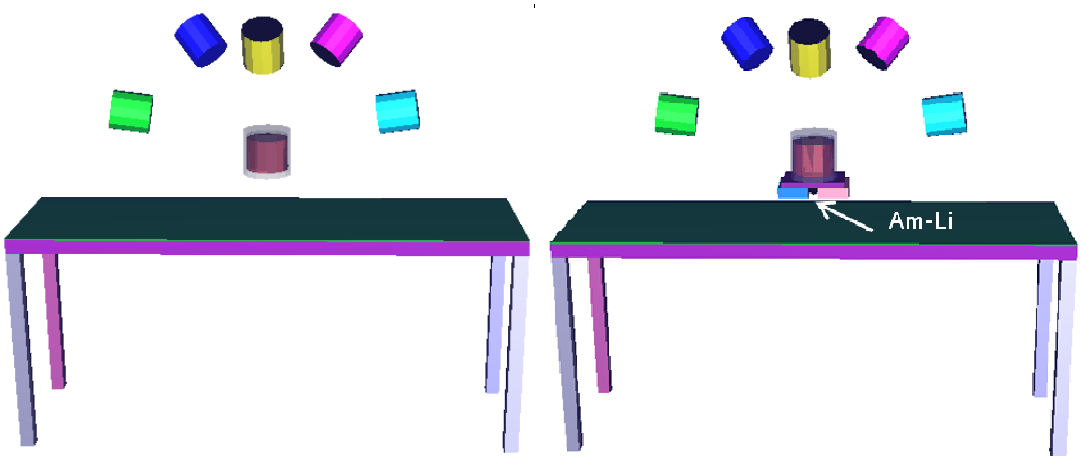

(a) (b)

Fig. 6-3. MCNPX-PoliMi model of the five liquid scintillators (~35 cm from the center of the LEU sample) measuring induced-fission neutrons for the DT interrogation case (a) and the moderated Am-Li interrogation case (b).

6.3. Active-Interrogation Measurements

Fissions were induced with an associated particle DT generator and a moderated radionuclide Am-Li source. The fission neutrons, as well as neutrons from (n, 2n) and (n, 3n) reactions, were measured with five cylindrical 12.7 cm ø by 12.7 cm^3 EJ-309 organic liquid scintillators. The DT neutron generator was available as part of a measurement campaign in place by Padova University [29]. Fig. 6-4 shows two photographs of the measurement configuration.

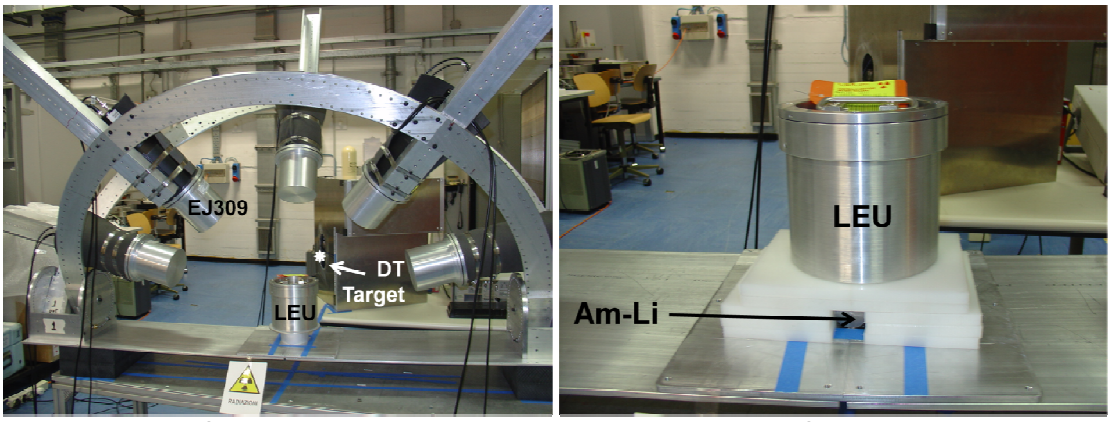

Fig. 6-4. The five-detector geometry positions the liquid scintillator faces at approximately 35 cm from the top of the LEU canister. The associated particle tagged DT neutrons are emitted in the direction coming out of the page. Also shown is the moderated Am-Li source placed under the LEU canister.

6.3.1. Data Acquisition and Analyses

The measurement and data-acquisition system utilized a CAEN V1720 digitizer (12-bit, 250-MHz) and PSD algorithms to differentiate neutron and photon events. The digitizer has eight channels, six of which were used: one for the DT generator's associated alpha detector and the remaining five for the liquid scintillators. The three LEU samples of varying mass and enrichment, shown in Table 6-1, were interrogated separately with the high-energy and low-energy neutron sources. Acquired TOF curves were then analyzed to draw relationships between detected neutrons and sample mass and enrichment.

The PSD algorithm, applied above a 75 keVee threshold (~0.7 MeV neutron energy), is important to isolate the neutron signal that comes from the induced fission, (n, 2n), and (n, 3n) neutrons. Presence of (n, 2n) reactions require greater than ~5 MeV incident neutrons while (n, 3n) reactions require more that ~11 MeV incident neutrons,

therefore only the DT interrogation cases will result in such a signal. In the DT interrogation case, PSD allows the removal of photon accidentals in the neutron TOF distribution. In the Am-Li interrogation case, PSD is more important as it allows us to identify the photon-neutron correlations that are studied here as a pseudo-TOF method. The PSD technique for the DT measurements and the Am-Li measurements is portrayed in Fig. 6-5. The effect of photon misclassification is more significant with the Am-Li measurement configurations due to the strong photon emission inherent in the interrogating source; this can be seen in Fig. 6-5.

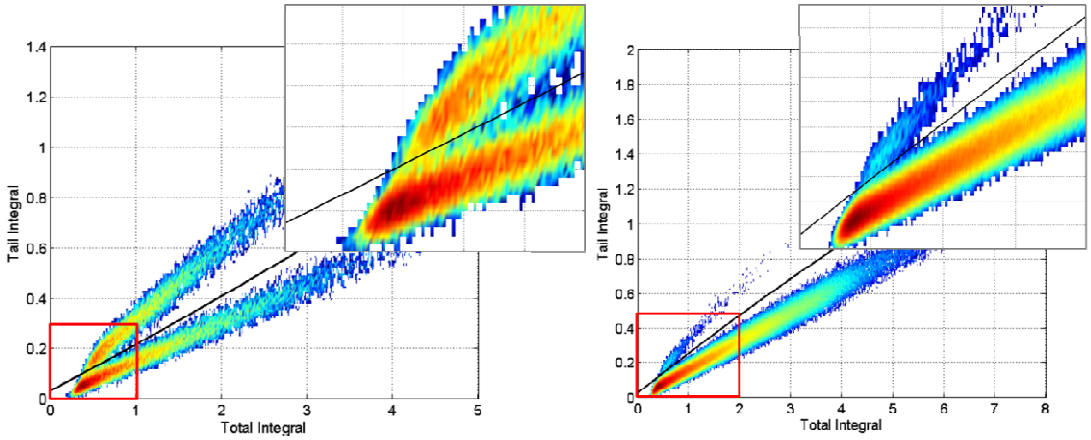

(a) (b)

Fig. 6-5. PSD technique applied to a) the DT interrogated LEU-3 measurements and b) the higher photon flux of the Am-Li interrogated LEU-3 measurements where the neutron events fall above the discrimination line.

6.4. Uranium Mass Investigation

When using the associated particle DT generator, an alpha detector provides a signal when a DT event emits a neutron in the direction of our LEU sample. By using this signal as a trigger, a TOF measurement can be performed, thus measuring the arrival time of particles created in the LEU sample. The triggering alpha detector is a YAP scintillation detector that is known to display good timing properties [29]. The distance between the LEU sample and the five detectors (~35 cm) must be chosen to provide adequate separation between the arrival of the photons and the arrival of the fast neutrons.

6.4.1. Simulation Results

Fig. 6-6a shows the simulated TOF results for the DT interrogated LEU samples. The photon signal can be eliminated and we can focus on the change in the neutron TOF curves for the three LEU samples. The neutron TOF curve in Fig. 6-6a shows variations in slope along the leading edge (25 – 30 ns), it is in this location that 14 MeV neutrons elastically scatter on the LEU, lose very little energy, and arrive quickly at the detectors and create a pulse by depositing less than 2 MeV (the upper limit of the data acquisition). The TOF curves showed that the mass of the LEU sample would trend with the amount of induced fission events, (n, 2n), and (n, 3n) events for samples of similar geometry. Therefore, the integrals of these neutron TOF curves provide information on the sample mass, as shown in Fig. 6-6b.

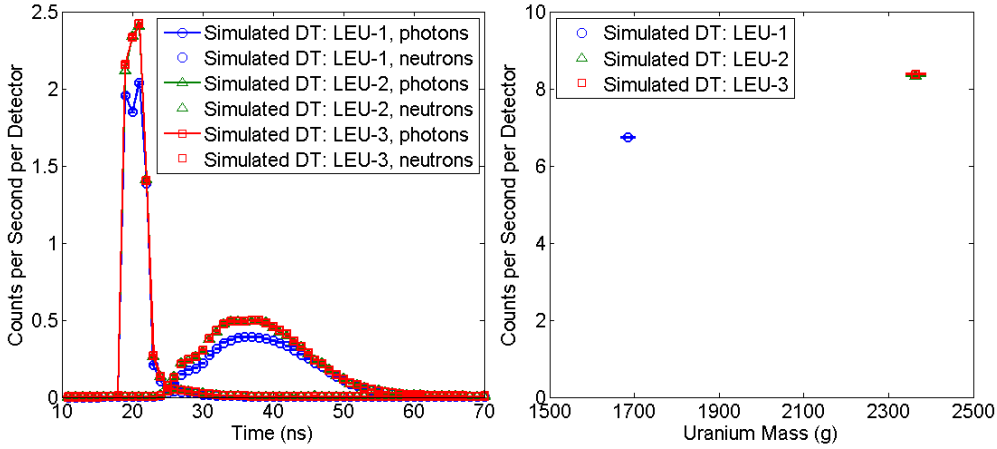

(a) (b)

Fig. 6-6. a) Simulated photon and neutron TOF curves for time-tagged DT interrogation of the three LEU samples with error bars that are smaller than the data point symbols, and b) the trend of the total neutron counts with uranium mass where the LEU-2 and LEU-3 points are overlapping.

6.4.2. Experimental Results

Fig. 7a shows the measured neutron TOF curves for the DT interrogated LEU samples, including statistical uncertainty. Fig. 6-7b shows the trend in the total neutron counts with uranium mass. The neutron counts trend appropriately with uranium mass, with the two canisters of equal mass having approximately the same neutron TOF response for the DT interrogation case.

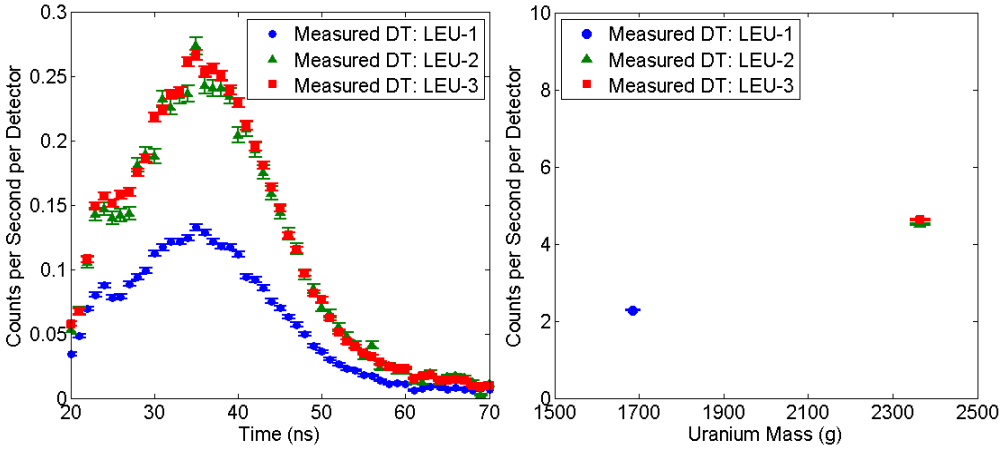

(a) (b)

Fig. 6-7. a) Measured neutron TOF curves for time-tagged DT interrogation of the three LEU samples and b) the trend of the total neutron counts with uranium mass.

6.5. Uranium-235 Enrichment Investigation

Fig. 6-8 shows the results of the ^{235}U enrichment investigation, where the moderated Am-Li neutrons will induce fission primarily in ^{235}U. The ^{235}U fission neutrons' TOF will be measured in the liquid scintillators by triggering on the photons produced during the induced nuclear interactions.

6.5.1. Simulation Results

The pseudo-TOF curves for the simulated Am-Li cases are shown in Fig. 6-8a. The relationship between the enrichment and these three curves is shown in Fig. 6-8b.

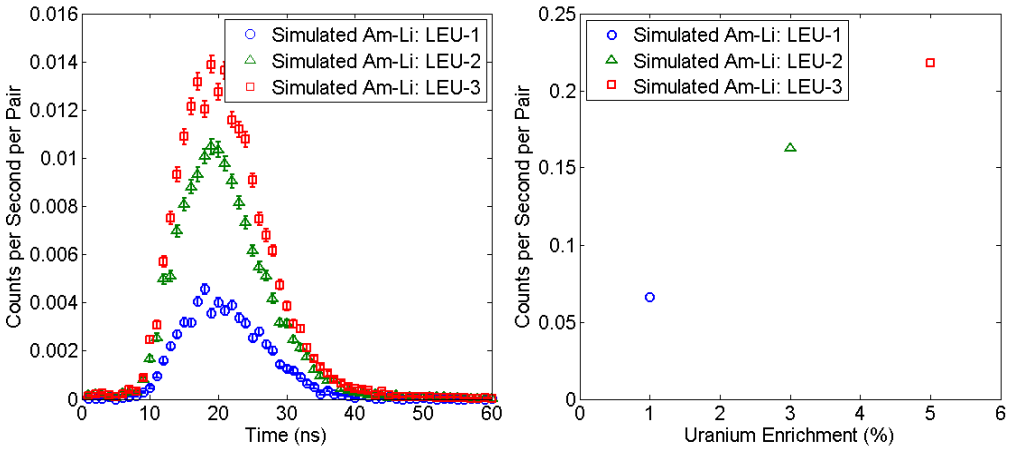

(a) (b)

Fig. 6-8. a) Simulated photon-triggered neutron TOF curves for the moderated Am-Li configurations and b) the trend of the total photon-neutron correlations with U-235 enrichment.

6.5.2. Experimental Results

Fig. 6-9a shows the measured photon-neutron correlations for the Am-Li interrogated LEU. Fig. 6-9b shows the trend of correlations with LEU enrichment. It is difficult to directly compare the LEU-1 sample to the LEU-2 and LEU-3 samples, as the mass is not consistent, although the general trend agrees with what is expected. The relationship between neutron counts and both uranium mass and enrichment follow the MCNPX-PoliMi predicted trends. The trends between the simulated (Fig. 6-8b) and measured (Fig. 6-9b) neutron counts versus enrichment are very similar, with the primary difference being in the vertical magnitude of the entire curve, as the simulations under-predict the system response. This non-linear behavior of the counts with enrichment (or mass) is rather typical of all active measurements with low energy Am-Li sources; the trend is due to the limited penetration of neutrons in the material that reduces the fraction of the sample that is interrogated when the sample size increases.

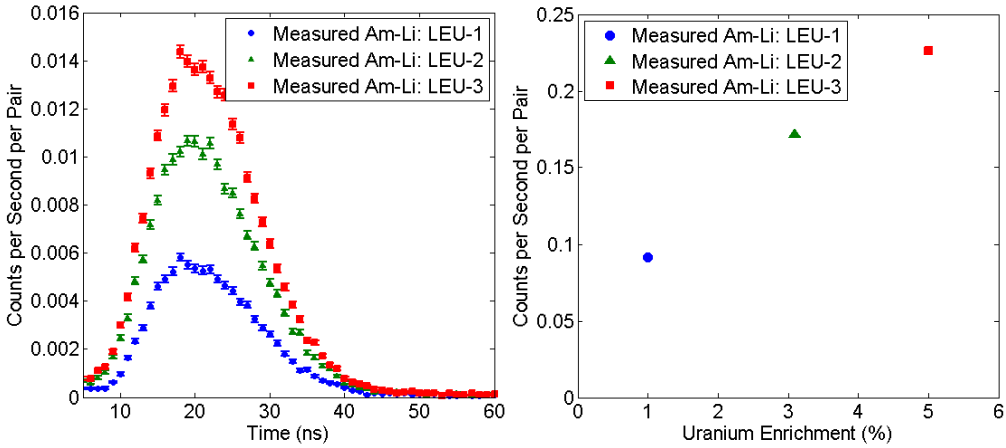

Fig. 6-9. a) Measured photon-triggered neutron TOF curves for the moderated Am-Li configurations and b) the trend of the total photon-neutron correlations with ^{235}U enrichment (with error bars smaller than that data point symbols).

6.6. Validating MCNPX-PoliMi/MPPost for Active-Interrogation Applications

MCNPX-PoliMi was used to design the measurement system and could further be used to optimize such a measurement system and extend its applicability. In order to use the simulation package for such activities, it is helpful to validate the simulated active-interrogation scenarios with the measured results.

Initially, a passive ^{252}Cf-source correlation measurement was performed with a well-characterized source to be compared with an MCNPX-PoliMi-simulated measurement. Good agreement has been observed between different organic liquid scintillation measurement systems and ^{252}Cf sources in the past. These past observations are consistent with the present measurement system, as shown in Fig. 6-10, where the cross-correlation distributions from the measurement and the simulation agree well. The peaks in the measured neutron-photon and photon-neutron distributions near time zero are primarily due to PSD misclassification of photons as neutrons. A relative small amount of measured data was collected for the ^{252}Cf source, hence the statistical fluctuations in the measured results.

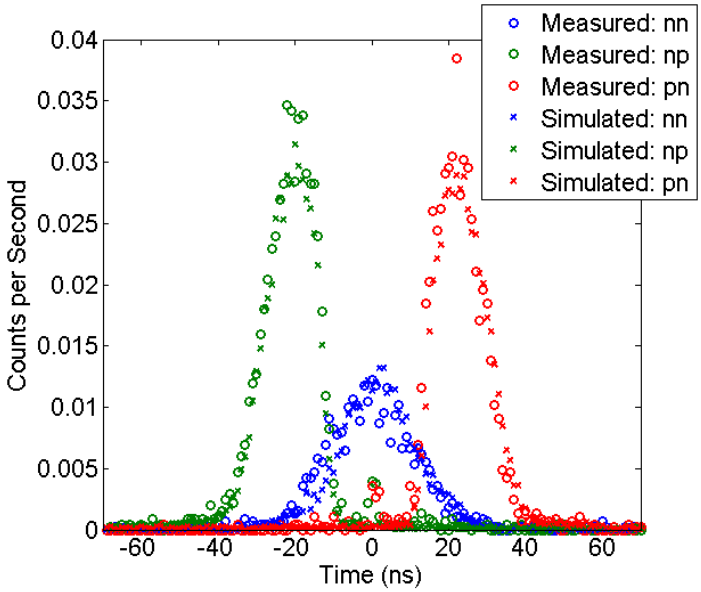

Fig. 6-10: Measured and MCNPX-PoliMi-simulated cross-correlation distributions for a single detector pair in conjunction with a bare ^{252}Cf source.

Due to the uncertainties associated with the use of the DT generator, it is difficult to make an absolute comparison between the simulation and measured results. Much of the error lies in details associated with the alpha trigger detector (YAP scintillator), including the poor knowledge of the detector's orientation and thus the neutron-beam diameter at the LEU sample, the inability to distinguish between photon and alpha events in the detector leading to accidental correlated events in the measurements, the instability of the neutron generator output, and the unknown location of the neutron-event threshold. Due to the proprietary nature of the use of the DT generator, all these unknowns could

not be resolved. These uncertainties can be minimized with a better characterized DT-generator/measurement system.

When considering active-interrogation simulations, more successful comparisons are made between the simulated and measured Am-Li cases. Previous work with Am-Li sources demonstrated better correlation results when neutrons from Am-Be and AmO_2 radionuclide sources were included in the source model [30]. The true 'contaminant' levels were unknown and therefore the Am-Be and AmO_2 neutron sources were added to better match a measured neutron PHD of the Am-Li interrogation source. The simulated Am-Li source was defined with 1.2% of the total neutron emission originating from an Am-Be neutron source and 1% from an AmO_2 source.

Figure 6-11 shows the MCNPX-PoliMi simulations and measurements of the TOF distributions of the LEU sample with moderated Am-Li. The simulated measurement TOF distribution behaves similarly to the measurement results but with lower count rates across the entire distribution. The simulation likely under-estimates the count rate due to uncertainties in the source activity, the source spectrum, un-modeled details of the surroundings and the high-density polyethylene density.

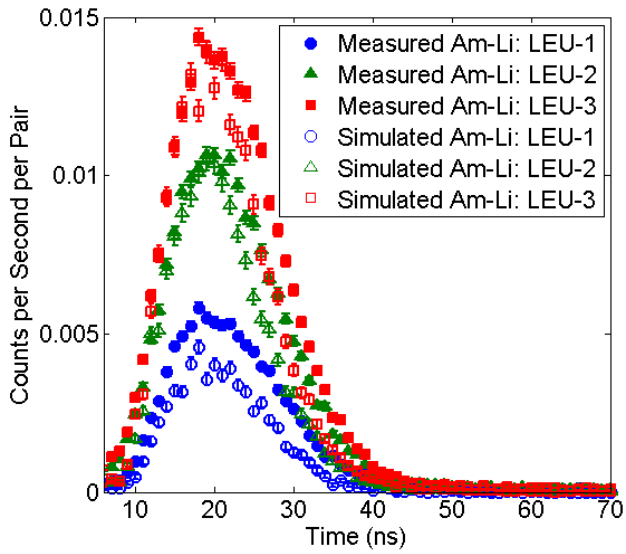

Fig. 6-11. Absolute comparison of measured and simulated TOF distributions for the moderated Am-Li configurations.

6.7. Summary and Conclusions

An active-interrogation measurement and simulation campaign was performed with the aim of characterizing uranium-containing materials. Active-interrogation methods were investigated, including a DT generator and a moderated Am-Li source. Time-correlation techniques were used to measure neutron-induced fission in LEU powder samples. MCNPX-PoliMi was used for the system design and understanding of the measured trends.

It was observed that 14.1 MeV neutrons induced fission in ^{235}U and ^{238}U isotopes, allowing the total uranium mass to be determined from neutron TOF measurements. Then, the supplemental use of low-energy neutrons from a moderated Am-Li source to induce fission in primarily ^{235}U, allowed conclusions as to the relative ^{235}U enrichment.

The standard charge integration PSD method appropriately discriminated photon events from neutron events in the liquid scintillators. This approach allowed the thorough analysis of neutron TOF distributions with the ability to eliminate photon accidentals. It also allowed pseudo-TOF distributions to be formed from the Am-Li interrogation cases by triggering on the photons that are emitted from the nuclear reactions in the LEU. It would be beneficial to investigate a broader range of uranium-containing materials. With more information on the response of a liquid scintillators system, advanced algorithms can be developed to quantify ^{235}U enrichment and uranium mass.

Chapter 7. Passive Neutron-Multiplicity Measurements

Typical of fission reactions is the emission of multiple neutrons simultaneously. Therefore, instrumentation that measures neutron multiplicity is an excellent way to quantify the amount of fissionable material present. Neutron multiplicity counters are common in nuclear safeguards efforts using ^{3}He detectors. Neutron detectors containing ^{3}He have a high efficiency for neutron detection when neutrons are moderated to thermal energies. Well established theory to analyze the signals (neutron coincidence or multiplicity) that come from systems containing many ^{3}He detectors provides values such as the mass of SNM. Measurement of mass with low uncertainty is needed to verify nuclear-material declarations.

Neutrons emitted from fission are not in fact thermal and organic scintillators have good efficiency over the range of fission neutrons, as discussed in Sect. 4.3. Additionally, organic scintillators are inherently fast and solve problems associated with dead time in traditional systems. An FNMC addresses the urgent need to innovate ^{3}He alternative systems to meet future safeguards needs and expand the scope of current safeguards measurement systems.

In the efforts to develop an FNMC at the UM, a small-scale system was developed for proof-of-concept simulations and measurements. The system made use of liquid organic scintillation detectors for fast-neutron detection of fissile materials. Such a system is expected to quantify small masses of plutonium inventory using neutron coincidence. MCNPX-PoliMi/MPPost codes were being used for the full-system design and therefore validation with a small-scale system was necessary to proceed with the design process. The validation measurements were performed on nuclear materials at the JRC in Ispra, Italy in April of 2012. The measurements highlight neutron coincidence with liquid scintillators and their potential to determine plutonium mass.

7.1. Simulating Neutron Multiplicity

The radiation source and the experimental geometry were modeled with MCNPX-PoliMi. Two different types of nuclear materials were measured and simulated, a MOX powder and PuO_2 pellets. Two MOX samples and nine PuO_2 pellets were studied. The two MOX samples and three combinations of the nine PuO_2 pellets were measured to represent five different ^{240}Pu effective ($^{240}Pu_{eff}$) masses. Equation 7-1 defines traditional $^{240}Pu_{eff}$ mass as a function of the masses of the even-numbered plutonium isotopes [5].

(7-1)

Built-in MCNPX-PoliMi sources were used to simulate the neutron and photon sources present in the samples containing both plutonium and oxygen: ^{240}Pu and ^{242}Pu spontaneous fissions and ^{238}Pu, ^{239}Pu, ^{240}Pu, and ^{241}Am (α, n) reactions. Figure 7-1 shows the make-up of the neutron source for both the PuO_2 and MOX samples. Negligible neutron sources (including ^{238}Pu spontaneous fission), contributing only 0.75% of the total neutron emission, were omitted. For all of the five configurations, detailed information was recorded for four organic scintillation detectors. These data were then analyzed using MPPost to arrive at PHDs and fast-neutron multiplicity.

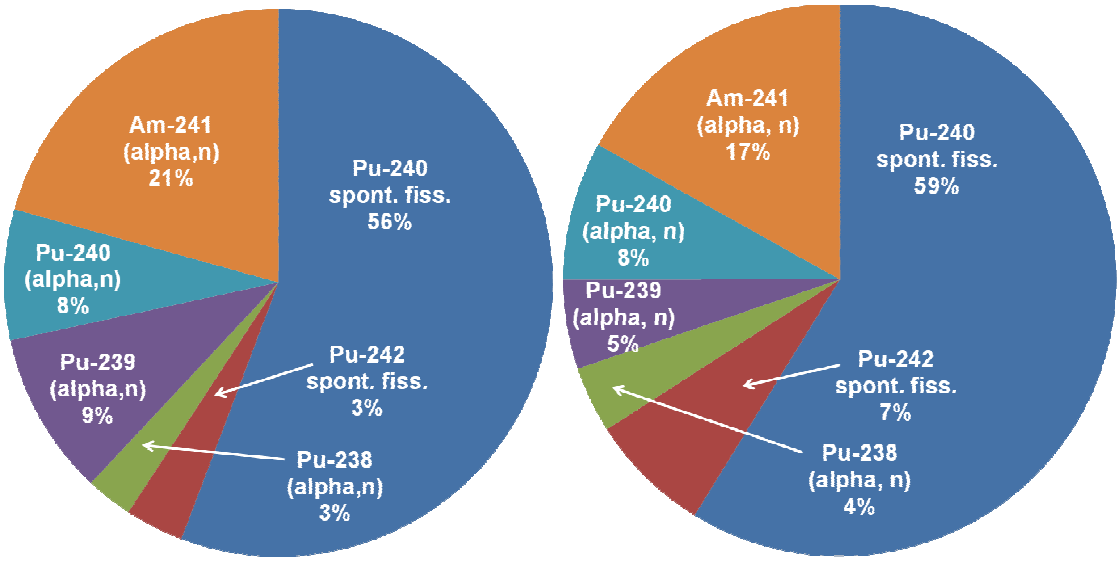

Fig. 7-1. The neutron-source contributions for the PuO_2 pellets (a) and MOX samples (b) measured at the JRC facility.

7.2. Measurement of Fast-Neutron Coincidence with Liquid Scintillators

At the JRC's Laboratory, a UM measurement system (Fig. 7-2) was utilized to measure fissile materials and the measurements were then simulated with MCNPX-PoliMi/MPPost. The data were valuable to test data-analysis algorithms for their potential and limitations. Benchmarking the simulation efforts with the measured results built confidence in the use of simulation and modeling tools, specifically MCNPX-PoliMi/MPPost, to facilitate a design process for the development of an FNMC. Such a measurement system would contain numerous standard liquid scintillators; specifically Eljen Technology manufactured EJ-309s. Additionally within the system, a small amount of lead shielding was used to reduce the photon flux from the samples.

Fig. 7-2. All experimental configurations included four 7.62 cm ø x 7.62 cm liquid scintillators 20 cm from the center of the measured samples. The configuration depicted includes nine PuO_2 pellets with 0.25 cm of lead shielding present, measured with a 70 keVee LO threshold.

7.2.1. Description of Plutonium-Containing Materials Measured

By measuring PuO_2 and MOX samples of varying mass, the trend between neutron doubles rate and plutonium mass was assessed. This trend provides a value that will work as a sensitivity-metric for the design process. The measured plutonium masses included PuO_2 pellets, ranging from 20 to 60 g, and MOX samples, 160 and 190 g, with details outlined in Table 7-1.

Table 7-1. Isotopic masses for the measured PuO_2 pellet combinations and MOX samples.

Sample: Isotope	PuO_2-1 (g)	PuO_2-2 (g)	PuO_2-3 (g)	MOX-1 (g)	MOX-2 (g)
^{234}U	--	--	--	0.05	0.06
^{235}U	--	--	--	4.79	5.50
^{236}U	--	--	--	0.05	0.06
^{238}U	--	--	--	670.50	769.48
^{238}Pu	0.02	0.03	0.04	0.24	0.27
^{239}Pu	14.24	39.66	52.33	111.81	127.02
^{240}Pu	5.39	9.31	11.26	47.00	53.39
^{241}Pu	0.13	0.23	0.27	1.67	1.90
^{242}Pu	0.29	0.37	0.41	3.38	3.84
^{241}Am	0.80	1.33	1.59	5.12	5.82
O	2.75	6.75	8.74	166.22	184.00
Total	23.63	57.68	74.65	1010.83	1151.33

A ^{252}Cf source was also measured for validation purposes. The measured materials are similar to those measured in low-level plutonium-sample inventory counters and helped provide insight into how organic scintillation detectors can find use in characterizing such materials. The measurement system used in this study uses only a fraction of the number of detectors an ideal prototype would contain.

7.2.2. Measurement System

To achieve portability, the measurement campaign in April 2012 used a 4-channel USB digitizer (CAEN DT5720) and a data-acquisition laptop to acquire data from four detectors (7.62 cm ø by 7.62 cm EJ-309s). These scintillators detect both neutrons and photons via scattering events in the hydrocarbon material; both particle types create pulses that are digitized, and kept for data analysis. The digitizer has a 12-bit resolution (11-bits effective) and a 250-MHz sampling frequency which is sufficient to identify the slight pulse-shape difference between the two types of interactions via PSD algorithms, shown in Fig. 7-3.

Due to the high photon emission from plutonium-containing materials, a thin lead shield (0.25 cm for PuO_2 and 1 cm for MOX) was also present. The detectors were placed at 20 cm from the center of the source and were arranged in a small arc with approximately 30 degrees between each detector.

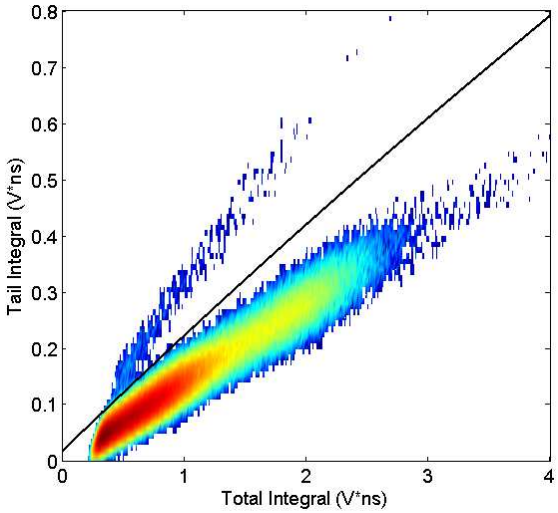

Fig. 7-3. Measured neutrons (upper region) and photons (lower region) from the shielded PuO_2 source measured at a 70 keVee light-output threshold (approximately 650 keV neutron energy deposited). A discrimination curve is shown that was used the separate neutrons from photons.

7.2.3. Measurement-Data Analysis

In order to quantify plutonium mass in nuclear materials it is common to rely on the detection of fission rate from a variety of plutonium isotopes. Measuring the fission rate is possible using neutron-multiplicity measurement techniques [5]. Neutron-multiplicity measurements are beneficial due to the emission of multiple neutrons spontaneously from a single reaction, which is unique to fission. In this work, plutonium-mass information will be gathered from the measured neutron doubles rate. Such neutron-multiplicity results were found by counting the coincident fast-neutron events in short time windows (~100 ns) [31]. A constant fraction delay method (with 0.5 as the fraction) is used to identify the arrival time of each pulse. Two PSD-attributed neutrons that arrive within the time window are considered coincident and contribute to the neutron-doubles rate. If a third neutron is detected within the time window the event is considered a neutron triple and does not contribute to the neutron-doubles rate, the same applies for all subsequent higher-order multiples.

7.3. Measurement Results and Validation of MCNPX-PoliMi/MPPost

7.3.1. Measured and Simulated PHDs

Figure 7-4 shows the measured normalized PHDs for the two different types of plutonium and ^{252}Cf. The shapes of these distributions shed light on the type of neutron source that is being measured, for example a plutonium-metal sample will give different PHD results than a PuO_2 sample due primarily to differences in the neutron scattering cross section of the material matrix [32]. This information can prove useful to tailor mass quantification equations to specific nuclear material types. To validate the simulation methodology, Fig. 7-5 shows an absolute comparison (on a linear scale) of neutron PHDs with good agreement between the simulated and measured results from a ^{252}Cf source and one of the configurations of PuO_2 pellets (#2 described in Table 7-1). The average point-by-point agreement between the simulated and measured results are 6.8% and 10.6% respectively, with most of the discrepancy coming from the low LO region where PSD is less accurate.

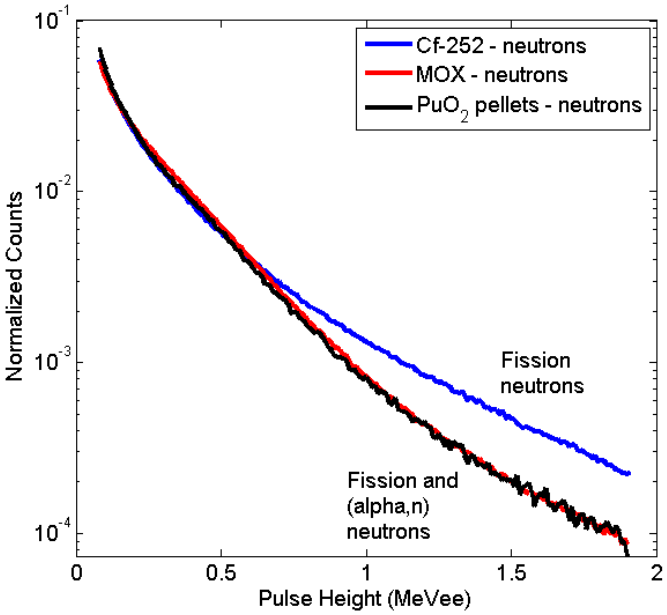

Fig. 7-4. Measured neutron PHDs (normalized to their integral) for ^{252}Cf, MOX, and PuO_2 pellets.

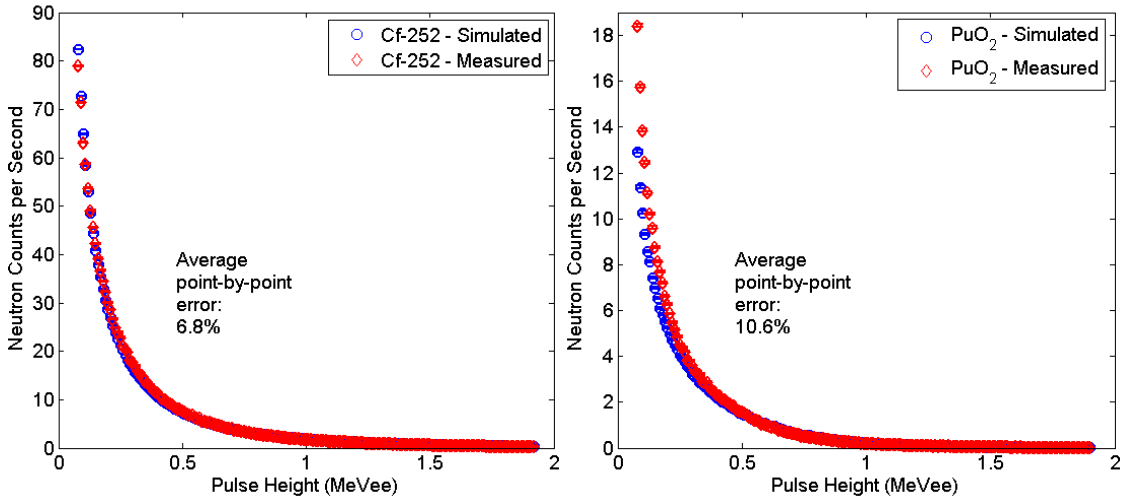

Fig. 7-5. Simulated and measured ^{252}Cf PHDs (left) with an average point-by-point agreement error of 6.8% and simulated and measured PuO_2 PHDs (right) with an average point-by-point agreement error of 10.6%. Statistical errors shown on the data points are smaller than the symbols used.

7.3.2. Neutron Coincidence

Sensitivity and efficiency of the measurement system was studied via the measured doubles rates (neutron coincidence) for PuO_2 and MOX samples, outlined in Table 7-1. Figure 7-6 shows the relationship between the neutron coincidence rate and the $^{240}Pu_{eff}$ mass is linear across all of the PuO_2 and MOX samples.

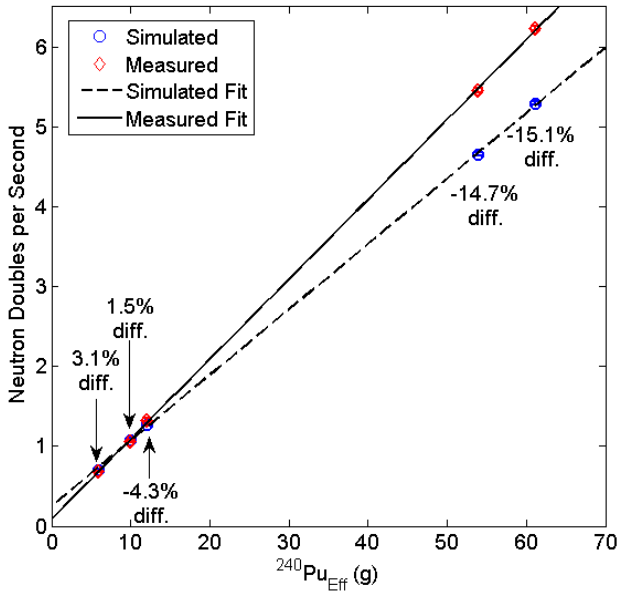

Fig. 7-6. Relationship between simulated and measured neutron doubles rates and $^{240}Pu_{eff}$ mass. Differences listed relate the simulated and measured data while statistical error bars shown on the data points are smaller than the symbols used.

Good agreement is observed for neutron doubles rates over a range of plutonium mass (also shown in Fig. 7-6). The difference between measurement and simulation for the three lower-mass plutonium samples was of the order of a few percent. The difference between the measurement and simulation for the larger masses was approximately 15%. Likely causes for the difference between simulated and measured values are misclassified photon events contributing to the neutron doubles rate and accidental neutron doubles, both forms of inaccuracy artificially 'inflate' the results. Additionally, large uncertainties in our knowledge of the density and volume of the MOX powders contribute to the error in the comparison of simulated and measured doubles. Finding good agreement between the simulated and measured neutron doubles is crucial considering the doubles rate is the result of primary concern for the design process.

Linear trends were independently fit to measured and simulated results. The sensitivity of the system can be characterized by the slope of the relationship. A more sensitive system will display a trend that has a larger slope and a more efficient system will display a trend with a higher overall magnitude. For the bench-top system used at the JRC, the sensitivity based on the measured data was 0.100 ±0.001 neutron doubles per second per gram (the slope of the line fit to the measured data points in Fig. 7-6 where the error is the standard deviation of said linear regression slope). Due to uncertainty in the MOX simulations, the simulated data predict a less sensitive measurement system with a sensitivity value of 0.082 ± 0.001 neutrons doubles per second per gram. Table 7-2 gives the deviation of the doubles rates from the fit for both the simulated and measured data. The results show that the linear fit is a reasonable choice.

Table 7-2. Difference between the data points and the linear fits.

	PuO_2-1 (%)	PuO_2-2 (%)	PuO_2-3 (%)	MOX-1 (%)	MOX-2 (%)
Simulation	-4.75	0.62	2.36	-0.39	0.48
Measurement	0.00	-2.41	2.52	-0.45	0.43

The measurement system had promising absolute efficiencies of 4.20 ± 0.05 % for neutron singles and 0.061 ± 0.001 % for neutron doubles measured with a ^{252}Cf source (error calculations take into account statistical uncertainty, source strength uncertainty, and PSD misclassification). Statistical uncertainty of doubles less than 5% can be achieved in 10 minutes for the smallest measured plutonium mass. This result is

encouraging considering the final system design will include more detectors and cover a significantly larger solid angle.

7.4. FNMC Simulations for Prototype Design

Current simulation efforts focus on studying trends in the detector shape, size, number, and configuration to achieve high efficiency, high sensitivity, and minimal dependence on sample placement. Examples of potential setups are shown in Fig. 7-7. An ideal detector design will not only perform accurately and efficiently, but also maintain a minimally intrusive geometry in terms of size and weight. With a list of candidate designs, bench-top experiments are being performed at UM to work towards fine-tuning the design.

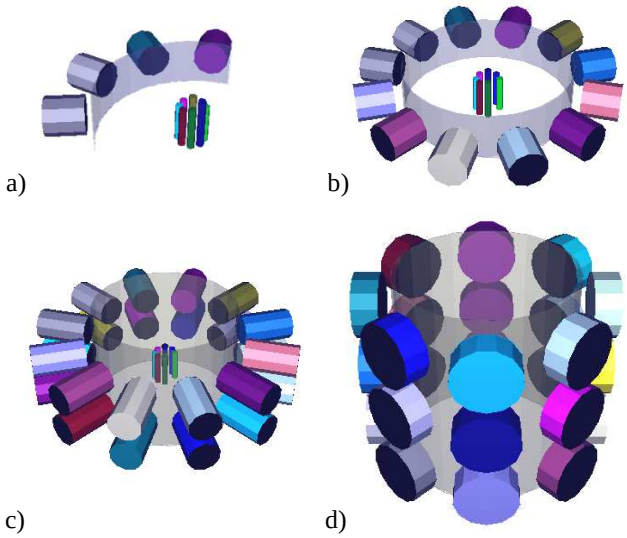

Fig. 7-7. Examples of FNMC models: (a) UM measurement system used in the present work based on EJ-309 liquid scintillators, (b) a full ring (12 detectors) of 7.62 cm ø by 7.62 cm EJ-309s, (c) two rings of 7.62 cm ø by 12.7 cm EJ-309s, and (d) three rings of 12.7 cm ø by 5.08 cm EJ-309s. The models include the active volume of the EJ-309s, 0.25 cm of lead shielding, and PuO_2 pellets.

Using MCNPX-PoliMi/MPPost many detector configurations were tested with numerous types of plutonium-containing materials of varying plutonium mass. We simulated the JRC's PuO_2 pellets as they were measured during the measurement campaign described in this work. Simulated results in Fig. 7-8 show how the doubles rate, from various system designs, trends with increasing $^{240}Pu_{eff}$ mass. Figure 7-9 shows the triples rates versus the $^{240}Pu_{eff}$ mass. Designs included either one, two, or three rings of liquid scintillators. The liquid scintillator dimensions were either 7.62 or 12.7 cm ø

and varied in length between 2.54 to 12.7 cm. The slope of the doubles rate curves shown in Fig. 7-7 is then the sensitivity metric for determining the responsiveness of the simulated systems to plutonium mass. From the three simulated PuO_2 samples, the third point deviates most from a linear trend due to all of the added canister material present for this particular case. The first two cases include one pellet and three pellets respectively, while the third case has nine pellets. The large increase in the steel casing has a small effect on the neutron doubles leading to the slight decrease in expected rate. This noted decrease is not present when the materials are modeled with the absence of their containers.

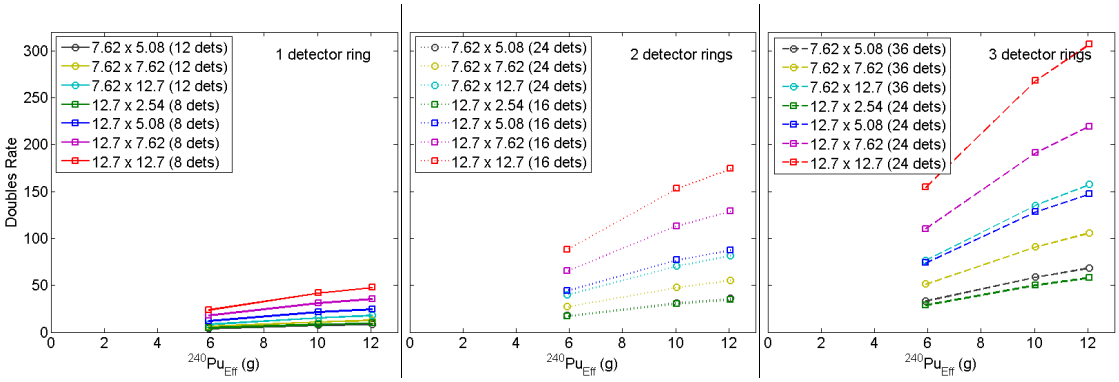

Fig. 7-8. The trend of simulated doubles rates with plutonium mass for 21 FNMC designs. The number of detectors and the detector size were varied. Each figure shows the response for one, two, or three detector rings where the statistical errors are smaller than the symbols used.

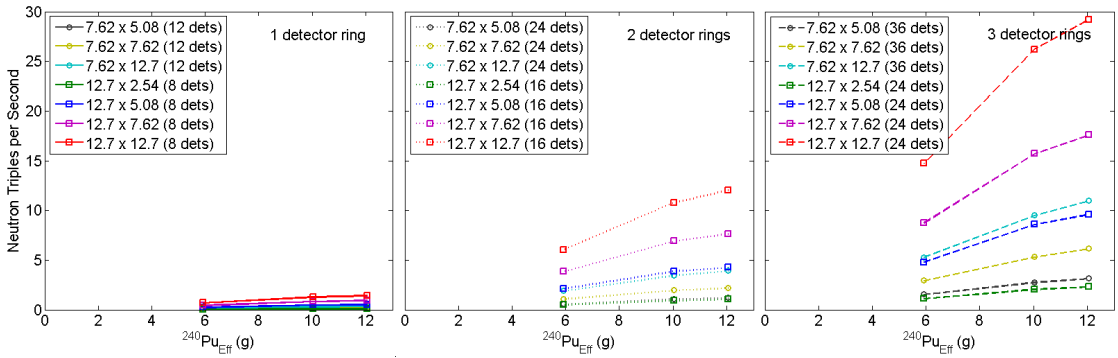

Fig. 7-9. The trend of simulated triples rates with plutonium mass for 21 FNMC designs. The number of detectors and the detector size were varied. Each figure shows the response for one, two, or three detector rings where the statistical errors are smaller than the symbols used.

Table 7-3. The sensitivity of each design portrayed in Fig. 9.

Detector Shape (diameter x length)	Sensitivity (Doubles Rate/g of $^{240}Pu_{eff}$)		
	One Ring	Two Rings	Three Rings
7.62 cm ø by 5.08 cm	0.75 ± 0.05	3.05 ± 0.22	5.81 ± 0.33
7.62 cm ø by 7.62 cm	1.12 ± 0.05	4.68 ± 0.34	8.99 ± 0.55
7.62 cm ø by 12.7 cm	1.55 ± 0.08	6.89 ± 0.47	13.36 ± 0.81
12.7 cm ø by 2.54 cm	0.81 ± 0.08	2.9 ± 0.28	4.81 ± 0.35
12.7 cm ø by 5.08 cm	2.03 ± 0.20	7.21 ± 0.72	12.11 ± 1.01
12.7 cm ø by 7.62 cm	2.93 ± 0.29	10.61 ± 0.99	18.05 ± 1.49
12.7 cm ø by 12.7 cm	3.94 ± 0.38	14.29 ± 1.38	25.3 ± 2.08

Table 7-3 gives the sensitivity of each of the designs. As expected, systems that cover the most solid angle and have the greatest detector volumes perform best. The simulated triples rates embody the same trends as the doubles curves, while providing an order of magnitude less counts and sensitivity. Additionally, the percent increase of neutron triples events per gram is consistent with what is seen with the neutron doubles trends.

The design with three rings of 12.7 cm ø by 12.7 cm detectors performs best, as it yields the highest doubles rate, resulting in the lowest uncertainty on the $^{240}Pu_{eff}$ mass, and also has the largest size and weight. A system with two rings of detectors 7.62 cm ø by 7.62 cm is more manageable and the sensitivity does not decrease significantly. By decreasing the detector depth, less cross-talk events are present in the neutron doubles. Additionally, the smaller liquid cells (such as the 7.62 cm ø by 7.62 cm detectors) provide better timing and PSD capabilities than larger cells (12.7 cm ø by 12.7 cm detectors). This trend is further confirmed for much larger volumes that have been previously studied [33]. In fact, detectors with cells having large volume suffer from light attenuation and degradation of the PSD performance, requiring a higher LO threshold, resulting in lower overall system efficiency. Cylindrical-shaped detector volumes with matching photo-multiplier tubes were chosen throughout the design process for their optimal light collection and PSD performance, providing an improvement over past designs in both efficiency and uncertainty [34].

7.5. Summary and Conclusions

Results on neutron coincidence measurements of PuO_2 and MOX with liquid scintillators were thoroughly studied. Specifically, the potential of a FNMC to determine plutonium mass with neutron coincidence was evaluated. The results show that liquids are a strong candidate for plutonium mass characterization. These measurements also allowed the opportunity to validate simulations performed with the MCNPX-PoliMi/MPPost simulation tools.

Based on the measurement results liquid scintillators appear to be a good candidate for a FNMC. Fast-neutron doubles rates (from multiplicity) trend linearly with $^{240}Pu_{eff}$ mass in PuO_2 and MOX samples. A small four-detector system showed a sensitivity of 0.100 ± 0.001 neutron doubles per gram per second. Simulations of larger systems proved that the sensitivity can increase up to values such as 25.30 ± 2.08 with increased detector size and numbers. The measured doubles efficiency for the four-detector system was 0.061 ± 0.001 %.

Neutron PHDs can aid in neutron multiplicity system calibration via specific source type characterization (fission sources only versus fission and (α, n) sources, e.g. metal versus oxide). In this study measurements only included PuO_2, future efforts will include an expansion of the material types that are measured and how they fit into the current mass characterization method.

The agreement between the fast-neutron measurement system's simulation and experimental campaigns was less than 5% difference for the PuO_2 pellets doubles rates and ~15% difference for the MOX samples doubles rates. Neutron pulse-height analysis had good agreements for ^{252}Cf (a commonly used validation source) and the PuO_2 pellets at 6.8 and 10.6% error, respectively. These results validate the use of the MCNPX-PoliMi/MPPost package for designing a FNMC. Both the simulated and measured data fit well to linear trends. The quality of the linear fits to both simulated and measured data validate using neutron doubles rates per gram of $^{240}Pu_{eff}$ to design a sensitive system and potentially quantify mass in a FNMC for materials of low multiplication.

Simulation efforts to design a full FNMC show that high levels of efficiency, sensitivity, and expedient measurement times can be achieved by increasing the number of detectors and the overall detection volume. The challenge then is balancing the

sensitivity and efficiency with practical size, electronics, and cross-talk. With a list of candidate designs, bench-top measurements were performed at UM to work towards a prototype configuration. The prototype system described in Chapter 8 will demonstrate an advanced level of PSD abilities in a large scale system that can quickly quantify small amounts of plutonium mass (on the order of grams to tens of grams) with acceptable levels of uncertainty.

Chapter 8. Towards a Fast-Neutron-Multiplicity Counter Prototype

Advancements in nuclear safeguards equipment should consider non-traditional neutron detectors to replace and potentially improve capabilities of current safeguards systems. A fast-neutron multiplicity counter (FNMC) that utilizes neutron elastic scattering for fast-neutron detection has been developed at the UM using the MCNPX-PoliMi simulation code. The use of detectors based on fast neutron scattering allows for accurate neutron timing and energy information. These additional capabilities can prove useful in addition to neutron-multiplicity information. A prototype detector system was built and underwent preliminary proof-of-concept tests using well-characterized plutonium samples and ^{252}Cf sources. Simulation results and initial benchmark-measurement results are compared in detail to demonstrate the potential of an FNMC made of liquid scintillators in the determination of plutonium mass. Preliminary measurement results also help characterize the accuracy of using FNMC neutron doubles and triples to characterize plutonium mass.

Two sets of measurements were performed with the FNMC prototype: ^{252}Cf tests at the UM DNNG laboratory and plutonium tests at the JRC Ispra laboratory. Section 8.1 describes the final prototype, subsequent sections review the results from the two mentioned measurement campaigns, and the Chapter will wrap-up with a conclusion on the potential of FNMCs with organic scintillators and suggestions for a more stable and accurate prototype design.

8.1. FNMC Prototype

Detectors available at the UM DNNG laboratory include sixteen 7.62 cm ø by 7.62 cm EJ-309 liquid scintillators. As discussed in Ch. 7, these detectors are ideal for simultaneous detection of fast neutrons and photons (excellent PSD) and are good candidates for an FNMC prototype. Figure 8-1 shows the two rings of eight detectors that were chosen to test a full FNMC. An aluminum structure was designed to hold the sixteen detectors using minimal structure material to minimize unwanted neutron

scattering. Aluminum was chosen as it is reasonably transparent to neutrons. The two detector rings were placed as close together as feasible, in order to maximize system efficiency by minimizing neutron loss. The detector structure was designed for an FNMC that has a sample cavity 40 cm in diameter. There is some flexibility in the structure, allowing 34 cm to 44 cm cavities, and 34 cm was used to boost efficiency once more. Two time-synchronized CAEN V1720, 12-bit, 250-MHz, and 8-channel digitizers were used to acquire individual pulse waveforms for each of the sixteen detectors (Fig. 8-2). The detectors were gain matched with the ^{137}Cs Compton edge at 0.3 V (corresponding to 478 keVee) and the detection threshold was placed at 0.0439 V for all detectors, shown in Fig. 8-3. These settings provided a dynamic range of 0.07 – 3.12 MeVee (approximately 0.65 – 6.6 MeV neutron energy deposited). Bare measurements and measurements with 1 cm of lead were performed. Bare measurements are possible with the FNMC, although the addition of lead greatly decreases the severity of photon misclassification and therefore the final system includes 1 cm of lead. The neutron detection efficiency of the FNMC is slightly decreased with the addition of shielding. Therefore the specific application of the system can dictate what is more important between the slight change in neutron detection efficiency and photon misclassification.

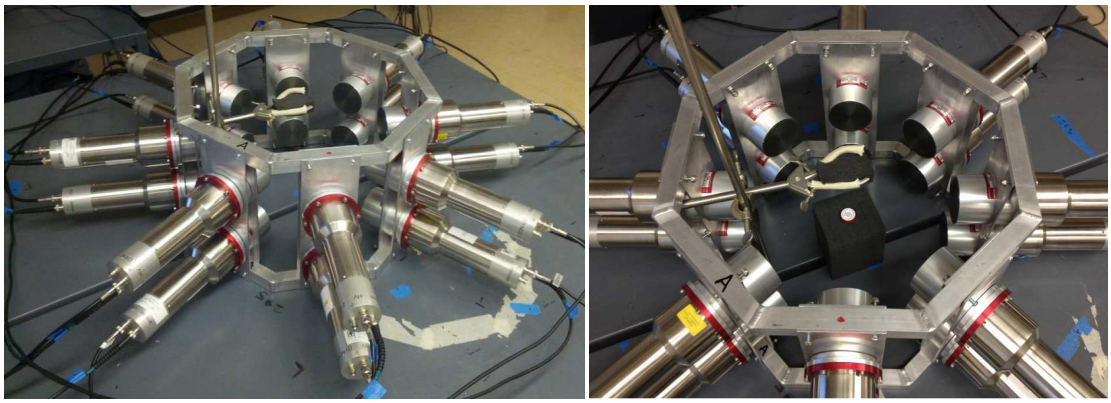

(a) (b)

Fig. 8-1. Measurements with the FNMC prototype, including two rings of eight 7.62 cm ø by 7.62 cm EJ-309 liquid scintillators, a) a bare ^{252}Cf fission source, and b) a bare ^{137}Cs photon source in the UM laboratory.

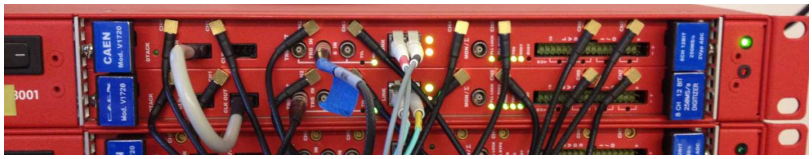

Fig. 8-2. Two CAEN V1720 12-bit, 250 MHz, 8-channel time-synchronized digitizers are connected to a Linux workstation via two optical links.

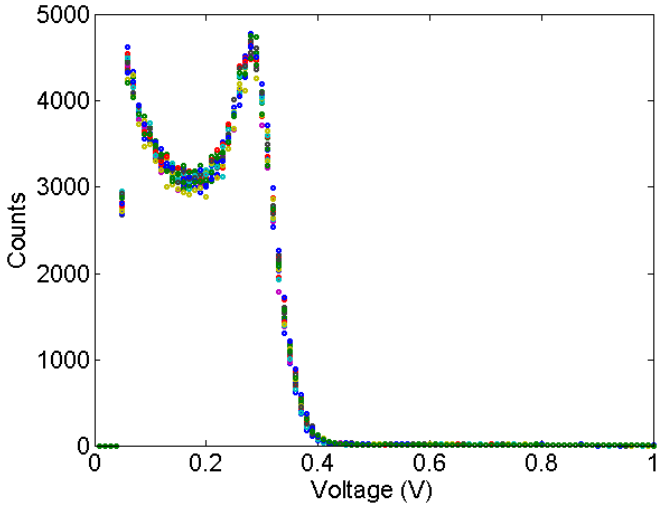

Fig. 8-3. Compton edge matching at 0.3 V for 100,000 photon pulses from all sixteen EJ-309 detectors with 0.0439 V (70 keVee) thresholds.

8.2. Initial ^{252}Cf Measurement and Simulation Benchmark Tests

Two ^{252}Cf sources were measured at UM for initial testing of the FNMC prototype as well as the first step of simulation validation. The two sources have activities of 4.7 (^{252}Cf #1) and 50.2 (^{252}Cf #2) µCi, respectively, resulting in approximately an order of magnitude difference in neutron output (20,000 versus 216,000 neutrons per second), which proved convenient for testing the system at different count rates. To further push the acquisition system and measurement analysis algorithms, a 95 µCi ^{137}Cs source was added to the 4.7 µCi ^{252}Cf source, testing the data-throughput limits of the data-acquisition system and studying the effect of a higher photon-to-neutron detection ratio on the data analysis. Lastly, a long background measurement was performed to assess the effect of the neutron background on multiplicity. All measurements were performed bare and a 70-keVee threshold was applied in the data processing. The measured neutron multiplicity for the mentioned measurement cases are show in Fig. 8-4. Measurement scenarios including the two ^{252}Cf sources were simulated for comparison.

The logarithmic scale used in Fig. 8-4 shows the vast range between the various measurements and each order of multiplicity. The multiplicity results for the two ^{252}Cf sources are an order of magnitude different as expected based on their source strengths.

Discussions follow on the effect of the background and the effect of the PSD performance on the measurements of ^{137}Cs alone and in combination with ^{252}Cf.

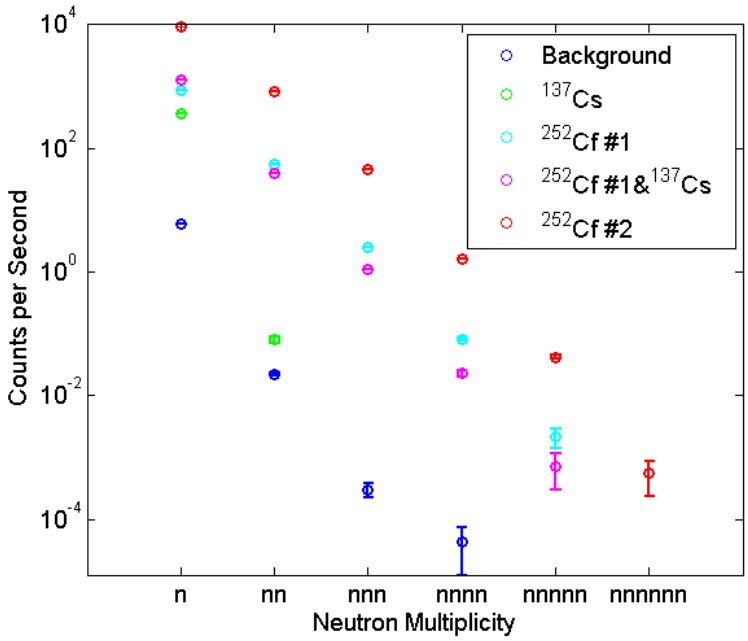

Fig. 8-4. Measured neutron multiplicity for measurements of ^{252}Cf #1, ^{252}Cf #2, ^{252}Cf #1 and ^{137}Cs, ^{137}Cs alone, and the UM laboratory background.

8.2.1. The FNMC's Response to Background Radiation

In the UM measurement laboratory, a thirteen hour background measurement was performed to determine the abundance of neutrons in the background and their contribution to accidental events. Figure 8-5a shows the total photon and neutron PHDs from all sixteen liquid scintillators. The photon PHD has two visible Compton edges from ^{40}K (1.24 MeVee edge from the 1.46 MeV photons) and ^{228}Th (2.38 MeVee edge from the 2.61 MeV photons). The total photon background rate was 1440 counts per second (90 counts per second per detector) and the total neutron background rate was 6 counts per second (only approximately 20 counts per minute per detector). Figure 8-5b shows the neutron multiplicity results from the measurement data. In this environment the neutron background was very small and does not have a significant effect on the neutron multiplicity. The background neutron doubles are only 0.7% of the doubles measured from the ^{252}Cf #1 source and 0.06% of the doubles measured from the ^{252}Cf #2 source.

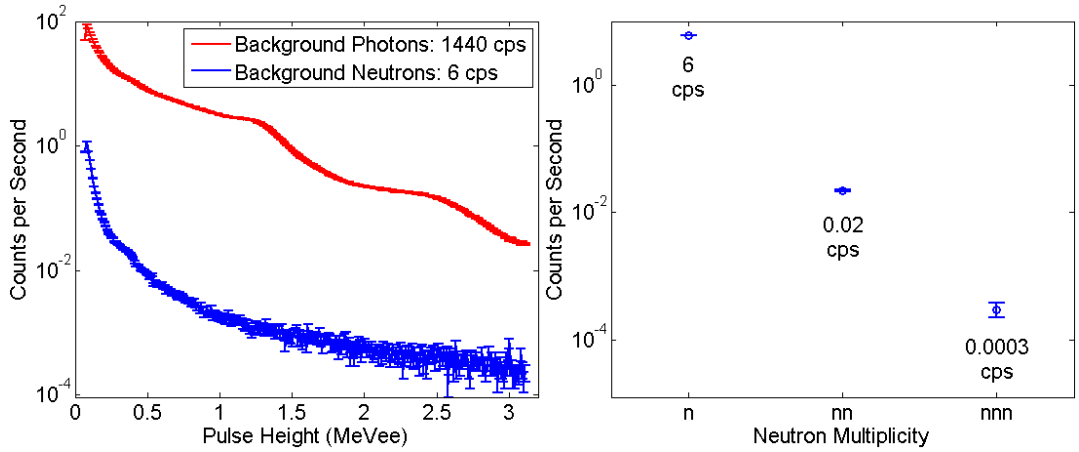

Fig. 8-5. a) Photon and neutron PHDs for all 16 liquid scintillators and b) neutron-multiplicity results from a 13-hour background measurement.

8.2.2. FNMC PSD Performance

To test the PSD capabilities of the system two measurements were performed: a 95 μCi ^{137}Cs source was measured alone and in combination with the 4.7 μCi ^{252}Cf source. The addition of the ^{137}Cs to the ^{252}Cf source increased the photon-to-neutron detection ratio from approximately 5 to 120. The change this addition brings to the neutron PHD and the neutron multiplicity reflects the effect of photon misclassification due to PSD. The most basic situation where photons are misclassified as neutrons is in the low-pulse-height area where the PSD distributions overlap. Figure 8-6 shows this effect where the low-pulse-height region of the PHD (less than approximately 0.3 MeVee) shows the largest difference between the two measurement scenarios.

The second situation where photon misclassification is common is in the cleaning of pulse pileup. The method of pulse-pileup cleaning employed on this data was described in Sect. 4.2 and uses a set fraction of the first pulse maximum to eliminate subsequent pulses that exceed that fraction of the pulse maximum. The scenario where photon/neutron misclassification is involved is when two separate photon pulses arrive within a single data-acquisition window and make it through the cleaning algorithm. In this case, the waveform is commonly classified as a neutron because the second small pulse increases the tail integral that is used in the digital PSD algorithm [18]. Figure 8-6 shows evidence of this effect seen in the neutron PHD where the ^{137}Cs Compton edge is visible. The pulse-pileup events result in a common Compton continuum, as it is the

single first detected pulse that is assessed for pulse height. This undetected pulse-pileup effect artificially increases the neutron count rate.

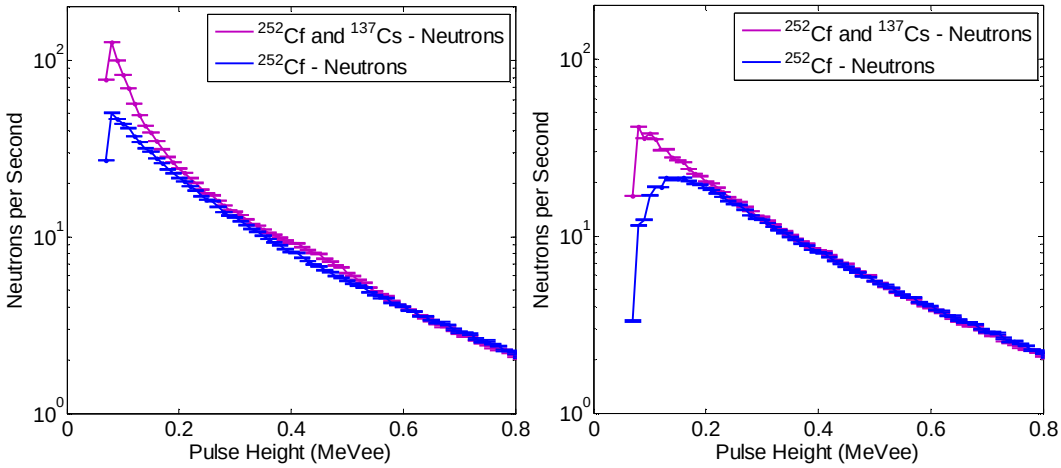

Fig. 8-6. The neutron PHDs for the measurements of ^{252}Cf and the combination of ^{252}Cf and ^{137}Cs when (a) doubles pulses at 10% of the pulse maximum and (b) 5% of the pulse maximum are cleaned.

The two scenarios discussed primarily affect the neutron singles rate because these photons are not correlated to the ^{252}Cf fission events. For a directly misclassified single photon to affect a neutron double, triple, or quadruple, it would need to arrive within the same 100 ns neutron multiplicity window as a detected single neutron, double neutron, etc. For a photon pileup event from ^{137}Cs to affect multiple neutron results, two photons would need to be detected in the same detector within approximately 10 ns of each other and still be within the 100 ns neutron-multiplicity window of a neutron detection. For these reasons, it is clear why Fig. 8-4 shows an increase in only the neutron singles with the addition of the ^{137}Cs source to the ^{252}Cf. When measuring true SNM, this effect would apply to photons from the background and radioactive decay, but not to photons from fission or (α, n) events as they are correlated in time.

The second effect of pulse pileup on neutron-multiplicity results in a decrease of neutron singles, doubles, and triples rates. When the high photon rate leads to pileup pulses that are correctly identified, one of the contributing pulses may be a neutron, and it is therefore removed from the data analysis. For the neutron singles, the previously described effects dominate and the neutron singles rate shown in Fig. 8-4 increases. For

the remaining multiples, this second pileup effect dominates, which is evidenced in Fig. 8-4 where the addition of the ^{137}Cs source leads to decreased doubles, triples, and so on.

Figure 8-7 compares the measured neutron PHD with and without the ^{137}Cs, showing the fractional increase in the PHD due to the addition of the photon source. Figures 8-6 and 8-7 show the comparison of two double pulse cleaning fractions: 10% and 5%. With 10% cleaning, the ^{137}Cs Compton edge is clearly present in the neutron PHD. When the severity of the cleaning is increased (a 5% cleaning fraction is used), the Compton edge is practically eliminated but many neutrons producing small pulses are also eliminated because the noise in their tail appears as a double pulse. When decreasing the pulse-pileup cleaning fraction from 10% to 5%, the amount of cleaned pulse-pileup waveforms increases from 0.1% to 5% of the data. There is no ideal level of pulse-pileup cleaning; it is a matter of determining whether neutron events can be sacrificed to ensure minimal photon misclassification. Many of these low pulse height waveforms that are wrongly eliminated are potential contributors to neutron doubles and triples events, therefore overly aggressive cleaning is not a solution in this application.

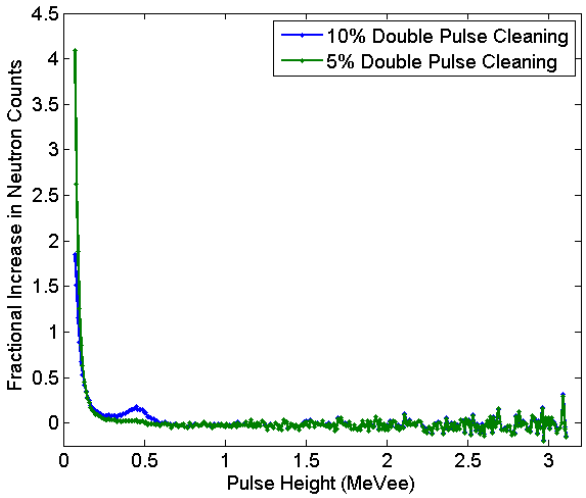

Fig. 8-7. The fractional increase in the neutron PHD when a ^{137}Cs source is added to a ^{252}Cf measurement at two different intensities of pulse-pileup cleaning.

The measurement of the ^{137}Cs photon source alone can be analyzed with the PSD-discrimination line determined for the ^{252}Cf data. PSD-classified neutrons from the photon only source were used to estimate the photon misclassification frequency. The neutron counts include true neutrons from background radiation which were subtracted based on the background measurement described previously. In 1000 photon events,

approximately two were classified as neutrons when a 10% pulse-pileup fraction was used; when a 5% pulse-pileup fraction was used, only approximately one photon was classified as a neutron. It is important to note that this value is only an approximation, especially considering photon misclassification is energy dependent and a mono-energetic photon source was used. Photons from ^{137}Cs are monoenergetic at 662 keV energy and therefore this misclassification rate obtained with ^{137}Cs is conservative. In fact when measuring plutonium samples, the photon emission has a broader and higher energy range, as seen in Fig. 4-15.

The effect on multiplicity of this strong photon source alone can be seen in Fig. 8-4 which shows that misclassification of the photon source primarily effects the singles rates. This is expected as the probability of accidental coincidence events is low for the 100 ns multiplicity window. After background subtraction, the neutron doubles rates from ^{137}Cs alone are almost negligible, as they are for triples and quadruples.

8.2.3. Simulation Validation

The measured neutron multiplicity for the two ^{252}Cf sources was compared to the simulated results. The MCNPX-PoliMi particle-transport code was used to simulate spontaneous fission events from ^{252}Cf (source option "1") and record detailed particle interaction information in the sixteen liquid scintillators. The MPPost data-processing code was used to develop the MCNPX-PoliMi output into neutron multiplicity. Figure 8-8 shows the comparison of the measured and simulated neutron multiplicity for both sources. Table 8-1 summarizes the level of agreement between the measurements and simulations. The percent difference between the measurement and simulations is quite different for the two sources and such absolute comparisons strongly depend on knowledge of the source strength. The known ^{252}Cf #1 fission reaction rate is inaccurate. For the ^{252}Cf #2 source, the difference between simulated and measured multiplicity is less than 1% for singles, -3% for doubles, and -15% for triples. This result is considered a very good agreement and is expected for the well-characterized ^{252}Cf #2 source. Measurement times were approximately 1.5 hours, long enough to obtain negligible statistical uncertainty on all orders of multiplicity.

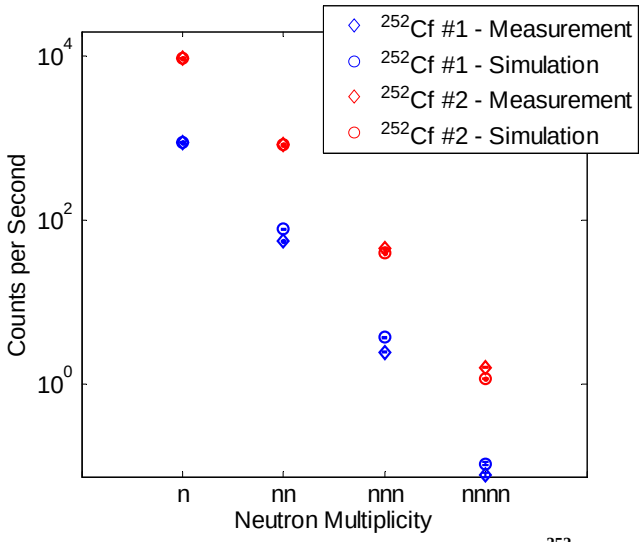

Fig. 8-8. Measured and simulated neutron multiplicities for two ^{252}Cf sources; statistical uncertainty error bars are included but appear smaller than the symbols that are used.

Table 8-1. ^{252}Cf multiplicity simulation validation for two sources.

	^{252}Cf #1 Agreement (%)	^{252}Cf #2 Agreement (%)
n	1.00	0.75
nn	37.03	-2.96
nnn	49.00	-12.38
nnnn	33.96	-27.95

8.2.4. Bare FNMC ^{252}Cf Neutron Multiplicity Detection Efficiency

The absolute fission detection efficiency values for singles, doubles, and triples, ε_m for multiple m, are calculated using Eqn. 8-1. The total neutron detection efficiency, ε_{tot}, calculated using Eqn. 8-2.

$$\boldsymbol{\varepsilon_m = \frac{number\ of\ detections\ of\ \ m\ neutrons}{number\ of\ spontaneous\ fission\ events}} \tag{8-1}$$

$$\boldsymbol{\varepsilon_{tot} = \frac{number\ of\ detected\ neutrons}{number\ of\ emitted\ neutrons}} \tag{8-2}$$

Figure 8-9 shows the measured and simulated neutron singles, doubles, and triples detection efficiencies for 252Cf measured with the two separate sources. Table 8-2 includes the tabulated 252Cf efficiency values for the two measured and simulated cases. Due to the lack of significant dead time in the FNMC prototype, each detected event (single neutron detection or double neutron detection for example) represents a single fission event from the source, fission events are not expected to overlap (overlap would

occur when detection rates surpassed two million counts per second). All events that are not cleaned from the data (approximately 95% of the data collected) are considered "real," and "accidentals" do not need to be subtracted from the data. Each detected event can be directly used towards determining the plutonium mass: unfolding of moments is not a necessary step.

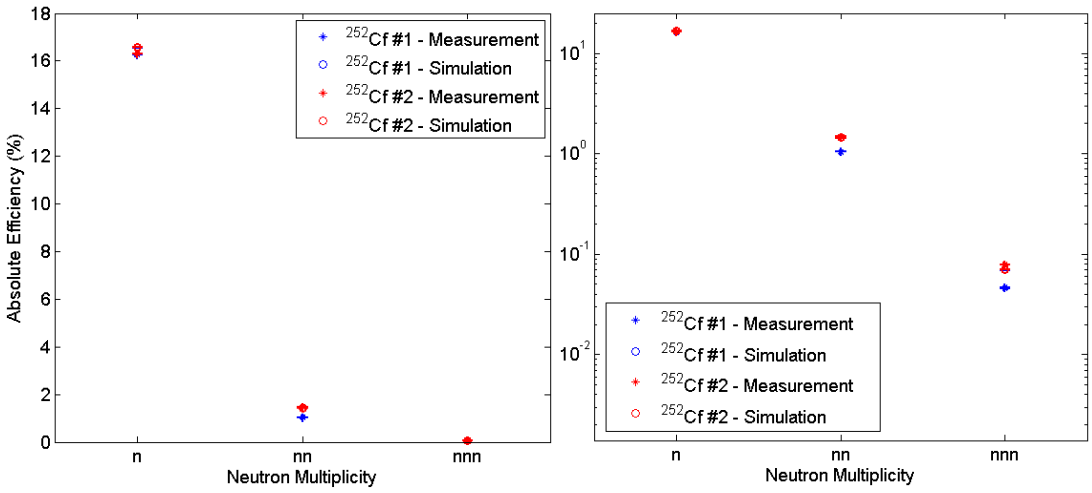

Fig. 8-9. (a) Linear and (b) logarithmic plots of the absolute detection efficiency for neutron singles, doubles, triples, and quadruples from ^{252}Cf, measured and simulated for two sources.

Table 8-2. Measured and simulated ^{252}Cf fission detection efficiency for neutron singles, doubles, and triples from two independent ^{252}Cf sources.

	^{252}Cf #1 Measured Efficiency (%)	^{252}Cf #1 Simulated Efficiency (%)	^{252}Cf #2 Measured Efficiency (%)	^{252}Cf #2 Simulated Efficiency (%)
ε_{tot}	5	5	5	5
ε_1	16	17	16	17
ε_2	1	1	1	1
ε_3	0.05	0.07	0.08	0.07

8.3. Characterizing Plutonium-Containing Materials with the FNMC Prototype

The ^{252}Cf tests helped to characterize the abilities and limitations of the FNMC prototype with a well-known fission source. To fully assess the system it was necessary to measure true plutonium samples as they have a number of differences from ^{252}Cf which can complicate the data analysis. As described previously in this work, the JRC in Ispra has a number of well-characterized plutonium samples for measurement. Figure 8-10 shows photographs of the experimental setup, which is identical to the system used at

the UM laboratory described earlier in the Chapter: sixteen detectors were placed around a 34 cm cavity. Due to the high photon emission from plutonium materials, 1 cm of lead shielding was used to improve PSD abilities.

Fig 8-10. The sixteen-detector FNMC setup at the JRC facility in Ispra.

Table 8-3. The aged material composition of seven plutonium samples investigated at the JRC.

Sample: Isotope	PuO_2-1 (g)	PuO_2-2 (g)	PuO_2-3 (g)	PuO_2-4 (g)	PM-1 (g)	PM-2 (g)	MOX-1 (g)	MOX-2 (g)
$^{240}Pu_{eff}$	***0.42***	***1.00***	***1.56***	***2.30***	***0.84***	***1.63***	***53.22***	***60.46***
^{234}U	--	--	--	--	--	--	0.05	0.06
^{235}U	--	--	--	--	--	--	4.79	5.50
^{236}U	--	--	--	--	--	--	0.05	0.06
^{238}U	--	--	--	--	--	--	670.50	769.48
^{238}Pu	0.001	0.004	0.046	0.064	0.001	0.005	0.23	0.27
^{239}Pu	6.184	5.638	4.885	4.140	17.941	17.246	111.81	127.01
^{240}Pu	0.417	0.948	1.216	1.679	0.837	1.598	46.99	53.38
^{241}Pu	0.004	0.018	0.096	0.099	0.006	0.018	1.59	1.81
^{242}Pu	0.003	0.024	0.138	0.278	0.003	0.009	3.38	3.84
^{241}Am	0.018	0.064	0.343	0.369	0.048	0.180	5.20	5.91
O	0.091	0.092	0.092	0.091	--	--	166.22	184.00
Total	6.716	6.787	6.816	6.719	18.836	19.056	1010.82	1151.32

Benchmark measurements of plutonium samples with the prototype system can confirm the proposed data analysis capabilities and validate the simulation methodology. Three types of materials were measured: PuO_2, plutonium metal (PM), and MOX. Five PuO_2 measurements were performed with $^{240}Pu_{eff}$ masses between 0.42 and 4.29 g. Two PM samples were measured with $^{240}Pu_{eff}$ masses of 0.84 and 1.63. Two masses of MOX with 53.22 and 60.46 g of $^{240}Pu_{eff}$ were measured. Details of the measurement samples are included in Table 8-3. These samples were simulated as well as fictitious samples covering a range of $^{240}Pu_{eff}$ mass from the measured values up to 70 g to assess the

evolution of the neutron singles, doubles, and triples rates across a larger range of mass. Summaries of the neutron emission are shown in Fig. 8-11.

There are several challenges associated with measuring plutonium that are not existent with ^{252}Cf. For example, a higher photon-to-neutron detection ratio is expected for any plutonium sample, plutonium isotopes have much lower fission nu-bar values, and PuO_2 and MOX emit (α, n) neutrons. With a strong ^{137}Cs source added to a small ^{252}Cf source, a photon-to-neutron detection ratio of 120 was achieved with a bare measurement. This ratio is much larger for all measured plutonium sources. One cm of lead shielding was added to the FNMC to improve the manageability of the photon flux by decreasing the ratios for MOX, PuO_2, and PM to approximately 25, 35, and 80 photon-to-neutron detections. ^{252}Cf has a very high nu-bar (an average of 3.757 neutrons per fission [8]) increasing the probability of doubles and triples events, while all plutonium isotopes emit just over 2 neutrons per spontaneous fission (2.16 for ^{240}Pu and 2.15 for ^{242}Pu) [8], making doubles and triples detection less probable. Lastly, the addition of the (α, n) neutron source component complicates the neutron signature by decreasing the value of the neutron singles and adding cross talk to neutron doubles.

Equation 8-3 defines the $^{240}Pu_{eff}$ mass relative to the even plutonium isotopes mass, for the FNMC with 1 cm of lead shielding. The coefficients are similar to those defined for ^{3}He systems that use moderation and detect thermal neutrons (Eqn. 7-1). The coefficients for the FNMC system were determined by simulating individual built-in sources (^{238}Pu, ^{240}Pu, and ^{242}Pu) in MCNPX-PoliMi and comparing the detected doubles rates to those simulated for ^{240}Pu. Including the 1 cm lead shield in these simulations had an effect on the coefficients, showing the dependence of neutron doubles on shielding configurations. This is important to consider as adjustments are made to the multiplicity counter.

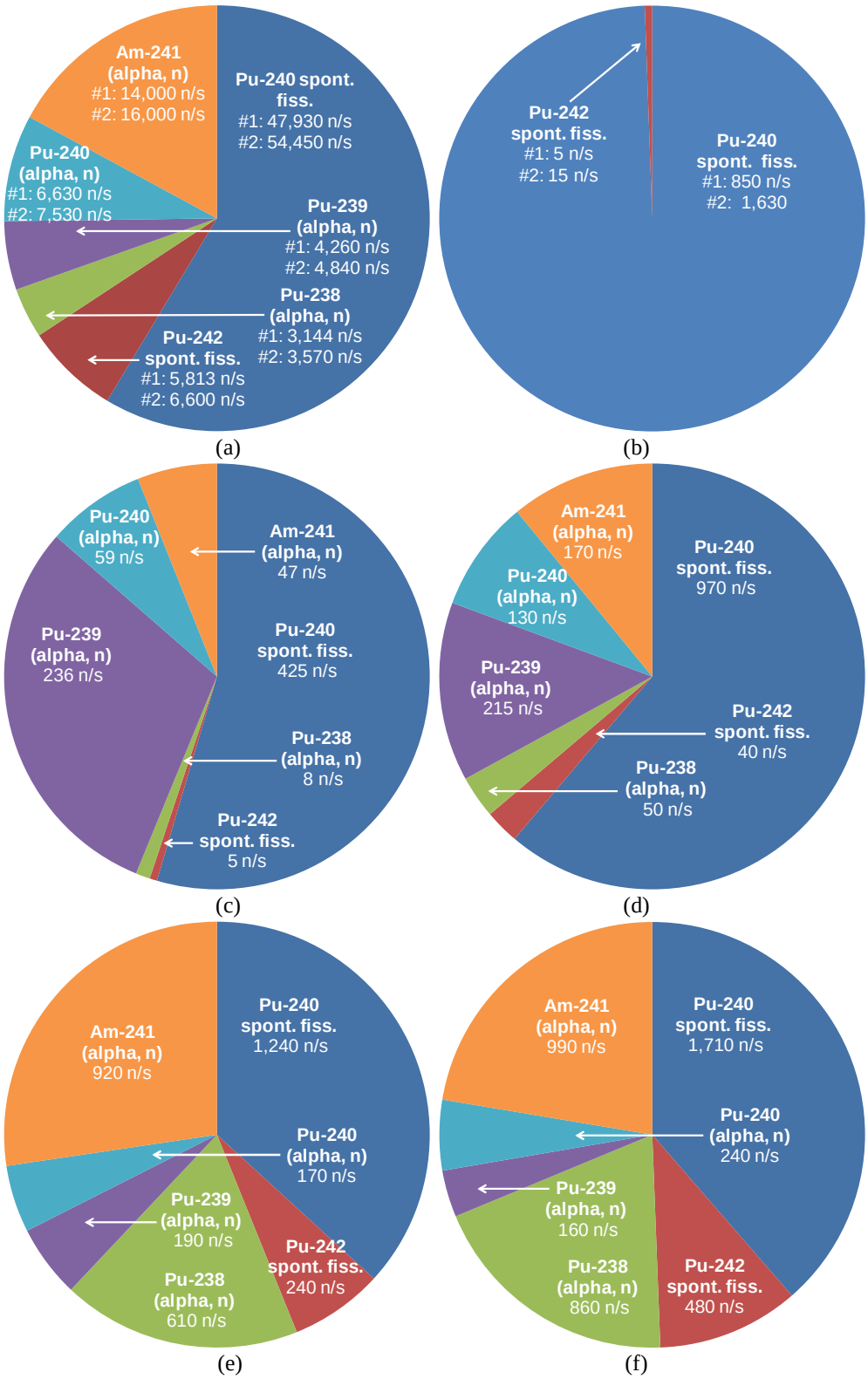

Fig. 8-11. The origin of neutron emission for a) the two MOX samples of identical isotopic composition, b) the two PM samples of similar isotopic composition, c) the PuO_2 #1, d) the PuO_2 #2, e) the PuO_2 #3, and f) the PuO_2 #4.

$$^{240}Pu_{eff} = (2.51)\ ^{238}Pu + \ ^{240}Pu + (1.67)\ ^{242}Pu \qquad (8\text{-}3)$$

8.3.1. Simulated Neutron Multiplicity

To study the effect of $^{240}Pu_{eff}$ mass on neutron singles, doubles, and triples rates, one PM sample (PM #2) and one PuO_2 (PuO_2 #4) sample were simulated with varying mass ranging from the true sample mass to 70 g. Figure 8-12 shows the simulated trends of singles, doubles, and triples rates with $^{240}Pu_{eff}$ mass for PM and PuO_2. The figures also include the same response for simulations where the material matrix of the PM and PuO_2 was voided, to show the effect of matrix attenuation and multiplication. The simulations correspond to a six hour measurements, where negligible statistical uncertainty is seen for higher-order multiples, such as triples.

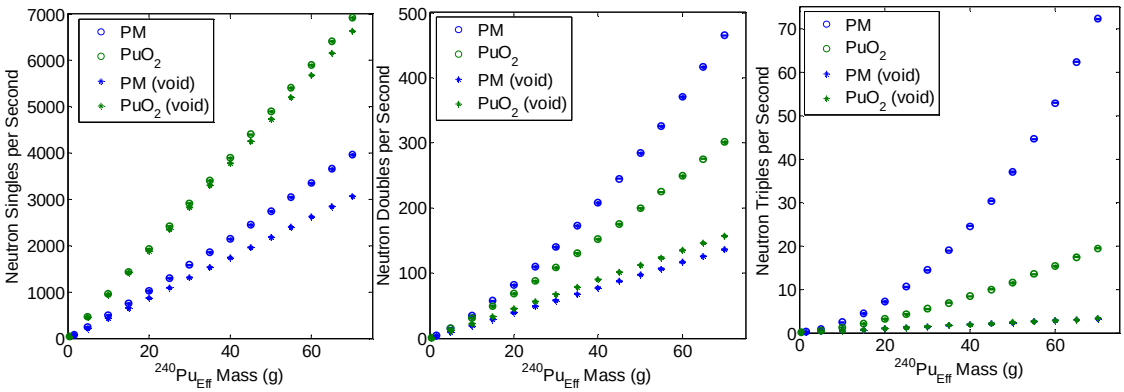

Fig. 8-12. Simulated singles, doubles, and triples for fictitious PM and PuO_2 samples of increasing $^{240}Pu_{eff}$ mass and consistent isotopic composition, based on JRC standards. Simulated results are also included for models with voided material matrices to study the effect of matrix attenuation and multiplication.

The singles trends for both materials studied are linear, but increase at different rates. The $^{240}Pu_{eff}$ relationship is based on doubles and does not account for single neutron sources. Therefore, a PuO_2 sample with the same $^{240}Pu_{eff}$ as a PM sample is expected to have a larger singles rate due to the single neutron sources from (α, n) reactions on oxygen. The singles rates for the PuO_2 with and without the material matrix are nearly identical while the effect of induced fission is seen in the PM. The neutron doubles are expected to be more similar than the singles between the two plutonium-containing materials before effects of the material matrix come into play, because their

primary source difference is in the (α, n) neutrons that emit only one neutron. For the voided cases, the spontaneous fission neutron emission is similar for both cases and thus the doubles trends are also expected to be similar. In fact, a difference is seen between the two sample types due to more cross-talk events from the (α, n) component of the PuO_2 leading to the slightly higher voided doubles values than the PM. The effect of cross talk on doubles rates is dependent on the frequency of single neutron emission, which is elevated for the PuO_2 samples with the addition of (α, n) neutrons. When the material matrix is taken into account, the increasing multiplication of the PM becomes apparent, while the PuO_2 experiences the same increase on a smaller scale. At smaller masses, where the present studies were focused, the trend of both materials is linear and similar in slope.

Triples rates can be used to study the multiplication of the sample. The triples immediately begin to have a non-linear trend for the PM samples and much larger rates than those of the PuO_2 samples which have lower material multiplication. The linear trend of the voided simulations confirms that the quadratic shape for triples versus $^{240}Pu_{eff}$ mass is due to multiplication. In the small samples that were studied here, matrix attenuation is not a dominant feature. In materials like MOX, this effect could be more prominent.

8.3.2. PSD Performance

The measurement system used at the JRC was described earlier in the chapter and was initially tested at UM with ^{252}Cf and ^{137}Cs. At the JRC measurements of the background, ^{252}Cf, and ^{137}Cs were repeated. The ^{137}Cs measurement was performed to compare to the photon misclassification rate that was discussed earlier in this Chapter. A pulse-pileup-cleaning level of 8% of the pulse height (between the 10% and 5% previously discussed) was used and the photon misclassification rate was between 2-3 misclassifications out of 1000 photon events.

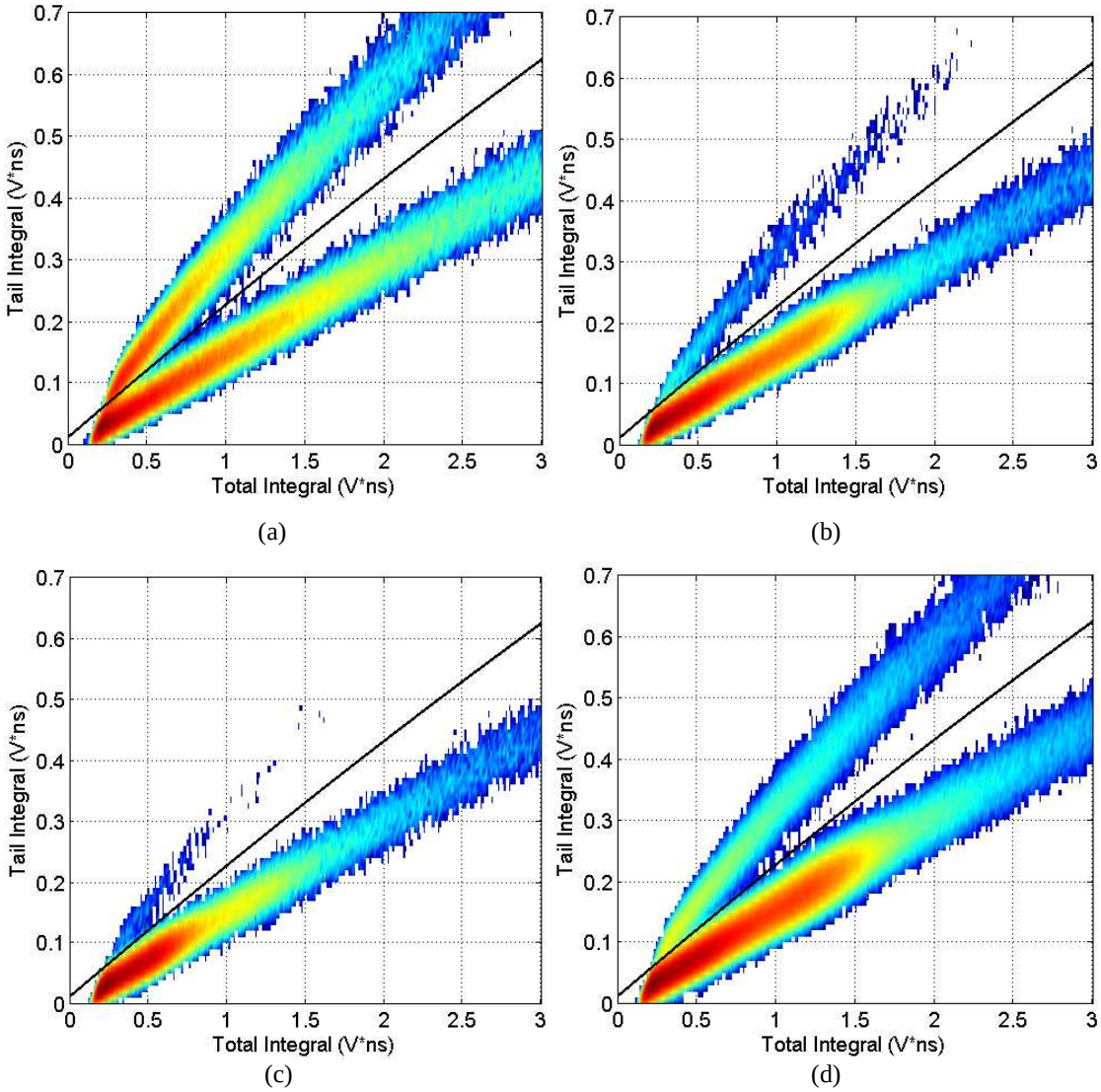

Fig. 8-13. Shows the optimized PSD discrimination line for 200,000 waveforms from the four measured material types with 1 cm of lead shielding: a) ^{252}Cf, b) PuO_2, c) PM, and d) MOX.

PSD tail versus total integral distributions for 200,000 waveforms from ^{252}Cf, PuO_2, PM, and MOX are shown in Fig. 8-13. At a 70-keVee threshold (approximately 650-keV energy deposition in the liquid scintillator), good separation is seen. Lower thresholds can be used with relatively good separation; a conservative value was used here although efficiency can be increased by decreasing the threshold. The relative photon-to-neutron detection ratio for each sample type can be seen by comparing the PSD figures. The PM measurement suffers the most from high photon-to-neutron detection ratios.

Tail and total integral lengths were chosen to provide optimal PSD as described in Sect. 4.3. The discrimination curve was determined by manually slicing the distributions in Fig. 8-13 perpendicularly to the neutron distribution, using Gaussian fitting to determine the minimum between the two distributions, and fitting the minima to a polynomial. Examples of slices from a ^{252}Cf measurement are shown in Fig. 8-14. This method of PSD works best if a large number of pulses are taken into consideration, so that slices of the distribution can be very thin resulting in more points for the polynomial fit. With detectors assemblies that are well gain matched, one polynomial can be used for all detectors. A CAEN A1536N high-voltage supply was used and the gain settings were stable over the five day measurement campaign.

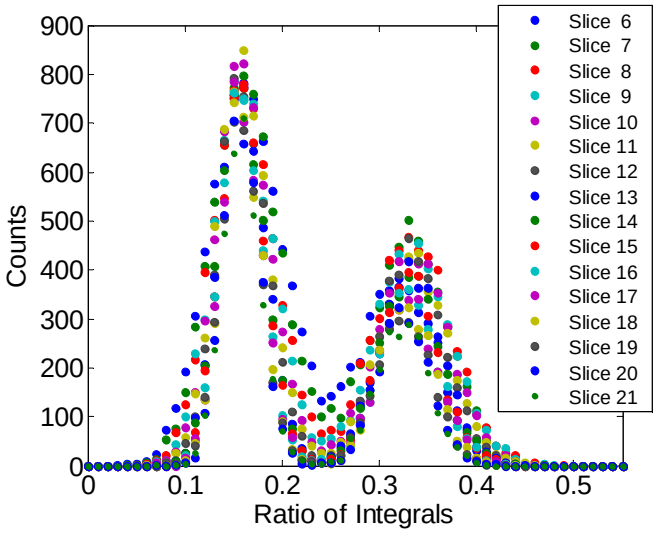

Fig. 8-14. Slices of the PSD tail versus total distributions plotted along the slice to find the minimum between the photon and neutron distributions.

8.3.3. Neutron Background Detection

Neutron detection techniques benefit from low environmental neutron background detection that can be misinterpreted as signal. Neutron multiplicity counters benefit to an even further extent considering neutron doubles, triples, etc. suffer less and less from neutron background as true neutron multiples are not expected. Some chance of truly coincident neutron multiples occur when high-energy neutrons cause spallation in high-Z materials. This effect is expected to be small unless large amounts of high-Z materials are present. Fig. 8-15 shows the measured neutron multiplicity for a 2.5 day background

measurement at the JRC laboratory. For the entire FNMC prototype, only 0.03 neutron doubles events and 0.0001 neutron triples per second were measured.

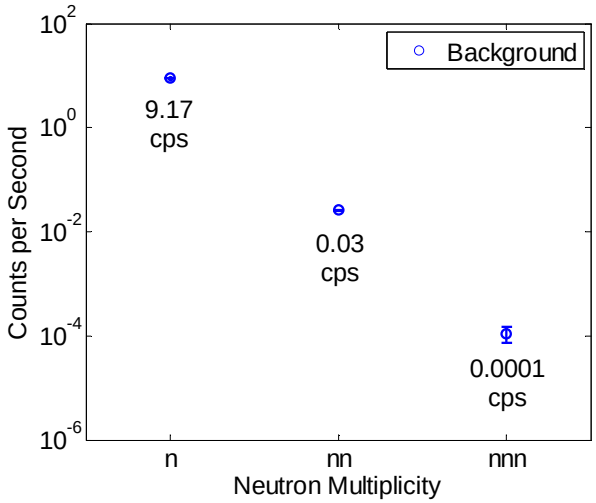

Fig. 8-15. Neutron multiplicity measured from a 2.5 day background measurement, values on the plot represent the singles, doubles, and triples rates from background alone.

The weakest measured PuO_2 sample (PuO_2 #1) can be studied with and without a neutron background subtraction. Even with the small neutron emission from PuO_2 #1, the neutron background is still small enough to have a negligible effect on doubles and triples rates: it comprises 17% of singles, 3% of doubles, and 0.4% of triples. These background rates are slightly higher than the values measured at UM, which is expected due to the increase in neutron sources at the facility. The JRC laboratory is an active nuclear laboratory with many neutron sources in use throughout the vicinity, producing a relatively high neutron background that compares well with a nuclear facility that requires safeguarding.

8.3.4. Measured Neutron Multiplicity and Simulation Validation

For the nine measurement scenarios, singles, doubles, and triples rate are compared versus $^{240}Pu_{eff}$ mass. Simulation results of these experiments are included in the comparison for validation and understanding of the measured results. Figure 8-16 show the doubles rates as a function of $^{240}Pu_{eff}$ mass and is the focus of this research. Figure 8-16 shows also the singles and triples rates.

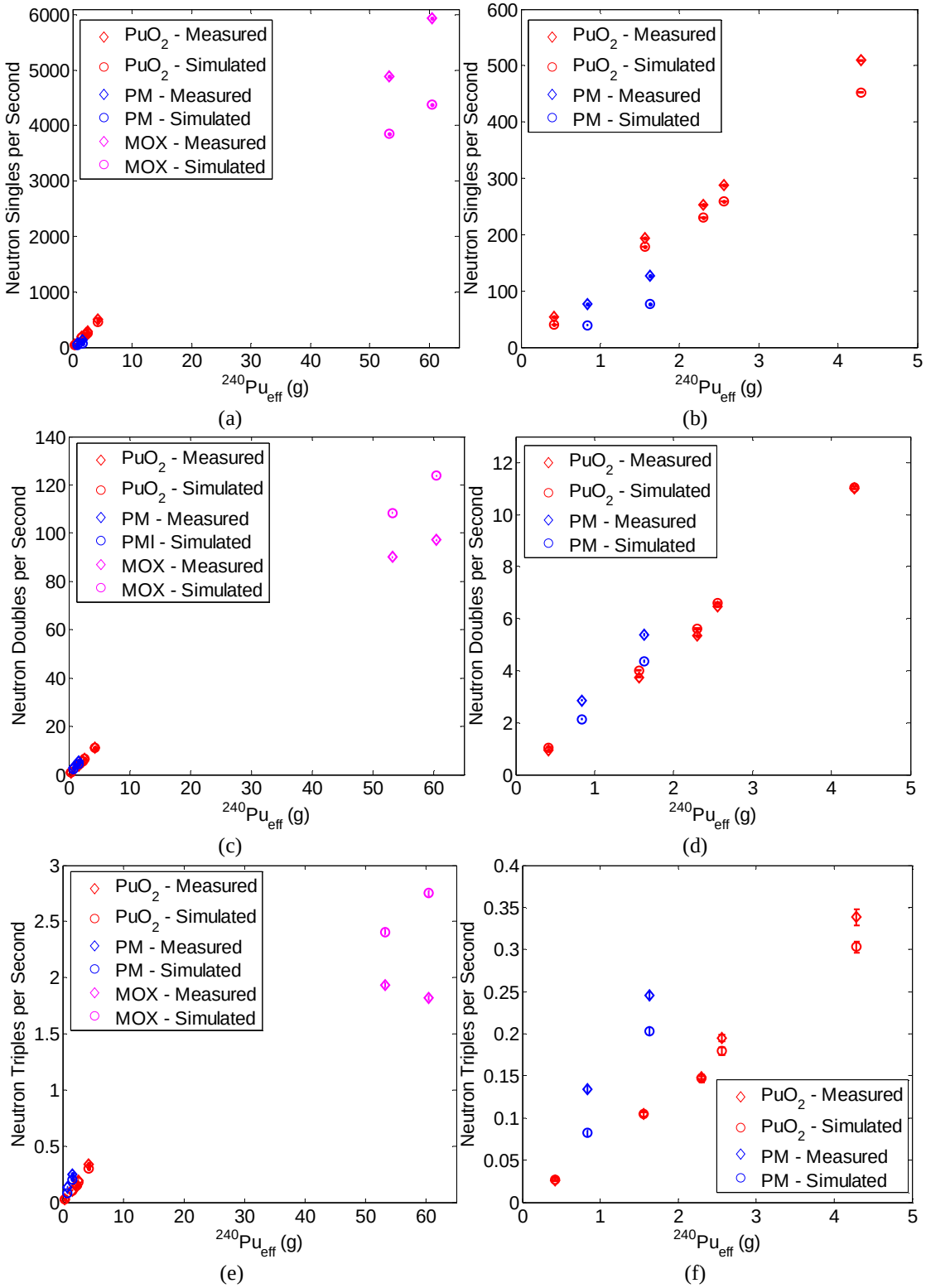

Fig. 8-16. Neutron singles (a and b), doubles (c and d), and triples (e and f) rates as a function of $^{240}Pu_{eff}$ mass measured with the FNMC with 1 cm of lead shielding for three material types: PuO_2, PM, and MOX. Two viewpoints are shown for each curve in order to focus in on the small PuO_2 and PM samples.

The simulation multiplicity values were compared to the measured values for the nine plutonium measurements. The percent difference is then valuable to study to understand the ability of the simulation tools to accurately reproduce multiplicity results for SNM measured with a FNMC. Table 8-4 summarizes the percent differences seen between simulation and measurement results for singles, doubles, triples, and quadruples. As seen previously in this work the MOX measured at the JRC has questions as to its density and configuration within its stainless steel container; it is not a surprise that the disagreement is quite large, around 30% for many of the values compared. The density of the MOX sample will affect the neutron singles and doubles quite differently. Neutrons from (α, n) reactions with oxygen are a big contributor to neutrons singles events. The density of the sample will dictate the emission of (α, n) neutrons, leading to low neutron emission if the sample is either too dense (the alpha particle was stopped before finding oxygen) or not dense enough (the alpha particle escaped the sample before being stopped). Specific activity values [8] used to quantify the number of (α, n) neutrons created in the simulated samples are only for a specific PuO_2 density and may not be accurate for the MOX powder sample that is measured.

Table 8-4. The percent difference between simulated and measured neutron multiplicity for the nine plutonium measurement configurations and ^{252}Cf.

	n (%)	nn (%)	nnn (%)	nnnn (%)
PM #1	-49	-25	-39	-40
PM #2	-40	-19	-17	-27
PuO_2 #1	-26	13	3	-40
PuO_2 #3	-8	7	0	-35
PuO_2 #4	-9	5	-1	6
PuO_2 #2,3	-10	2	-8	-9
PuO_2 #1,2,3	-11	0	-10	-4
MOX #1	-21	20	24	15
MOX #2	-26	27	51	34

The PM samples (PM #1 and #2) also had poor absolute comparisons between simulation and measurement. One contribution to the disagreement is the high photon-to-neutron detection ratio (over twice the ratio PuO_2 and three times the ratio of the MOX), leading to more severe misclassification. Taking into account the percentage error expected for misclassification based on the PM's photon-to-neutron detection ratios (approximately 20 %), the remaining difference is similar to the worst cases for PuO_2 and

MOX. Next, the knowledge of sample placement within the container was not clearly known and therefore the placement within the cavity was far from exact and may not be replicated properly in simulations. However, simulation tests of small placement variations found this to be a small effect.

The measured doubles data points can be fit by both linear and quadratic relationships for doubles rate versus $^{240}Pu_{eff}$. Both fits are shown in Fig. 8-17. From the simulations in Fig. 8-12, it is known that at such low mass values (less than 5g of $^{240}Pu_{eff}$) the trend will appear linear, but as masses continue to increase, the quadratic trend is apparent as previously discussed. Large enough masses to determine this quadratic trend were not available for measurement and therefore in order to avoid extrapolation, a linear fit is used. The linear and quadratic trend lines, where the doubles rate *D* is a function of $^{240}Pu_{eff}$ mass in grams, are defined in Eqn. 8-4 and 8-5. The composition of MOX is quite different than the PuO_2 samples due to the significant uranium content; as a result matrix attenuation is more common. Such samples will require their own calibration curve. To truly calibrate an FNMC system a wider range of PuO_2, PM, and MOX would be necessary.

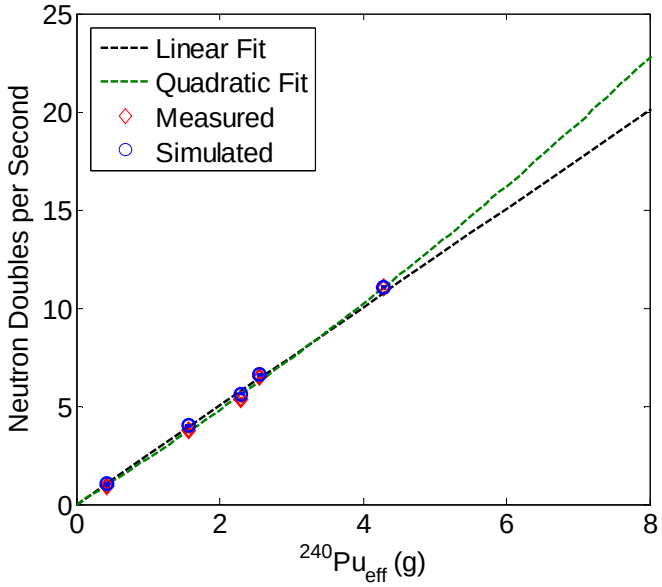

Fig. 8-17. Linear and quadratic fits to the PuO_2 doubles rate versus $^{240}Pu_{eff}$ mass data with R^2 values of 0.9945 and 0.998 respectively.

$$D\ [counts\ per\ second] = 2.51\ \times\ ^{240}Pu_{eff}[g] \quad (8\text{-}4)$$

$$D\ [counts\ per\ second] = 0.07\ \times\ ^{240}Pu_{eff}[g]^2 +\ 2.26 \times\ ^{240}Pu_{eff}[g] \quad (8\text{-}5)$$

The driving force for the choice of organic scintillators in a safeguards measurement system is the fast response of the detectors, leading to practically non-existent accidentals counts, resulting in the ability to get good statistical uncertainty in small measurement times. Using the linear fit for doubles rates, the statistical uncertainty for doubles counts can be translated directly into $^{240}Pu_{eff}$ mass. Figure 8-18 demonstrates the measurement times that would be needed to achieve set levels of statistical uncertainty (5% and 10%) for $^{240}Pu_{eff}$ mass. For these small masses, 10% statistical uncertainty can be achieved in less than one minute. Achieving 5% statistical uncertainty only takes a couple of minutes. When safeguarding SNM, the key is to look for the diversion of "significant quantities" of material. These amounts are defined as: 8 kg of plutonium, 25 kg of uranium-235 in highly enriched uranium, 75 kg of uranium-235 in natural or low enriched uranium [35]. Therefore, when measuring large plutonium samples, it is necessary to have very small $^{240}Pu_{eff}$ mass uncertainty on the result to ensure a significant quantity has not been removed. Considering that the time needed to measure at a set level of uncertainty decreases rapidly with the increase in mass (Fig. 8-18), materials high in mass can be measured with excellent statistics in a very short time.

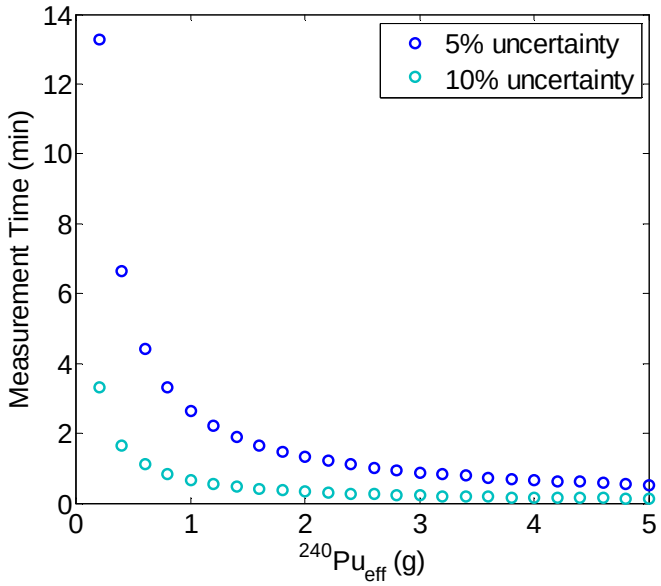

Fig. 8-18. The measurement time necessary to achieve 5% and 10% uncertainty on $^{240}Pu_{eff}$ mass determination with the FNMC prototype.

There is a straight-forward method to estimate the systematic error for the mass characterization technique developed from this set of data. Four of the five PuO_2 data points can be used to develop the $^{240}Pu_{eff}$ mass quantification curve and the fifth point can be used as a test to get an idea of systematic error. Figure 8-19 shows the four points used for the linear fit, which results in a slightly steeper slope of 2.52 neutron doubles per gram of $^{240}Pu_{eff}$ mass, and the fifth measured point. The measured neutron doubles rate from the PuO_2 #3 sample predicts a $^{240}Pu_{eff}$ mass of 1.49 ± 0.01 g. The true mass value is 1.56 g, leading to a systematic error of 4.71%.

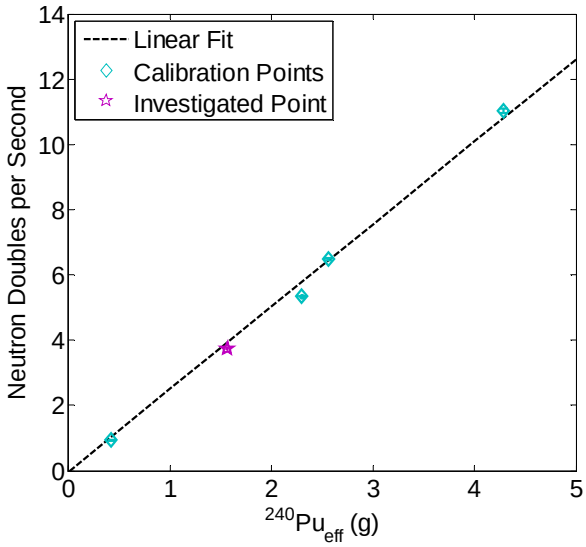

Fig. 8-19. Linear fit to four of five PuO_2 doubles rates versus $^{240}Pu_{eff}$ mass data points and the fifth point that is used for systematic uncertainty analysis.

The best way to compare a traditional multiplicity counter to the FNMC prototype is to compare the uncertainty in $^{240}Pu_{eff}$ mass determination for a set measurement time. For a solid comparison, both systems would need to measure a similar sample. A comparable ^{3}He multiplicity counter would be the high-level neutron coincidence (HLNC) counter. The HLNC contains eighteen moderated ^{3}He detectors and advertises 17.8% efficiency [36]. For oxide samples of the order of grams, the HLNC counter is expected to quantify $^{240}Pu_{eff}$ mass with 0.5% statistical uncertainty in approximately 2 hours and 45 minutes [37]. Similarly, MOX powder samples on the order kilograms reaches 0.3% statistical uncertainty in approximately fifteen minutes. When studied for the same measurement times as the HLNC, The FNMC $^{240}Pu_{eff}$ mass uncertainties were

0.4% and 0.3% for gram-level PuO_2 and kilogram-level MOX samples respectively. The two systems use different detection mechanisms, shielding mediums, data analysis methods, and detector configurations, but perform identically with respect to statistical uncertainty on plutonium mass quantification.

The samples measured at the JRC with the FNMC were also measured with the JRC Drum Monitor. This Drum Monitor system is not as comparable to the FNMC as the HLNC considering it has 148 ^{3}He tubes and a large cavity designed to fit waste drums. With a large number of ^{3}He tubes and significant polyethylene shielding, the system has high detection efficiency. For the PuO_2 #4 sample, the JRC Drum Monitor system achieved 0.52% statistical uncertainty on the plutonium mass characterization performed in 1 hour and 40 minutes. Similarly, using the FNMC measurement, the $^{240}Pu_{eff}$ mass was predicted with 0.56% statistical uncertainty in the same measurement time.

8.3.5. FNMC Detection Efficiencies

Detection efficiency is a valuable parameter to study in order to optimize and improve an FNMC measurement system. It is not however very useful to directly compare FNMC and ^{3}He system efficiencies, as they use their detections in different ways to achieve the end result: an estimate of the $^{240}Pu_{eff}$ mass. For this reason, the approach used in Sect. 8.3.4 above was preferred. Figure 8-20 shows the absolute fission detection efficiency using ^{252}Cf for the FNMC with 1 cm of lead shielding. Table 8.7 summarizes the measured and simulated values.

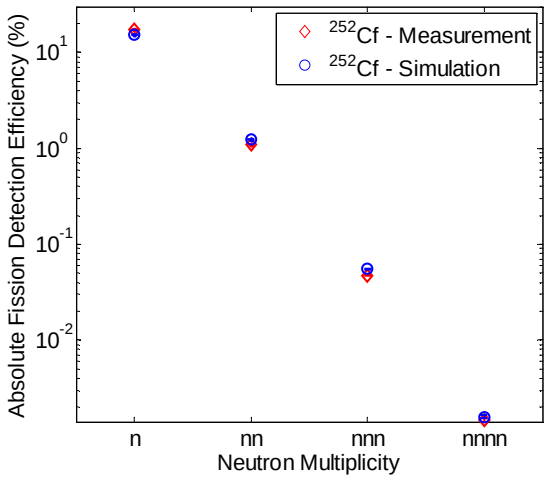

Fig. 8-20. The probability of a single, double, triple, or quadruple detection event per ^{252}Cf fission event.

Table 8-7. The absolute total neutron detection efficiency and the absolute fission detection efficiency for singles, double, triples, and quadruples.

^{252}Cf	ε_{tot}	ε_1	ε_2	ε_3	ε_4
Measured Efficiency (%)	5.28 ± 0.06	17.48 ± 0.33	1.10 ± 0.01	0.047 ± 0.001	0.002 ± 0.000
Simulated Efficiency (%)	4.81 ± 0.05	15.44 ± 0.28	1.23 ± 0.01	0.055 ± 0.001	0.002 ± 0.000

Increasing the efficiency of the system leads to smaller measurement times required for a set level of plutonium mass characterization uncertainty. There are numerous ways that the FNMC could be altered to increase the detection efficiency. The HLNC has a 17 cm diameter cavity, half the diameter of the FNMC, the FNMC detectors can easily move in to rapidly increase the efficiency. Adding a neutron scattering material between the detectors will scatter some neutrons back into the detectors that were on the path to escape the system. Simulations were performed placing polyethylene sheets in the empty space between detectors and the ^{252}Cf neutron doubles rates increased approximately 20%. The measurement threshold can be lowered, down to 40 to 50 keVee at this point in time, while still maintaining suitable PSD for most samples. The general shape of the neutron PHDs can be described by exponentially decreasing curves, therefore a lower threshold greatly increases neutron events and consequently efficiency. The above suggestions could be easily implemented into the current FNMC prototype.

8.3.6. Characterization with PHDs

The measurements showed that different types of plutonium-containing materials require different FNMC calibration curves to use both neutron doubles or triples to characterize $^{240}Pu_{eff}$ mass. In Sect. 4.5.1 it was shown that PHDs could be used to characterize material types. In the FNMC, PHDs with good statistics can be collected in a short measurement time by combining all detector signals. Figure 8-21 shows the measured neutron PHDs normalized to their integral for plutonium-containing samples that were measured during this measurement campaign.

The shape of the PHD could be used to determine the curve chosen to quantify the $^{240}Pu_{eff}$ from both doubles and triples rates. Isotopic neutron sources such as Am-Be and other (α, n) sources could also immediately be detected, as shown in Sect. 4.5.1.

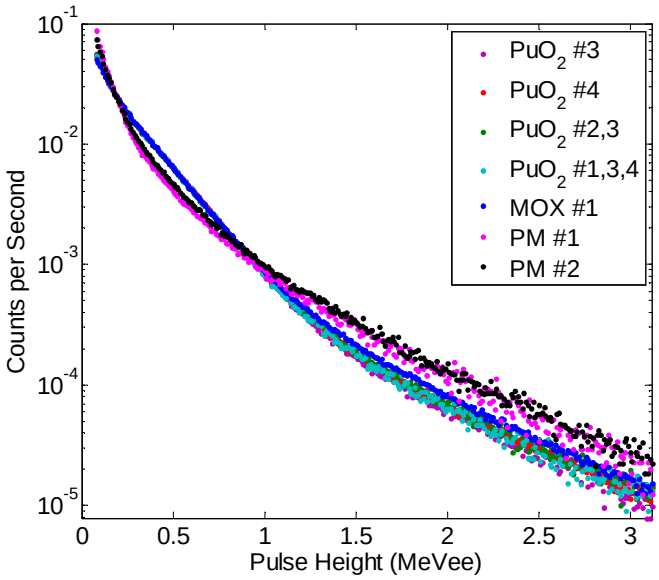

Fig. 8-21. Normalized PHDs for seven of the plutonium measurement configurations, showing oxide versus metal characterization abilities.

8.3.7. Proposed Future Work

As mentioned throughout this Chapter, there are numerous ways to improve the current prototype multiplicity system. Starting with detector system efficiency, several further modifications in the geometry and data acquisition can be made to increase the efficiency. These modifications include decreased cavity dimensions, addition of a scattering medium around detectors, decreased detection threshold, and optimization of lead shielding.

Measurements need to be performed on a broader range of plutonium containing materials to fully characterize the FNMC system. By measuring more well-defined samples the simulations can be further validated and a full calibration curve can be developed for both neutron doubles and triples.

There are data analysis techniques that could be finessed to improve the accuracy of multiplicity results. Initially, the quality of the neutron multiplicity results relies on the PSD performance, as seen with the PM measurements. Basic charge integration methods were used here to discriminate photons and neutrons, new methods can be tailored to specific pulse-height regions to improve the PSD. Also, improvements in high-quality photomultiplier tubes, digitizer sampling frequencies, and electronic noise will have an impact on the performance. Secondly, cross talk has been mentioned throughout this

work and has the potential to affect the ability of the system to quantify plutonium mass. If the neutron energy distribution among sources stays relatively constant, then the effect of cross talk across a range of masses is constant and only increases the system efficiency. However, when neutron energy distributions differ (fission neutrons versus (α, n) neutrons for example) the contribution of cross talk to doubles and triples rates will not be the same. The prevalence of cross talk is energy dependent, and the probability of detecting the same neutron in two separate detectors increases with neutron energy. Additionally, the effect of neutron cross talk on doubles depends on the frequency of neutron singles events. One way to practically eliminate this issue is to reject coincidence events from neighboring detectors, as they are most affected by of cross talk events.

Progress is being made within the DNNG to perform data analysis and mass determination algorithms on-the-fly with improvements in the size of FPGA's available in multi-channel digitizers. Multi-trigger logic, pulse-height identification, accurate timing determination, and PSD are all being implemented on-board. Recently available digitizers and digitizer crates will allow all algorithms to be stored on the digitizer and time synchronization between digitizers to be inherent. With new computer connectivity abilities, such as USB 3.0, data transfer capabilities will increase dramatically. The current prototype is limited by count rates because all waveforms are transferred to the computer and analyzed offline. When combining on-the-fly data analysis and improved connectivity, count-rate limitations will not be an issue as the measurement system will process all relevant information directly on the digitizer's board and will provide the quantities of interest.

8.3.8. Summary and Conclusions

A prototype fast-neutron-multiplicity counter was designed, constructed, and tested in two measurement campaigns. The first campaign was at UM using two ^{252}Cf sources and the second at the JRC in Ispra using two plutonium metal samples, four PuO_2 samples, and two MOX samples.

The FNMC results showed a linear trend between neutron doubles rates from PuO_2 samples and $^{240}Pu_{eff}$ mass. By using doubles rates, $^{240}Pu_{eff}$ mass could be quantified to 5% uncertainty in measurement times of the order of minutes. Plutonium metal and

PuO_2 fit on the same calibration curve for $^{240}Pu_{eff}$ masses less than 5 grams, but simulations show that the two types begin to separate shortly after that. Independent calibration curves would be needed for the two types of material and the knowledge of which curve to use can be learned from the shape of the neutron PHD.

This work proves the potential of an FNMC and provides some avenues for future work. Throughout this work, the importance of many details became apparent in the use of liquid scintillators for neutron detection. Use of a digitizer with a fast enough data-sampling frequency and vertical resolution are important to PSD. Another key aspect to the success of a system such as an FNMC is not only the data acquisition and analysis, but the choice of high quality electronics including fast and robust photo-multiplier tubes. These details, as well as numerous more, play a role in the successful implementation of an FNMC.

Chapter 9. Summary and Conclusions

The number and complexity of nuclear facilities are increasing and new technologies are needed to maintain successful international safeguards efforts. Specifically, new radiation measurement systems for nuclear safeguards are needed to provide accountability of nuclear materials in facilities around the world. Previously-developed systems relied on ^{3}He as the detection medium. These systems used neutron moderators prior to neutron detection. This thesis explores the use of fast neutron detectors in a new safeguards instrument: the FNMC. The use of fast neutron detectors such as the liquid scintillators used here provides some advantages over the previously-used ^{3}He detectors.

Organic liquid scintillators are a valuable tool for studying SNM characteristics. They are especially compatible with neutron multiplicity counting techniques for material characterization. These detectors are sensitive to neutrons at an appropriate range of energy for neutron detection within this application: neutrons from spontaneous and induced fission. The organic scintillator coupled with fast photo-multiplier tubes, electronics, and algorithms lead to excellent timing properties providing nanosecond accuracy on detection timing. Organic scintillators are sensitive to photons, but liquids offer the capability to apply PSD processing techniques on measured data to distinguish between neutrons and photons. Alternatives to ^{3}He multiplicity systems are being sought after. This work proposes an option that uses sixteen liquid scintillators and one cm of lead shielding to measure neutron doubles and triples to quantify $^{240}Pu_{eff}$ mass.

A number of experiments and simulations were performed to show the feasibility of the FNMC system. Passive neutron coincidence measurements of plutonium were performed to measure correlated neutrons from spontaneous and induced fissions. Within this study, the detection system was able to capture the time, energy, and angular distributions of neutron emission from the samples. Active-interrogation methods of uranium characterization were investigated to determine the ability of the liquid scintillators to detect induced-fission neutrons in the presence of active neutron sources. Detection timing techniques were used to identify small differences in enrichment and mass. A partial FNMC system was used to perform initial tests of the multiplicity

sensitivity of the system to changes in $^{240}Pu_{eff}$ mass. With the knowledge and tools developed in the measurements with the partial system, a full FNMC system was designed and used to quantify plutonium mass.

In parallel to measurement campaigns the physics behind neutron detection and methods for data analysis were studied using MCNPX-PoliMi simulations. The simulations helped design measurement system geometries and predicted the success of chosen data analysis techniques. After measured data were collected and analyzed the results were used to validate the simulation methodology. Throughout this work simulation validations were successful in improving the simulation tools and in the end the simulations were used to design the full FNMC measurement system.

An optimized and efficient FNMC was shown to be able to characterize materials in fast measurement times because little to no accidental counts are collected during its acquisition. Because each coincident detection is directly used, the efficiency of the system can be at a lower level and the system can still arrive at low statistical uncertainties on the $^{240}Pu_{eff}$ in fast measurement times. The measured absolute neutron detection efficiency was 5.28 ± 0.06 %. The absolute fission detection efficiency for the neutron doubles was 1.10 ± 0.01 %. The FNMC can measure gram levels of $^{240}Pu_{eff}$ to 5% statistical uncertainty in measurement times on the order of a couple of minutes. The presented FNMC could produce a system that would meet and exceed the performance of traditional ^{3}He technology, but at a fraction of the cost.

Appendix A – MCNPX-PoliMi Input Files

FNMC PuO_2 Simulation

```
c DNNG: CBNM1 (70)
c ~~~~~~~~~~~~~~~~~~~~~~~~~~~~~~~~~
c  Cells
c ~~~~~~~~~~~~~~~~~~~~~~~~~~~~~~~~~
c   EJ-309 Detectors
c ~~~~~~~~~~~~~~~~~~~~~~~~~~~~~~~~~
  101   1  -0.957    -11           imp:N,P=1   $ detector
  102   1  -0.957    -12           imp:N,P=1   $ detector
  103   1  -0.957    -13           imp:N,P=1   $ detector
  104   1  -0.957    -14           imp:N,P=1   $ detector
  105   1  -0.957    -15           imp:N,P=1   $ detector
  106   1  -0.957    -16           imp:N,P=1   $ detector
  107   1  -0.957    -17           imp:N,P=1   $ detector
  108   1  -0.957    -18           imp:N,P=1   $ detector
  109   1  -0.957    -19           imp:N,P=1   $ detector
  110   1  -0.957    -20           imp:N,P=1   $ detector
  111   1  -0.957    -21           imp:N,P=1   $ detector
  112   1  -0.957    -22           imp:N,P=1   $ detector
  113   1  -0.957    -23           imp:N,P=1   $ detector
  114   1  -0.957    -24           imp:N,P=1   $ detector
  115   1  -0.957    -25           imp:N,P=1   $ detector
  116   1  -0.957    -26           imp:N,P=1   $ detector
c ~~~~~~~~~~~~~~~~~~~~~~~~~~~~~~~~~
c   Table
c ~~~~~~~~~~~~~~~~~~~~~~~~~~~~~~~~~
  201   5  -2.7      -31           imp:n,p=1   $ Surface
  206   5  -2.7      -32           imp:n,p=1   $ Support
  207   5  -2.7      -33           imp:n,p=1   $ Support
  208   5  -2.7      -34           imp:n,p=1   $ Support
  209   5  -2.7      -35           imp:n,p=1   $ Support
  215   5  -2.7      -36           imp:n,p=1   $ Leg
  216   5  -2.7      -37           imp:n,p=1   $ Leg
  218   5  -2.7      -38           imp:n,p=1   $ Leg
  219   5  -2.7      -39           imp:n,p=1   $ Leg
  220   5  -2.7      -40           imp:n,p=1   $ Leg
  221   5  -2.7      -41           imp:n,p=1   $ Leg
c ~~~~~~~~~~~~~~~~~~~~~~~~~~~~~~~~~
c   Detector Structure
c ~~~~~~~~~~~~~~~~~~~~~~~~~~~~~~~~~
  300   5  -2.7      -90 11 19     imp:N,P=1   $front plate
  301   5  -2.7      -91 11 19     imp:N,P=1   $back plate
  302   5  -2.7      -92 12 20     imp:N,P=1   $front plate
  303   5  -2.7      -93 12 20     imp:N,P=1   $back plate
  304   5  -2.7      -94 13 21     imp:N,P=1   $front plate
  305   5  -2.7      -95 13 21     imp:N,P=1   $back plate
  306   5  -2.7      -96 14 22     imp:N,P=1   $front plate
  307   5  -2.7      -97 14 22     imp:N,P=1   $back plate
  308   5  -2.7      -98 15 23     imp:N,P=1   $front plate
  309   5  -2.7      -99 15 23     imp:N,P=1   $back plate
  310   5  -2.7     -100 16 24     imp:N,P=1   $front plate
  311   5  -2.7     -101 16 24     imp:N,P=1   $back plate
```

```
  312   5  -2.7     -102 17 25     imp:N,P=1   $front plate
  313   5  -2.7     -103 17 25     imp:N,P=1   $back plate
  314   5  -2.7     -104 18 26     imp:N,P=1   $front plate
  315   5  -2.7     -105 18 26     imp:N,P=1   $back plate
  316   5  -2.7 -106:-108:-110:-112:
                -114:-116:-118:-120 imp:N,P=1  $bottom bar
  317   5  -2.7 -107:-109:-111:-113:
                -115:-117:-119:-121 imp:N,P=1  $top bar
c ~~~~~~~~~~~~~~~~~~~~~~~~~~~~~~~~~
c   Lead Shielding
c ~~~~~~~~~~~~~~~~~~~~~~~~~~~~~~~~~
  501   3 -11.34     -51 52 -53 54 imp:N,P=1   $lead shield
c ~~~~~~~~~~~~~~~~~~~~~~~~~~~~~~~~~
c Ground
c ~~~~~~~~~~~~~~~~~~~~~~~~~~~~~~~~~
  601   6  -2.3      -500 -61      imp:N,P=1   $concrete floor
c ~~~~~~~~~~~~~~~~~~~~~~~~~~~~~~~~~
c   PuO2 Source
c ~~~~~~~~~~~~~~~~~~~~~~~~~~~~~~~~~
  701   7  -10.94    -71            imp:n,p=1  $PuO2 Sample
  702   8  -7.92     -72            imp:n,p=1  $Source stand
  703   8  -7.92     -73 74         imp:n,p=1  $Source stand
  704   8  -7.92     -75            imp:n,p=1  $Source stand
c ~~~~~~~~~~~~~~~~~~~~~~~~~~~~~~~~~
c  Environment
c ~~~~~~~~~~~~~~~~~~~~~~~~~~~~~~~~~
  901   2  -1.205E-3 -500 61 11 12 13 14 15 16 17 18 19 20
             21 22 23 24 25 26 31 32 33 34 35 36 37 38
             39 40 41 90 91 92 93 94 95 96 97 98 99 100
             101 102 103 104 105 71 72 75
              #703 #316 #317 #501 imp:N,P=1
  999   0     500                  imp:N,P=0

c ~~~~~~~~~~~~~~~~~~~~~~~~~~~~~~~~~
c  Surfaces
c ~~~~~~~~~~~~~~~~~~~~~~~~~~~~~~~~~
c   EJ-309 Detectors
c ~~~~~~~~~~~~~~~~~~~~~~~~~~~~~~~~~
  11   RCC    16.92         0   5.31    7.6200         0  0    3.8100
  12 1 RCC    16.92         0   5.31    7.6200         0  0    3.8100
  13 2 RCC    16.92         0   5.31    7.6200         0  0    3.8100
  14 3 RCC    16.92         0   5.31    7.6200         0  0    3.8100
  15 4 RCC    16.92         0   5.31    7.6200         0  0    3.8100
  16 5 RCC    16.92         0   5.31    7.6200         0  0    3.8100
  17 6 RCC    16.92         0   5.31    7.6200         0  0    3.8100
  18 7 RCC    16.92         0   5.31    7.6200         0  0    3.8100
  19   RCC    16.92         0  -5.31    7.6200         0  0    3.8100
  20 1 RCC    16.92         0  -5.31    7.6200         0  0    3.8100
  21 2 RCC    16.92         0  -5.31    7.6200         0  0    3.8100
  22 3 RCC    16.92         0  -5.31    7.6200         0  0    3.8100
  23 4 RCC    16.92         0  -5.31    7.6200         0  0    3.8100
  24 5 RCC    16.92         0  -5.31    7.6200         0  0    3.8100
  25 6 RCC    16.92         0  -5.31    7.6200         0  0    3.8100
  26 7 RCC    16.92         0  -5.31    7.6200         0  0    3.8100
c ~~~~~~~~~~~~~~~~~~~~~~~~~~~~~~~~~
c   Table
c ~~~~~~~~~~~~~~~~~~~~~~~~~~~~~~~~~
```

```
  31 8 BOX  -50  -100   -0.5   100   0 0    0 200   0   0 0   0.5
  32 8 BOX  -50  -100   -4.9     4.4 0 0    0 200   0   0 0   4.4
  33 8 BOX  45.6 -100   -4.9     4.4 0 0    0 200   0   0 0   4.4
  34 8 BOX -45.6 -100   -4.9    91.2 0 0    0   4.4 0   0 0   4.4
  35 8 BOX -45.6   95.6 -4.9    91.2 0 0    0   4.4 0   0 0   4.4
  36 8 BOX -50     -2.2 -4.9     4.4 0 0    0   4.4 0   0 0 -85.5
  37 8 BOX  45.6   -2.2 -4.9     4.4 0 0    0   4.4 0   0 0 -85.5
  38 8 BOX -50   -100   -4.9     4.4 0 0    0   4.4 0   0 0 -85.5
  39 8 BOX  45.6 -100   -4.9     4.4 0 0    0   4.4 0   0 0 -85.5
  40 8 BOX -50     95.6 -4.9     4.4 0 0    0   4.4 0   0 0 -85.5
  41 8 BOX  45.6   95.6 -4.9     4.4 0 0    0   4.4 0   0 0 -85.5
c ~~~~~~~~~~~~~~~~~~~~~~~~~~~~~~~~
c   Lead Shielding
c ~~~~~~~~~~~~~~~~~~~~~~~~~~~~~~~~
  51   CZ   6.5        $outer cylinder
  52   CZ   5.5        $inner cylinder
  53   PZ   15.25      $top
  54   PZ  -16.25      $bottom
c ~~~~~~~~~~~~~~~~~~~~~~~~~~~~~~~~
c Ground
c ~~~~~~~~~~~~~~~~~~~~~~~~~~~~~~~~
  61 PZ     -108   $ Floor level
c ~~~~~~~~~~~~~~~~~~~~~~~~~~~~~~~~
c CBNM
c ~~~~~~~~~~~~~~~~~~~~~~~~~~~~~~~~
  71  RCC  0 0 -0.21   0 0 0.364  0.73
  72  RCC  0 0 -0.25   0 0 0.02   4.5
  73  RCC  0 0 -16.25  0 0 16     3
  74  RCC  0 0 -16.25  0 0 16     2.8
  75  RCC  0 0 -17.25  0 0 1      8.5
c ~~~~~~~~~~~~~~~~~~~~~~~~~~~~~~~~
c  Detector Structure
c ~~~~~~~~~~~~~~~~~~~~~~~~~~~~~~~~
  90 RPP  22 22.3175   -5.05     5.05   -17.25  13.35
  91 RPP 24.2225 24.54 -5.05     5.05   -17.25  13.35
  92 1 RPP 22 22.3175  -5.05     5.05   -17.25  13.35
  93 1 RPP 24.2225 24.54 -5.05   5.05   -17.25  13.35
  94 2 RPP 22 22.3175  -5.05     5.05   -17.25  13.35
  95 2 RPP 24.2225 24.54 -5.05   5.05   -17.25  13.35
  96 3 RPP 22 22.3175  -5.05     5.05   -17.25  13.35
  97 3 RPP 24.2225 24.54 -5.05   5.05   -17.25  13.35
  98 4 RPP 22 22.3175 -5.05      5.05   -17.25  13.35
  99 4 RPP 24.2225 24.54 -5.05   5.05   -17.25  13.35
 100 5 RPP 22 22.3175 -5.05      5.05   -17.25  13.35
 101 5 RPP 24.2225 24.54 -5.05   5.05   -17.25  13.35
 102 6 RPP 22 22.3175  -5.05     5.05   -17.25  13.35
 103 6 RPP 24.2225 24.54 -5.05  5.05   -17.25  13.35
 104 7 RPP 22 22.3175 -5.05     5.05   -17.25  13.35
 105 7 RPP 24.2225 24.5 -5.05   5.05   -17.25  13.35
 106   RPP  22.3176 24.2224   -10.0333 10.0333 -17.25 -15.345
 107   RPP  22.3176 24.2224   -10.0333 10.0333  11.445 13.35
 108 1 RPP  22.3176 24.2224   -10.0333 10.0333 -17.25 -15.345
 109 1 RPP  22.3176 24.2224   -10.0333 10.0333  11.445 13.35
 110 2 RPP  22.3176 24.2224   -10.0333 10.0333 -17.25 -15.345
 111 2 RPP  22.3176 24.2224   -10.0333 10.0333  11.445 13.35
 112 3 RPP  22.3176 24.2224   -10.0333 10.0333 -17.25 -15.345
 113 3 RPP  22.3176 24.2224   -10.0333 10.0333  11.445 13.35
```

```
 114 4 RPP  22.3176 24.2224   -10.0333 10.0333 -17.25 -15.345
 115 4 RPP  22.3176 24.2224   -10.0333 10.0333  11.445 13.35
 116 5 RPP  22.3176 24.2224   -10.0333 10.0333 -17.25 -15.345
 117 5 RPP  22.3176 24.2224   -10.0333 10.0333  11.445 13.35
 118 6 RPP  22.3176 24.2224   -10.0333 10.0333 -17.25 -15.345
 119 6 RPP  22.3176 24.2224   -10.0333 10.0333  11.445 13.35
 120 7 RPP  22.3176 24.2224   -10.0333 10.0333 -17.25 -15.345
 121 7 RPP  22.3176 24.2224   -10.0333 10.0333  11.445 13.35
c ~~~~~~~~~~~~~~~~~~~~~~~~~~~~~~~~~
c  Environment
c ~~~~~~~~~~~~~~~~~~~~~~~~~~~~~~~~~
 500 RPP -500 500   -500 500   -500 500

c ~~~~~~~~~~~~~~~~~~~~~~~~~~~~~~~~~
c Data
c ~~~~~~~~~~~~~~~~~~~~~~~~~~~~~~~~~
c Translations
c ~~~~~~~~~~~~~~~~~~~~~~~~~~~~~~~~~
  TR1  0 0 0   0.7071  0.7071  0   -0.7071  0.7071  0   0  0  1
  TR2  0 0 0   0       1       0   -1       0       0   0  0  1
  TR3  0 0 0  -0.7071  0.7071  0   -0.7071 -0.7071  0   0  0  1
  TR4  0 0 0  -1       0       0    0      -1       0   0  0  1
  TR5  0 0 0  -0.7071 -0.7071  0    0.7071 -0.7071  0   0  0  1
  TR6  0 0 0   0      -1       0    1       0       0   0  0  1
  TR7  0 0 0   0.7071 -0.7071  0    0.7071  0.7071  0   0  0  1
  TR8  0 0 -17.25
c ~~~~~~~~~~~~~~~~~~~~~~~~~~~~~~~~~
c Physics
c ~~~~~~~~~~~~~~~~~~~~~~~~~~~~~~~~~
  MODE n p
  PHYS:N J 20
  PHYS:P 0 1 1
  CUT:P 2J 0
c ~~~~~~~~~~~~~~~~~~~~~~~~~~~~~~~~~
c Source
c ~~~~~~~~~~~~~~~~~~~~~~~~~~~~~~~~~
  SDEF cel=701 pos=0 0 -0.21 axs=0 0 1 rad=d1 ext=d2 erg=d3
  SC1  Source radius (inner outer)
  SI1  0 0.73
  SC2  Source height
  SI2  0 0.364
  SI3  L 3 4 38 39 40 41
  SP3  0.2230 0.0430 0.2372 0.0723 0.0666 0.3579
  IPOL  99 1 2 1 J 1 16 101 102 103 104 105 106 107 108
        109 110 111 112 113 114 115 116
  NPS 4635000 $ 9270000 = Number of reactions in 3600 sec (aged CBNM)
  FILES 21 DUMN1
  DBCN
  PRDMP 2J 1
c ~~~~~~~~~~~~~~~~~~~~~~~~~~~~~~~~~
c Materials
c ~~~~~~~~~~~~~~~~~~~~~~~~~~~~~~~~~
c  EJ-309 liquid scintillator
c (Eljen Technologies, EJ-309 Fact Sheet)
c ~~~~~~~~~~~~~~~~~~~~~~~~~~~~~~~~~
  m1   nlib=60c  plib=04p
       1001      0.548
```

```
      6000      0.452
c ~~~~~~~~~~~~~~~~~~~~~~~~~~~~~~~~
c Air, Dry (near sea level) d=-1.205E-3
c (Mat. Compendium PNNL)
c ~~~~~~~~~~~~~~~~~~~~~~~~~~~~~~~~
  m2  nlib=60c  plib=04p
      6000     -0.000124
      7014     -0.755268
      8016     -0.231781
     18000.42c -0.012827
c ~~~~~~~~~~~~~~~~~~~~~~~~~~~~~~~~
c  Lead Shielding d=-11.34
c
c ~~~~~~~~~~~~~~~~~~~~~~~~~~~~~~~~
  m3  82000.42c 1
c ~~~~~~~~~~~~~~~~~~~~~~~~~~~~~~~~
c Polyethylene d=-0.9300
c (Mat. Compendium PNNL)
c ~~~~~~~~~~~~~~~~~~~~~~~~~~~~~~~~
  m4  nlib=60c  plib=04p
      1001 -0.143716
      6000 -0.856284
c ~~~~~~~~~~~~~~~~~~~~~~~~~~~~~~~~
c Aluminum table d=-2.70
c ~~~~~~~~~~~~~~~~~~~~~~~~~~~~~~~~
  m5  nlib=60c  plib=04p
     13027     -1
c ~~~~~~~~~~~~~~~~~~~~~~~~~~~~~~~~
c Concrete (Mat. Compendium PNNL) d=-2.3
c (Mat. Compendium PNNL)
c ~~~~~~~~~~~~~~~~~~~~~~~~~~~~~~~~
  m6  nlib=60c  plib=04p
      1001     -0.022100
      6000     -0.002484
      8016     -0.574930
     11023     -0.015208
     12000     -0.001266
     13027     -0.019953
     14000     -0.304627
     19000     -0.010045
     20000     -0.042951
     26000.42c -0.006435
c ~~~~~~~~~~~~~~~~~~~~~~~~~~~~~~~~
c  PuO2 CBNM Sample d=-10.94
c (CBNM-70)
c ~~~~~~~~~~~~~~~~~~~~~~~~~~~~~~~~
  m7  94238.42c   -0.00669
      94239.60c   -0.71672
      94240.60c   -0.17839
      94241.60c   -0.01412
      94242.60c   -0.02031
      95241.61c   -0.05027
      08016.60c   -0.01350
c ~~~~~~~~~~~~~~~~~~~~~~~~~~~~~~~~
c Steel d=-7.92
c (Mat. Compendium PNNL)
c ~~~~~~~~~~~~~~~~~~~~~~~~~~~~~~~~
```

```
  m8  26000.55c -0.6950
      24000.50c -0.1900
      28000.50c -0.0950
      25055.51c  -0.0200
c ~~~~~~~~~~~~~~~~~~~~~~~~~~~~~~~~~
c  Tallies
c ~~~~~~~~~~~~~~~~~~~~~~~~~~~~~~~~~
c detectors
c ~~~~~~~~~~~~~~~~~~~~~~~~~~~~~~~~~
c  F31:n 11.3 12.3 13.3 14.3 15.3 16.3 17.3 18.3 19.3
c  E31 0 0.5 0.7 29i 1 899i 10 100
c  C31 0 1
c  F41:p 11.3
c  E41 0 999i 10
c  C41 0 1
c ~~~~~~~~~~~~~~~~~~~~~~~~~~~~~~~~~
```

Ispra PuO_2 Pellet Simulations with the Partial FNMC

```
c DNNG: Measurement 1 PuO2 pellets
c ~~~~~~~~~~~~~~~~~~~~~~~~~~~~~~~~~
c  Cells
c ~~~~~~~~~~~~~~~~~~~~~~~~~~~~~~~~~
c   EJ-309 Detectors
c ~~~~~~~~~~~~~~~~~~~~~~~~~~~~~~~~~
  101   1  -0.916    -11           imp:N,P=1   $ detector
  102   1  -0.916    -12           imp:N,P=1   $ detector
  103   1  -0.916    -13           imp:N,P=1   $ detector
  104   1  -0.916    -14           imp:N,P=1   $ detector
c ~~~~~~~~~~~~~~~~~~~~~~~~~~~~~~~~~
c Tables
c ~~~~~~~~~~~~~~~~~~~~~~~~~~~~~~~~~
  201   5  -2.7      -21  imp:N,P=1   $ Aluminum surface
  202   5  -2.7      -22  imp:N,P=1   $ Aluminum rectangular support
  203   5  -2.7      -23  imp:N,P=1   $ Aluminum rectangular support
  204   5  -2.7      -24  imp:N,P=1   $ Aluminum rectangular support
  205   5  -2.7      -25  imp:N,P=1   $ Aluminum rectangular support
  206   5  -2.7      -26  imp:N,P=1   $ Aluminum support, PMT and table
  207   5  -2.7      -27  imp:N,P=1   $ Aluminum support, PMT and table
  208   5  -2.7      -28  imp:N,P=1   $ Aluminum surface, source table
  209   5  -2.7      -29  imp:N,P=1   $ Aluminum rectangular support
  210   5  -2.7      -30  imp:N,P=1   $ Aluminum rectangular support
  211   5  -2.7      -31  imp:N,P=1   $ Aluminum rectangular support
  212   5  -2.7      -32  imp:N,P=1   $ Aluminum rectangular support
c ~~~~~~~~~~~~~~~~~~~~~~~~~~~~~~~~~
c Ground
c ~~~~~~~~~~~~~~~~~~~~~~~~~~~~~~~~~
  401   6  -2.3      -91 -41       imp:N,P=1   $ concrete floor
c ~~~~~~~~~~~~~~~~~~~~~~~~~~~~~~~~~
c   Lead Shielding
c ~~~~~~~~~~~~~~~~~~~~~~~~~~~~~~~~~
  501   3  -11.34 -51 52 53 -54 55 imp:N,P=1   $lead shield
c ~~~~~~~~~~~~~~~~~~~~~~~~~~~~~~~~~
c  PuO2 pellets and containers
c ~~~~~~~~~~~~~~~~~~~~~~~~~~~~~~~~~
  701   7  -4.27   -71             imp:N,P=1   $pellet #6
  702   7  -4.25   -72             imp:N,P=1   $pellet #7
  703   7  -4.23   -73             imp:N,P=1   $pellet #8
  704   7  -4.26   -74             imp:N,P=1   $pellet #9
  705   7  -4.26   -75             imp:N,P=1   $pellet #10
  706   7  -5.35   -76             imp:N,P=1   $pellet #20
  707   7  -5.70   -77             imp:N,P=1   $pellet #21
  708   7  -5.70   -78             imp:N,P=1   $pellet #22
  709   8  -5.24   -79             imp:N,P=1   $pellet #30
  801   9  -7.92   -81 71          imp:N,P=1   $container #6
  802   9  -7.92   -82 72          imp:N,P=1   $container #7
  803   9  -7.92   -83 73          imp:N,P=1   $container #8
  804   9  -7.92   -84 74          imp:N,P=1   $container #9
  805   9  -7.92   -85 75          imp:N,P=1   $container #10
  806   9  -7.92   -86 76          imp:N,P=1   $container #20
  807   9  -7.92   -87 77          imp:N,P=1   $container #21
  808   9  -7.92   -88 78          imp:N,P=1   $container #22
  809   9  -7.92   -89 79          imp:N,P=1   $container #30
```

```
c ~~~~~~~~~~~~~~~~~~~~~~~~~~~~~~~~
c  Environment
c ~~~~~~~~~~~~~~~~~~~~~~~~~~~~~~~~
  901   2  -1.205E-3 -91 #501  41
             11 12 13 14 21 22 23
             24 25 26 27 28 29 30
             31 32 81 82 83 84 85
             86 87 88 89           imp:N,P=1
  999   0    91                    imp:N,P=0

c ~~~~~~~~~~~~~~~~~~~~~~~~~~~~~~~~
c  Surfaces
c ~~~~~~~~~~~~~~~~~~~~~~~~~~~~~~~~
c  EJ-309 Detectors
c ~~~~~~~~~~~~~~~~~~~~~~~~~~~~~~~~
  11 1 RCC      20  0  0    7.62  0  0    3.81
  12 2 RCC      20  0  0    7.62  0  0    3.81
  13 3 RCC      20  0  0    7.62  0  0    3.81
  14 4 RCC      20  0  0    7.62  0  0    3.81
c ~~~~~~~~~~~~~~~~~~~~~~~~~~~~~~~~
c Tables
c ~~~~~~~~~~~~~~~~~~~~~~~~~~~~~~~~
  21 RPP -47.5  47.5 8.45  53.95   -17    -15.5   $ Aluminum surface on
the
  22 RPP -57    47.5 8.45  12.95   -21.5  -17.01  $ Aluminum
rectangular
  23 RPP -57    47.5 49.45  53.95   -21.5  -17.01  $ Aluminum
rectangular
  24 RPP -57   -52.5 12.96  49.44   -21.5  -17.01  $ Aluminum
rectangular
  25 RPP  43.5  47.5 12.96  49.44   -21.5  -17.01  $ Aluminum
rectangular
  26 RPP -47.5  47.5 31.2   40.2    -15.49 -11     $ Aluminum
rectangular
  27 RPP -47.5  47.5 35.7   40.2    -10.99  -2     $ Aluminum
rectangular
  28 RPP -82.5  82.5 -42.55   7.45   -21    -20.6  $ Aluminum surface
  29 RPP -82.5  82.5 -42.55 -38.05   -25.5  -21.01 $ Aluminum
  30 RPP -82.5  82.5  2.95   7.45   -25.5  -21.01  $ Aluminum
  31 RPP -82.5 -78 -38.04   2.94   -25.5  -21.01   $ Aluminum
  32 RPP  78  82.5 -38.04  2.94   -25.5  -21.01    $ Aluminum
c ~~~~~~~~~~~~~~~~~~~~~~~~~~~~~~~~
c Ground
c ~~~~~~~~~~~~~~~~~~~~~~~~~~~~~~~~
  41 PZ     -99   $ Floor level
c ~~~~~~~~~~~~~~~~~~~~~~~~~~~~~~~~
c   Lead Shielding
c ~~~~~~~~~~~~~~~~~~~~~~~~~~~~~~~~
  51 5 CZ   20
  52 5 CZ   19.75
  53   PZ  -5
  54   PZ   5
  55   PY   7
c ~~~~~~~~~~~~~~~~~~~~~~~~~~~~~~~~
c PuO2 Pellets
c ~~~~~~~~~~~~~~~~~~~~~~~~~~~~~~~~
  71   RCC   1.768 -1.768 -0.75  0 0 0.4   0.7
```

```
  72   RCC   2.5    0      -0.75  0 0 0.4   0.7
  73   RCC   1.768  1.768 -0.75  0 0 0.4   0.7
  74   RCC   0      2.5   -0.75  0 0 0.4   0.7
  75   RCC  -1.768  1.768 -0.75  0 0 0.4   0.7
  76   RCC  -2.5    0      -0.9   0 0 0.8   0.7
  77   RCC  -1.768 -1.768 -1.0   0 0 1.5   0.7
  78   RCC   0     -2.5   -1.3   0 0 3.0   0.7
  79   RCC   0      0      -1.7   0 0 3.4   0.7
  81   RCC   1.768 -1.768 -6.8   0 0 7.95  0.75
  82   RCC   2.5    0      -6.8   0 0 7.95  0.75
  83   RCC   1.768  1.768 -6.8   0 0 7.95  0.75
  84   RCC   0      2.5   -6.8   0 0 7.95  0.75
  85   RCC  -1.768  1.768 -6.8   0 0 7.95  0.75
  86   RCC  -2.5    0      -6.8   0 0 8.2   0.75
  87   RCC  -1.768 -1.768 -6.8   0 0 8.8   0.75
  88   RCC   0     -2.5   -6.8   0 0 10    0.75
  89   RCC   0      0      -6.8   0 0 10    0.75
c ~~~~~~~~~~~~~~~~~~~~~~~~~~~~~~~~~
c  Environment
c ~~~~~~~~~~~~~~~~~~~~~~~~~~~~~~~~~
  91 RPP -500 500   -500 500   -500 500

c ~~~~~~~~~~~~~~~~~~~~~~~~~~~~~~~~~
c Data
c ~~~~~~~~~~~~~~~~~~~~~~~~~~~~~~~~~
c Translations
c ~~~~~~~~~~~~~~~~~~~~~~~~~~~~~~~~~
  TR1  0 0 0   0.815 0.5790 0   -0.5790  0.815 0   0 0 1
  TR2  0 0 0   0.313 0.9499 0   -0.9499  0.313 0   0 0 1
  TR3  0 0 0  -0.313 0.9499 0   -0.9499 -0.313 0   0 0 1
  TR4  0 0 0  -0.815 0.5790 0   -0.5790 -0.815 0   0 0 1
  TR5  0  -2.0 0
c ~~~~~~~~~~~~~~~~~~~~~~~~~~~~~~~~~
c Physics
c ~~~~~~~~~~~~~~~~~~~~~~~~~~~~~~~~~
  MODE n p
  PHYS:N J 20
  PHYS:P 0 1 1
  CUT:P 2J 0
c ~~~~~~~~~~~~~~~~~~~~~~~~~~~~~~~~~
c Source
c ~~~~~~~~~~~~~~~~~~~~~~~~~~~~~~~~~
  SDEF pos=0 0 -1.7 axs=0 0 1 rad=D1 ext=D2 erg=D5 cel=D6 eff=1e-4
  SC1  Source radius (inner outer)
  SI1  0 3.2
  SC2  Source height
  SI2  0 3.4
  SI5  L 3      4      -38    -39    -40    -41
  SP5    0.3782 0.0235 0.0403 0.1418 0.1129 0.3033
  SI6  L 701   702   703   704   705   706   707   708   709
  SP6    0.024 0.024 0.024 0.024 0.024 0.060 0.120 0.240 0.460
  IPOL  99 1 2 1 J 1 4 101 102 103 104
  NPS 1.26585E7 $ 14065 rxn/sec, 1 hour meas is 50634000, use 4 seeds
  FILES 21 DUMN1
  DBCN
  PRDMP 2J 1
c ~~~~~~~~~~~~~~~~~~~~~~~~~~~~~~~~~
```

```
c Materials
c ~~~~~~~~~~~~~~~~~~~~~~~~~~~~~~~~
c  EJ-309 liquid scintillator
c (Eljen Technologies, EJ-309 Fact Sheet)
c ~~~~~~~~~~~~~~~~~~~~~~~~~~~~~~~~
  m1   nlib=60c  plib=04p
       1001      0.548
       6000      0.452
c ~~~~~~~~~~~~~~~~~~~~~~~~~~~~~~~~
c Air, Dry (near sea level) d=-1.205E-3
c (Mat. Compendium PNNL)
c ~~~~~~~~~~~~~~~~~~~~~~~~~~~~~~~~
  m2  nlib=60c  plib=04p
      6000     -0.000124
      7014     -0.755268
      8016     -0.231781
     18000.42c -0.012827
c ~~~~~~~~~~~~~~~~~~~~~~~~~~~~~~~~
c  Lead Shielding d=-11.34
c
c ~~~~~~~~~~~~~~~~~~~~~~~~~~~~~~~~
  m3  82000.42c 1
c ~~~~~~~~~~~~~~~~~~~~~~~~~~~~~~~~
c Polyethylene d=-0.9300
c (Mat. Compendium PNNL)
c ~~~~~~~~~~~~~~~~~~~~~~~~~~~~~~~~
  m4  nlib=60c  plib=04p
      1001 -0.143716
      6000 -0.856284
c ~~~~~~~~~~~~~~~~~~~~~~~~~~~~~~~~
c Aluminum table d=-2.70
c ~~~~~~~~~~~~~~~~~~~~~~~~~~~~~~~~
  m5  nlib=60c  plib=04p
     13027     -1
c ~~~~~~~~~~~~~~~~~~~~~~~~~~~~~~~~
c Concrete (Mat. Compendium PNNL) d=-2.3
c (Mat. Compendium PNNL)
c ~~~~~~~~~~~~~~~~~~~~~~~~~~~~~~~~
  m6  nlib=60c  plib=04p
      1001     -0.022100
      6000     -0.002484
      8016     -0.574930
     11023     -0.015208
     12000     -0.001266
     13027     -0.019953
     14000     -0.304627
     19000     -0.010045
     20000     -0.042951
     26000.42c -0.006435
c ~~~~~~~~~~~~~~~~~~~~~~~~~~~~~~~~
c  PuO2 pellets 6,7,8,9,10,20,21,22
c ~~~~~~~~~~~~~~~~~~~~~~~~~~~~~~~~
  m7  8016.60c    -0.1174
      94238.42c   -0.0005
      94239.60c   -0.7466
      94240.60c   -0.1151
      94241.60c   -0.0027
```

```
      94242.60c   -0.0023
      95241.61c   -0.0153
c ~~~~~~~~~~~~~~~~~~~~~~~~~~~~~~~~~
c  PuO2 pellet 30
c ~~~~~~~~~~~~~~~~~~~~~~~~~~~~~~~~~
  m8  8016.60c    -0.1164
      94238.42c   -0.0007
      94239.60c   -0.6026
      94240.60c   -0.2282
      94241.60c   -0.0057
      94242.60c   -0.0124
      95241.61c   -0.0340
c ~~~~~~~~~~~~~~~~~~~~~~~~~~~~~~~~~
c    Steel
c ~~~~~~~~~~~~~~~~~~~~~~~~~~~~~~~~~
  m9  26000.55c -0.6950
      24000.50c -0.1900
      28000.50c -0.0950
      25055.51c  -0.0200
c ~~~~~~~~~~~~~~~~~~~~~~~~~~~~~~~~~
c  Tallies
c ~~~~~~~~~~~~~~~~~~~~~~~~~~~~~~~~~
c detectors
c ~~~~~~~~~~~~~~~~~~~~~~~~~~~~~~~~~~~~
  F31:n 11.3 12.3 13.3 14.3
  E31 0 0.5 0.7 29i 1 899i 10 100
  C31 0 1
```

Ispra Mixed-Oxide Fuel Example

```
Detailed Ispra Model Setup
c
~~~~~~~~~~~~~~~~~~~~~~~~~~~~~~~~~~~~~~~~~~~~~~~~~~~~~~~~~~~~~~~~~~~~~~~~~~~~~~
c   CELLS
~~~~~~~~~~~~~~~~~~~~~~~~~~~~~~~~~~~~~~~~~~~~~~~~~~~~~~~~~~~~~~~~~~~~~~~~~~~~~~
~
c
c   MOX Source 2
c ~~~~~~~~~~~~~~~~
601     0          -73 87 -82     imp:n,p=1 $vacuum on top of powder
602     1   -0.7   -73 81 -87     imp:n,p=1 $MOX powder
603     10  -7.92   73 -74 81 -82 imp:n,p=1 $inner steel cylinder
604     10  -7.92  -74 80 -81     imp:n,p=1 $steel inner bottom
605     10  -7.92  -74 82 -83     imp:n,p=1 $steel inner top
606     0           74 -75 80 -83 imp:n,p=1 $surrounding vacuum
cylinder
607     0          -75 79 -80     imp:n,p=1 $bottom vacuum
608     0          -75 83 -84     imp:n,p=1 $top vacuum
609     0          -72 84 -85     imp:n,p=1 $another top vacuum
610     10  -7.92   75 -76 79 -84 imp:n,p=1 $outer steel cylinder
611     10  -7.92  -76 89 -79     imp:n,p=1 $steel outer bottom
612     10  -7.92   72 -77 84 -85 imp:n,p=1 $steel cylinder top
613     10  -7.92  -77 85 -86     imp:n,p=1 $steel outer top
614     0          -71 88 -89     imp:n,p=1 $vacuum inside al-support
615     0           71 -72 88 -89 imp:n,p=1 $Al cylindrical support
c
c   EJ-309 Detector 1
c ~~~~~~~~~~~~~~~~
1       2   -2.70     1 -2  -9          imp:N,P=1      $ Al endcap
3       2   -2.70     2 -32  8  -9      imp:N,P=1      $ Al external wall
4       2   -2.70     3 -5   9  -12     imp:N,P=1      $ Al wall
c 5     6   -0.001    2 -3   7  -8      imp:N,P=1      $ nitrogen chamber
6       5   -0.916    2 -32  -8         imp:N,P=1      $ detector
7       7   -2.23     32 -5  -9         imp:N,P=1      $ pyrex window
8       2   -2.70     4 -14  12 -13     imp:N,P=1      $ Al ring
9       2   -0.001    5 -31 -10         imp:N,P=1      $ PMT big
10      4   -0.001    5 -31  10 -11     imp:N,P=1      $ air around PMT
11      8   -8.747    5 -21  11 -12     imp:N,P=1      $ mu metal wall
18      2   -0.001   31 -27 -34         imp:N,P=1      $ PMT small
19      4   -0.001   31 -21  19 -11     imp:N,P=1      $ air around PMT
21      8   -8.747   15 -27  19 -20     imp:N,P=1      $ mu metal wall
22      4   -0.001   21 -27  34 -19     imp:N,P=1      $ air around PMT
13      4   -0.001   27 -17 -19         imp:N,P=1      $ air/Al in tube
14      2   -2.70    16 -27  20 -35     imp:N,P=1      $ Al wall
23      2   -2.70    27 -17  19 -35     imp:N,P=1      $ Al wall
15      2   -2.70    17 -18 -35         imp:N,P=1      $ Al endcap
16      4   -0.001   21 -15  19 -28     imp:N,P=1      $ air around PMT
17      8   -8.747   21 -15  19  28 -29 imp:N,P=1      $ mu metal wall
c
c   EJ-309 Detector 2
c ~~~~~~~~~~~~~~~~
101 like 1 but trcl=2
103 like 3 but trcl=2
104 like 4 but trcl=2
```

```
c 105  like 5 but trcl=2
106 like 6 but trcl=2
107 like 7 but trcl=2
108 like 8 but trcl=2
109 like 9 but trcl=2
110 like 10 but trcl=2
111 like 11 but trcl=2
118 like 18 but trcl=2
119 like 19 but trcl=2
121 like 21 but trcl=2
122 like 22 but trcl=2
113 like 13 but trcl=2
114 like 14 but trcl=2
123 like 23 but trcl=2
115 like 15 but trcl=2
116 like 16 but trcl=2
117 like 17 but trcl=2
c
c   EJ-309 Detector 3
c ~~~~~~~~~~~~~~~~~
301 like 1 but trcl=3
303 like 3 but trcl=3
304 like 4 but trcl=3
c 305  like 5 but trcl=3
306 like 6 but trcl=3
307 like 7 but trcl=3
308 like 8 but trcl=3
309 like 9 but trcl=3
310 like 10 but trcl=3
311 like 11 but trcl=3
318 like 18 but trcl=3
319 like 19 but trcl=3
321 like 21 but trcl=3
322 like 22 but trcl=3
313 like 13 but trcl=3
314 like 14 but trcl=3
323 like 23 but trcl=3
315 like 15 but trcl=3
316 like 16 but trcl=3
317 like 17 but trcl=3
c
c   EJ-309 Detector 4
c ~~~~~~~~~~~~~~~~~
401 like 1 but trcl=4
403 like 3 but trcl=4
404 like 4 but trcl=4
c 405  like 5 but trcl=4
406 like 6 but trcl=4
407 like 7 but trcl=4
408 like 8 but trcl=4
409 like 9 but trcl=4
410 like 10 but trcl=4
411 like 11 but trcl=4
418 like 18 but trcl=4
419 like 19 but trcl=4
421 like 21 but trcl=4
422 like 22 but trcl=4
```

```
413 like 13 but trcl=4
414 like 14 but trcl=4
423 like 23 but trcl=4
415 like 15 but trcl=4
416 like 16 but trcl=4
417 like 17 but trcl=4
c
c   Lead Bricks
c ~~~~~~~~~~~~~~~~
500  9  -11.34 (40 :-41 )-42 43 (-44 :45 )-46 47 48 -49   imp:n,p=1
501 like 500 but trcl=2
502 like 500 but trcl=3
503 like 500 but trcl=4
c
c   Table
c ~~~~~~~~~~~~~~~~
200  2  -2.7  -50  imp:n,p=1     $ Surface
201  2  -2.7  -51  imp:n,p=1     $ Surface
202  2  -2.7  -52  imp:n,p=1     $ Surface
203  2  -2.7  -53  imp:n,p=1     $ Support
204  2  -2.7  -54  imp:n,p=1     $ Support
205  2  -2.7  -55  imp:n,p=1     $ Support
206  2  -2.7  -56  imp:n,p=1     $ Support
207  2  -2.7  -57  imp:n,p=1     $ Support
208  2  -2.7  -58  imp:n,p=1     $ Support
209  2  -2.7  -59  imp:n,p=1     $ Support
210  2  -2.7  -60  imp:n,p=1     $ Support
211  2  -2.7  -61  imp:n,p=1     $ Support
213  2  -2.7  -62  imp:n,p=1     $ Support
214  2  -2.7  -63  imp:n,p=1     $ Leg
215  2  -2.7  -64  imp:n,p=1     $ Leg
216  2  -2.7  -65  imp:n,p=1     $ Leg
217  2  -2.7  -66  imp:n,p=1     $ Leg
218  2  -2.7  -67  imp:n,p=1     $ Leg
219  2  -2.7  -68  imp:n,p=1     $ Leg
220  2  -2.7  -69  imp:n,p=1     $ Leg
221  2  -2.7  -70  imp:n,p=1     $ Leg
c
c   Floor
c ~~~~~~~~~~~~~~~~
800 3 -2.35  -97 imp:n,p=1
c
c Enviroment
c ~~~~~~~~~~~~~~~~
990 4  -.001225   -99
     50 51 52 53 54 55 56 57 58 59 60 61 62   $ Table
     63 64 65 66 67 68 69 70  97    imp:n,p=1
      $ 76 -84 89 (77:-89:86)      imp:n,p=1  $ Floor
991 4 -0.001225   -98
     #1 #3 #4 #6 #7 #8 #9 #10 #11 #18 #19 #13 $ Det 1
     #14 #15 #16 #17 #21 #22 #23
     #101 #103 #104 #106 #107 #108 #109 #110  $ Det 2
     #111 #118 #119 #113 #114 #115 #116 #117
     #121 #122 #123
     #301 #303 #304 #306 #307 #308 #309 #310  $ Det 3
     #311 #318 #319 #313 #314 #315 #316 #317
     #321 #322 #323
```

```
     #401 #403 #404 #406 #407 #408 #409 #410  $ Det 4
     #411 #418 #419 #413 #414 #415 #416 #417
     #421 #422 #423 #500 #501 #502 #503
     (-89:76:84) (77:-84:86) #613   imp:n,p=1    $ Lead Bricks
999 0  99 98   imp:n,p=0

c
c~~~~~~~~~~~~~~~~~~~~~~~~~~~~~~~~~~~~~~~~~~~~~~~~~~~~~~~~~~~~~~~~~~~~~~~~~~~~~~~
c   SURFACES
c
c~~~~~~~~~~~~~~~~~~~~~~~~~~~~~~~~~~~~~~~~~~~~~~~~~~~~~~~~~~~~~~~~~~~~~~~~~~~~~~~
c
c   MOX Source Container
c ~~~~~~~~~~~~~~~~~
71    6    cz 2.1  $Support cylinder inner
72    6    cz 5.1  $Support cylinder outer and upper empty space
73    6    cz 4.14  $inner contaner cylinder inner wall
74    6    cz 4.445  $inner container cylinder outer wall
75    6    cz 5.2  $outer container cylinder inner wall
76    6    cz 5.4  $outer container cylinder outer wall
77    6    cz 6.75  $top steel cylinder
c  78    6    pz -17.5482  $top of support, bottom of container
79    6    pz -16.5482  $outer container - BOTTOM
80    6    pz -16.3482  $inner container outer surf
81    6    pz -15.8482  $inner container inner surf
82    6    pz 10.9518  $inner container inner surf
83    6    pz 11.4518  $inner container outer surf
84    6    pz 11.6518  $outer container
85    6    pz 13.6518  $outer container
86    6    pz 15.6518  $outer container
87    6    pz 10.9517  $top of PuO powder
88    6    pz -17.5
89    6    pz -17.5482   $ top
c
c   EJ-309 Detector
c ~~~~~~~~~~~~~~~~~
C      Surface cards for detector
1  1    PX   0
2  1    PX   0.16002
3  1    PX   11.8
4  1    PX   12.6
32 1    PX   12.67
5  1    PX   13.35
c 7  1    CX   5.2303
8  1    CX   6.33998
9  1    CX   6.5
10 1    CX   6.35
C      Surface cards for the PMT
11 1    CX   6.8984
12 1    CX   7
13 1    CX   8.2
14 1    PX   14.6
31 1    PX   21.95
15 1    PX   32.2
16 1    PX   34.7
27 1    PX   35.4
17 1    PX   37.63998
```

```
18 1    PX   37.8
34 1    CX   4.2
19 1    CX   4.3984
20 1    CX   4.5
35 1    CX   4.7
21 1    PX   29.3
C      Surface cards for the table
22 1    PY  -8.54238
23 1    PY  -8.29438
24 1    PX  -95.6
25 1    PZ  -38.1
26 1    PZ   38.1
33 1    PX   56.8
C      Surface cards for the conical part of the PMT
c 27 1    CX
28 1    KX   37.3  0.743162901 -1
29 1    KX   37.42 0.743162901 -1
c
c   Lead Blocks
c ~~~~~~~~~~~~~~~~~
40 5 P -55.125 0 56.25 275.625
41 5 P -55.125 0 -56.25 0
42 5 PX 0
43 5 PX -5
44 5 P 27.5625 -28.125 0 175.594
45 5 P 27.5625 28.125 0 -316.41
46 5 P -55.125 0 56.25 1403.438
47 5 p -55.125 0 -56.25 -1127.81
48 5 P 27.5625 -28.125 0 -454.22
49 5 P 27.5625 28.125 0 316.406
c
c   Table
c ~~~~~~~~~~~~~~~~~
50 BOX -100 -50 -0.5    50 0 0    0 100 0   0 0 0.5     $ Surface
51 BOX -50 -100 -0.5    100 0 0   0 200 0   0 0 0.5     $ Surface
52 BOX  50 -50  -0.5    50 0 0    0 100 0   0 0 0.5     $ Surface
53 BOX -100 -50 -4.9    50 0 0    0 4.4 0   0 0 4.4     $ Support
54 BOX -100 -45.6 -4.9  4.4 0 0   0 91.2 0  0 0 4.4     $ Support
55 BOX -100 45.6 -4.9   50 0 0    0 4.4 0   0 0 4.4     $ Support
56 BOX -50 -100 -4.9    4.4 0 0   0 200 0   0 0 4.4     $ Support
57 BOX 45.6 -100 -4.9   4.4 0 0   0 200 0   0 0 4.4     $ Support
58 BOX -45.6 -100 -4.9  91.2 0 0  0 4.4 0   0 0 4.4     $ Support
59 BOX -45.6 95.6 -4.9  91.2 0 0  0 4.4 0   0 0 4.4     $ Support
60 BOX 50 -50 -4.9      50 0 0    0 4.4 0   0 0 4.4     $ Support
61 BOX 50 45.6 -4.9     50 0 0    0 4.4 0   0 0 4.4     $ Support
62 BOX 95.6 -45.6 -4.9  4.4 0 0   0 91.2 0  0 0 4.4     $ Support
63 BOX -100 -2.2 -4.9   4.4 0 0   0 4.4 0   0 0 -85.5   $ Leg
64 BOX -50 -2.2 -4.9    4.4 0 0   0 4.4 0   0 0 -85.5   $ Leg
65 BOX 45.6 -2.2 -4.9   4.4 0 0   0 4.4 0   0 0 -85.5   $ Leg
66 BOX 95.6 -2.2 -4.9   4.4 0 0   0 4.4 0   0 0 -85.5   $ Leg
67 BOX -50 -100 -4.9    4.4 0 0   0 4.4 0   0 0 -85.5   $ Leg
68 BOX 45.6 -100 -4.9   4.4 0 0   0 4.4 0   0 0 -85.5   $ Leg
69 BOX -50 95.6 -4.9    4.4 0 0   0 4.4 0   0 0 -85.5   $ Leg
70 BOX 45.6 95.6 -4.9   4.4 0 0   0 4.4 0   0 0 -85.5   $ Leg
c
c   Floor
c ~~~~~~~~~~~~~~~~~
```

```
97 BOX -300 -300 -120.9 600 0 0  0 600 0  0 0 30.5
c
c   Enviroment
c ~~~~~~~~~~~~~~~~
98 BOX -350 -350  0     700 0 0   0 700 0   0 0 150
99 BOX -350 -350 -150   700 0 0   0 700 0   0 0 150

c
~~~~~~~~~~~~~~~~~~~~~~~~~~~~~~~~~~~~~~~~~~~~~~~~~~~~~~~~~~~~~~~~~~~~~~~~~~~~~~~
c   DATA
c
~~~~~~~~~~~~~~~~~~~~~~~~~~~~~~~~~~~~~~~~~~~~~~~~~~~~~~~~~~~~~~~~~~~~~~~~~~~~~~~
TR1 30 0 13                           $ Move the Detectors
TR2 0 0 0   -1 0 0   0 1 0   0 0 1
TR3 0 0 0   0 -1 0   1 0 0   0 0 1
TR4 0 0 0   0 1 0   -1 0 0   0 0 1
TR5 30 0 0                            $ Move the Lead
TR6 0 0 17.5484                       $ Move the MOX
c
~~~~~~~~~~~~~~~~~~~~~~~~~~~~~~~~~~~~~~~~~~~~~~~~~~~~~~~~~~~~~~~~~~~~~~~~~~~~~~~
c   PHYSICS
c
~~~~~~~~~~~~~~~~~~~~~~~~~~~~~~~~~~~~~~~~~~~~~~~~~~~~~~~~~~~~~~~~~~~~~~~~~~~~~~~
MODE n
PHYS:N J 20.
PHYS:P 0 1 1
CUT:P 2J 0
c
~~~~~~~~~~~~~~~~~~~~~~~~~~~~~~~~~~~~~~~~~~~~~~~~~~~~~~~~~~~~~~~~~~~~~~~~~~~~~~~
c   SOURCE
c
~~~~~~~~~~~~~~~~~~~~~~~~~~~~~~~~~~~~~~~~~~~~~~~~~~~~~~~~~~~~~~~~~~~~~~~~~~~~~~~
sdef pos=0 0 0 axs=0 0 1 rad=d1 ext=d2 TR=6 erg=d3
sc1  Source radius (inner outer)
si1  0 4.14
sp1  -21 1
sc2  source height
si2  -15.8482 7.9228
sp2  -21 0
si3  L 3 4 38 39 40 41
sp3  0.3736 0.0455 0.0682 0.0902 0.1404 0.2822
IPOL 99 1 2 1 J 1 4 6 106 306 406
NPS 33656840 $ 52337 rxn/s, 14 hr meas is 3029115600 rxn/s, 90 seeds
FILES 21 DUMN1
DBCN
PRDMP 2J 1
c
~~~~~~~~~~~~~~~~~~~~~~~~~~~~~~~~~~~~~~~~~~~~~~~~~~~~~~~~~~~~~~~~~~~~~~~~~~~~~~~
c   MATERIALS
c
~~~~~~~~~~~~~~~~~~~~~~~~~~~~~~~~~~~~~~~~~~~~~~~~~~~~~~~~~~~~~~~~~~~~~~~~~~~~~~~
c
c   MOX
c ~~~~~~~~~~~~~~~~~
c    Mox Fuel
```

```
c
~~~~~~~~~~~~~~~~~~~~~~~~~~~~~~~~~~~~~~~~~~~~~~~~~~~~~~~~~~~~~~~~~~~~~~~~~~~~~~~
~m1    8016.60c -0.16443  94238.42c -0.00024   94239.60c -0.11062
      94240.60c -0.04650  94241.60c -0.000183  94242.60c -0.00334
      95241.61c -0.00490  92235.60c -0.00474   92238.60c -0.66330
c
c   Aluminium  p=-2.7
c ~~~~~~~~~~~~~~~~~
m2   13027.70c -0.9653
     12000.60c -0.0100
     26000.55c -0.0070
     14000.60c -0.0060
     29000.50c -0.0028
     30000.42c -0.0025
     24000.50c -0.0020
     25055.70c -0.0015
     22000.51c -0.0015
c
c    concrete (ordinary with ENDF-VI)  ,d=-2.35       ,PRS 374
c ~~~~~~~~~~~~~~~~~
m3    1001.60c -0.005558    8016.60c -0.498076    11023.60c -0.017101
      12000.60c -0.002565   13027.60c -0.045746   14000.60c -0.315092
      16000.60c -0.001283   19000.60c -0.019239   20000.60c -0.082941
      26054.60c -0.000707   26056.60c -0.011390   26057.60c -0.000265
      26058.60c -0.000036
c
c    air (US S. Atm at sea level) d=-.001225    ,HC&P 14-19
c ~~~~~~~~~~~~~~~~~
m4   7014.60c -0.755636    8016.60c -0.231475   18000.59c -0.012889
c
c    EJ-309 liquid scintillator d=-0.916
c ~~~~~~~~~~~~~~~~~
m5     1001      0.548          nlib = 60c
       6000      0.452          nlib = 60c
c
c    Nitrogen    d=-0.001
c ~~~~~~~~~~~~~~~~~
c m6      7014  1                nlib = 60c
c
c    Pyrex    d=-2.23
c ~~~~~~~~~~~~~~~~~
m7      5011  -0.040064         nlib = 60c
        8016  -0.539562         nlib = 60c
       11023  -0.028191         nlib = 60c
       13027  -0.011644         nlib = 60c
       14000  -0.377220         nlib = 60c
       19000  -0.003321         nlib = 60c
c
c    MU-Metal   d=-8.747
c ~~~~~~~~~~~~~~~~~
m8     28000.50c 0.8
       42000     0.05           nlib = 60c
       14000     0.005          nlib = 60c
       29063     0.0002         nlib = 60c
       26056     0.1448         nlib = 60c
c
c    Lead     g=-11.34
```

```
c ~~~~~~~~~~~~~~~~~
m9   82000.50c 1
c    Steel
c ~~~~~~~~~~~~~~~~~
m10   26000.55c -0.6950
     24000.50c -0.1900
     28000.50c -0.0950
     25055.51c -0.0200
c
c
~~~~~~~~~~~~~~~~~~~~~~~~~~~~~~~~~~~~~~~~~~~~~~~~~~~~~~~~~~~~~~~~~~~~~~~~~~~~~~~
c   TALLIES
c
~~~~~~~~~~~~~~~~~~~~~~~~~~~~~~~~~~~~~~~~~~~~~~~~~~~~~~~~~~~~~~~~~~~~~~~~~~~~~~~
c
c   Face of Detector 1
c ~~~~~~~~~~~~~~~~~
F11:n 2
E11 0.640 100
C11 0 1
FS11 -9
F21:p 2
E21 0 99i 10
C21 0 1
FS21 -9
c
c   Face of Detector 2
c ~~~~~~~~~~~~~~~~~
F31:n 101002
E31 0.640 100
C31 0 1
FS31 -9
F41:p 2
E41 0 99i 10
C41 0 1
FS41 -9
```

INL Mixed-Oxide Fuel Example

```
Sample 127 Aged -- 90 pins -- 40 cm -- 2 in Pb shielding
c CELL CARDS
c MOX Fuel Can
  4    2  -2.7    -71 72          IMP:N,P=1
c MOX Fuel Rods
  5    3  -9.45068   -82          IMP:N,P=1   $ fuel core
  6    4  -6.5    -81 82          IMP:N,P=1   $ fuel cladding
  7    LIKE 5 BUT TRCL=1
  8    LIKE 5 BUT TRCL=2
  9    LIKE 5 BUT TRCL=3
  10   LIKE 5 BUT TRCL=4
  11   LIKE 5 BUT TRCL=5
  12   LIKE 5 BUT TRCL=6
  13   LIKE 5 BUT TRCL=7
  14   LIKE 5 BUT TRCL=8
  15   LIKE 5 BUT TRCL=9
  16   LIKE 5 BUT TRCL=10
  17   LIKE 5 BUT TRCL=11
  18   LIKE 5 BUT TRCL=12
  19   LIKE 5 BUT TRCL=13
  20   LIKE 5 BUT TRCL=14
  21   LIKE 5 BUT TRCL=15
  22   LIKE 5 BUT TRCL=16
  23   LIKE 5 BUT TRCL=17
  24   LIKE 5 BUT TRCL=18
  25   LIKE 5 BUT TRCL=19
  26   LIKE 5 BUT TRCL=20
  27   LIKE 5 BUT TRCL=21
  28   LIKE 5 BUT TRCL=22
  29   LIKE 5 BUT TRCL=23
  30   LIKE 5 BUT TRCL=24
  31   LIKE 5 BUT TRCL=25
  32   LIKE 5 BUT TRCL=26
  33   LIKE 5 BUT TRCL=27
  34   LIKE 5 BUT TRCL=28
  35   LIKE 5 BUT TRCL=29
  36   LIKE 5 BUT TRCL=30
  37   LIKE 5 BUT TRCL=31
  38   LIKE 5 BUT TRCL=32
  39   LIKE 5 BUT TRCL=33
  40   LIKE 5 BUT TRCL=34
  41   LIKE 5 BUT TRCL=35
  42   LIKE 5 BUT TRCL=36
  43   LIKE 5 BUT TRCL=37
  44   LIKE 5 BUT TRCL=38
  45   LIKE 5 BUT TRCL=39
  46   LIKE 5 BUT TRCL=40
  47   LIKE 5 BUT TRCL=41
  48   LIKE 5 BUT TRCL=42
  49   LIKE 5 BUT TRCL=43
  50   LIKE 5 BUT TRCL=44
  51   LIKE 5 BUT TRCL=45
  52   LIKE 5 BUT TRCL=46
  53   LIKE 5 BUT TRCL=47
```

```
54   LIKE 5 BUT TRCL=48
55   LIKE 5 BUT TRCL=49
56   LIKE 5 BUT TRCL=50
57   LIKE 5 BUT TRCL=51
58   LIKE 5 BUT TRCL=52
59   LIKE 5 BUT TRCL=53
60   LIKE 5 BUT TRCL=54
61   LIKE 5 BUT TRCL=55
62   LIKE 5 BUT TRCL=56
63   LIKE 5 BUT TRCL=57
64   LIKE 5 BUT TRCL=58
65   LIKE 5 BUT TRCL=59
66   LIKE 5 BUT TRCL=60
67   LIKE 5 BUT TRCL=61
68   LIKE 5 BUT TRCL=62
69   LIKE 5 BUT TRCL=63
70   LIKE 5 BUT TRCL=64
71   LIKE 5 BUT TRCL=65
72   LIKE 5 BUT TRCL=66
73   LIKE 5 BUT TRCL=67
74   LIKE 5 BUT TRCL=68
75   LIKE 5 BUT TRCL=69
76   LIKE 5 BUT TRCL=70
77   LIKE 5 BUT TRCL=71
78   LIKE 5 BUT TRCL=72
79   LIKE 5 BUT TRCL=73
80   LIKE 5 BUT TRCL=74
81   LIKE 5 BUT TRCL=75
82   LIKE 5 BUT TRCL=76
83   LIKE 5 BUT TRCL=77
84   LIKE 5 BUT TRCL=78
85   LIKE 5 BUT TRCL=79
86   LIKE 5 BUT TRCL=80
87   LIKE 5 BUT TRCL=81
88   LIKE 5 BUT TRCL=82
89   LIKE 5 BUT TRCL=83
90   LIKE 5 BUT TRCL=84
91   LIKE 5 BUT TRCL=85
92   LIKE 5 BUT TRCL=86
93   LIKE 5 BUT TRCL=87
94   LIKE 5 BUT TRCL=88
95   LIKE 5 BUT TRCL=89
106  LIKE 6 BUT TRCL=1
107  LIKE 6 BUT TRCL=2
108  LIKE 6 BUT TRCL=3
109  LIKE 6 BUT TRCL=4
110  LIKE 6 BUT TRCL=5
111  LIKE 6 BUT TRCL=6
112  LIKE 6 BUT TRCL=7
113  LIKE 6 BUT TRCL=8
114  LIKE 6 BUT TRCL=9
115  LIKE 6 BUT TRCL=10
116  LIKE 6 BUT TRCL=11
117  LIKE 6 BUT TRCL=12
118  LIKE 6 BUT TRCL=13
119  LIKE 6 BUT TRCL=14
120  LIKE 6 BUT TRCL=15
```

```
121  LIKE 6 BUT TRCL=16
122  LIKE 6 BUT TRCL=17
123  LIKE 6 BUT TRCL=18
124  LIKE 6 BUT TRCL=19
125  LIKE 6 BUT TRCL=20
126  LIKE 6 BUT TRCL=21
127  LIKE 6 BUT TRCL=22
128  LIKE 6 BUT TRCL=23
129  LIKE 6 BUT TRCL=24
130  LIKE 6 BUT TRCL=25
131  LIKE 6 BUT TRCL=26
132  LIKE 6 BUT TRCL=27
133  LIKE 6 BUT TRCL=28
134  LIKE 6 BUT TRCL=29
135  LIKE 6 BUT TRCL=30
136  LIKE 6 BUT TRCL=31
137  LIKE 6 BUT TRCL=32
138  LIKE 6 BUT TRCL=33
139  LIKE 6 BUT TRCL=34
140  LIKE 6 BUT TRCL=35
141  LIKE 6 BUT TRCL=36
142  LIKE 6 BUT TRCL=37
143  LIKE 6 BUT TRCL=38
144  LIKE 6 BUT TRCL=39
145  LIKE 6 BUT TRCL=40
146  LIKE 6 BUT TRCL=41
147  LIKE 6 BUT TRCL=42
148  LIKE 6 BUT TRCL=43
149  LIKE 6 BUT TRCL=44
150  LIKE 6 BUT TRCL=45
151  LIKE 6 BUT TRCL=46
152  LIKE 6 BUT TRCL=47
153  LIKE 6 BUT TRCL=48
154  LIKE 6 BUT TRCL=49
155  LIKE 6 BUT TRCL=50
156  LIKE 6 BUT TRCL=51
157  LIKE 6 BUT TRCL=52
158  LIKE 6 BUT TRCL=53
159  LIKE 6 BUT TRCL=54
160  LIKE 6 BUT TRCL=55
161  LIKE 6 BUT TRCL=56
162  LIKE 6 BUT TRCL=57
163  LIKE 6 BUT TRCL=58
164  LIKE 6 BUT TRCL=59
165  LIKE 6 BUT TRCL=60
166  LIKE 6 BUT TRCL=61
167  LIKE 6 BUT TRCL=62
168  LIKE 6 BUT TRCL=63
169  LIKE 6 BUT TRCL=64
170  LIKE 6 BUT TRCL=65
171  LIKE 6 BUT TRCL=66
172  LIKE 6 BUT TRCL=67
173  LIKE 6 BUT TRCL=68
174  LIKE 6 BUT TRCL=69
175  LIKE 6 BUT TRCL=70
176  LIKE 6 BUT TRCL=71
177  LIKE 6 BUT TRCL=72
```

```
  178  LIKE 6 BUT TRCL=73
  179  LIKE 6 BUT TRCL=74
  180  LIKE 6 BUT TRCL=75
  181  LIKE 6 BUT TRCL=76
  182  LIKE 6 BUT TRCL=77
  183  LIKE 6 BUT TRCL=78
  184  LIKE 6 BUT TRCL=79
  185  LIKE 6 BUT TRCL=80
  186  LIKE 6 BUT TRCL=81
  187  LIKE 6 BUT TRCL=82
  188  LIKE 6 BUT TRCL=83
  189  LIKE 6 BUT TRCL=84
  190  LIKE 6 BUT TRCL=85
  191  LIKE 6 BUT TRCL=86
  192  LIKE 6 BUT TRCL=87
  193  LIKE 6 BUT TRCL=88
  194  LIKE 6 BUT TRCL=89
c Air inside MOX fuel can  (within the inner three rings of pins)
  201  5 -0.001205  -74      #5   #6   #7   #8   #9  #10  #11
                             #12 #106 #107 #108 #109 #110 #111
             #13  #14  #15  #16  #17  #18  #19  #20  #21  #22
             #23  #24  #25  #26  #27  #28  #29  #30  #31  #32
             #33  #34  #35  #36  #37  #38  #39  #40  #41  #42
            #112 #113 #114 #115 #116 #117 #118 #119 #120 #121
            #122 #123 #124 #125 #126 #127 #128 #129 #130 #131
            #132 #133 #134 #135 #136 #137 #138 #139 #140 #141 IMP:N,P=1
c Air inside MOX fuel can  (within the second to last ring of pins)
  203  5 -0.001205  -73 74  #43  #44  #45  #46  #47  #48  #49
             #50  #51  #52  #53  #54  #55  #56  #57  #58  #59
             #60  #61  #62  #63  #64  #65  #66 #142 #143 #144
            #145 #146 #147 #148 #149 #150 #151 #152 #153 #154
            #155 #156 #157 #158 #159 #160 #161 #162 #163 #164
            #165                                              IMP:N,P=1
c Air inside MOX fuel can  (within the outer ring of pins)
  204  5 -0.001205  -72 73  #67  #68  #69  #70  #71  #72  #73
             #74  #75  #76  #77  #78  #79  #80  #81  #82  #83
             #84  #85  #86  #87  #88  #89  #90  #91  #92  #93
             #94  #95 #166 #167 #168 #169 #170 #171 #172 #173
            #174 #175 #176 #177 #178 #179 #180 #181 #182 #183
            #184 #185 #186 #187 #188 #189 #190 #191 #192 #193
            #194                                              IMP:N,P=1
c Detector active liquid volumes (EJ-309)
  301  1   -0.964  -31    IMP:N,P=1
  302  1   -0.964  -32    IMP:N,P=1
  303  1   -0.964  -33    IMP:N,P=1
  304  1   -0.964  -34    IMP:N,P=1
c Shielding (lead)
  401  6   -11.34  -41    IMP:N,P=1
  402  6   -11.34  -42    IMP:N,P=1
  403  6   -11.34  -43    IMP:N,P=1
  404  6   -11.34  -44    IMP:N,P=1
  405  6   -11.34  -45    IMP:N,P=1
  406  6   -11.34  -46    IMP:N,P=1
  407  6   -11.34  -47    IMP:N,P=1
  408  6   -11.34  -48    IMP:N,P=1
c Table (plywood)
  501  7   -0.4785 -51    IMP:N,P=1
```

```
  502  7   -0.4785 -52    IMP:N,P=1
  503  7   -0.4785 -53    IMP:N,P=1
  504  7   -0.4785 -54    IMP:N,P=1
c Source stand (styrofoam)
  601  8   -0.016  -61    IMP:N,P=1
c Bounding sphere
  999  5 -1.205E-3 -99 31 32 33 34 41 42 43 44 45 46 47 48
                       51 52 53 54 61 71 IMP:N,P=1
c Outside universe
  9999 0            99      IMP:N,P=0
c END CELL CARDS-BLANK LINE FOLLOWS

c SURFACE CARDS
c Detector active volumes (det 1,2,3,5)
  31   RCC   40   0     0   12.7   0     0  6.35
  32   RCC  -40   0     0  -12.7   0     0  6.35
  33   RCC   0    0   -40    0     0 -12.7  6.35
  34   RCC   0    0    40    0     0  12.7  6.35
c Shielding blocks
  41   RPP    34.42  39.50  -10.16  10.16  -10.16  10.16
  42   RPP   -39.50 -34.42  -10.16  10.16  -10.16  10.16
  43   RPP   -10.16  10.16  -10.16  10.16  -39.50 -34.42
  44   RPP   -10.16  10.16  -10.16  10.16   34.42  39.50
  45   RPP    29.34  39.50  -15.24 -10.16  -10.16  10.16
  46   RPP   -39.50 -29.34  -15.24 -10.16  -10.16  10.16
  47   RPP   -10.16  10.16  -15.24 -10.16  -39.50 -29.34
  48   RPP   -10.16  10.16  -15.24 -10.16   29.34  39.50
c Table
  51   RPP      0.00  152.40   -15.875  -15.24    -43.18   43.18
  52   RPP   -152.40    0.00   -15.875  -15.24    -43.18   43.18
  53   RPP    -43.18   43.18   -15.875  -15.24   -195.58  -43.18
  54   RPP    -43.18   43.18   -15.875  -15.24     43.18  195.58
c Source stand
  61   RPP     -7.62  7.62  -15.24 -7.77875  -7.62  7.62
c Can containing fuel rods (1/16in thick)
  71   RCC     0 -7.77875 0   0 17.78   0   5.56
  72   RCC     0 -7.62    0   0 17.4625 0   5.40
  73   RCC     0 -7.62    0   0 17.4625 0   4.23
  74   RCC     0 -7.62    0   0 17.4625 0   3.26626
c MOX Fuel Rods
  81   RCC  0  -7.62     0    0  15.24   0   0.47624
  82   RCC  0  -7.58952  0    0  15.179  0   0.424577
c Bounding sphere
  99   SO 250
c END SURFACE CARDS-BLANK LINE FOLLOWS

C DATA CARDS
C
C --------Transformations------------
C
TR1     0.9525 0.00000        0
TR2    0.47625 0.00000 0.824889
TR3    -0.9525 0.00000        0
TR4   -0.47625 0.00000 0.824889
TR5    0.47625 0.00000 -0.82489
TR6   -0.47625 0.00000 -0.82489
TR7   1.786963 0.00000 0.478815
```

```
TR8   1.308148 0.00000 1.308148
TR9   0.478815 0.00000 1.786963
TR10  -1.78696 0.00000 0.478815
TR11  -1.30815 0.00000 1.308148
TR12  -0.47882 0.00000 1.786963
TR13  1.786963 0.00000 -0.47882
TR14  1.308148 0.00000 -1.30815
TR15  0.478815 0.00000 -1.78696
TR16  -1.78696 0.00000 -0.47882
TR17  -1.30815 0.00000 -1.30815
TR18  -0.47882 0.00000 -1.78696
TR19      2.79 0.00000        0
TR20  2.621742 0.00000 0.954236
TR21  2.137264 0.00000 1.793377
TR22     1.395 0.00000 2.416211
TR23  0.484478 0.00000 2.747614
TR24     -2.79 0.00000        0
TR25  -2.62174 0.00000 0.954236
TR26  -2.13726 0.00000 1.793377
TR27    -1.395 0.00000 2.416211
TR28  -0.48448 0.00000 2.747614
TR29  2.621742 0.00000 -0.95424
TR30  2.137264 0.00000 -1.79338
TR31     1.395 0.00000 -2.41621
TR32  0.484478 0.00000 -2.74761
TR33  -2.62174 0.00000 -0.95424
TR34  -2.13726 0.00000 -1.79338
TR35    -1.395 0.00000 -2.41621
TR36  -0.48448 0.00000 -2.74761
TR37   3.71792 0.00000  0.48947
TR38   3.46455 0.00000  1.43506
TR39   2.97508 0.00000  2.28286
TR40   2.28286 0.00000  2.97508
TR41   1.43506 0.00000  3.46455
TR42   0.48947 0.00000  3.71792
TR43  -3.71792 0.00000  0.48947
TR44  -3.46455 0.00000  1.43506
TR45  -2.97508 0.00000  2.28286
TR46  -2.28286 0.00000  2.97508
TR47  -1.43506 0.00000  3.46455
TR48  -0.48947 0.00000  3.71792
TR49   3.71792 0.00000 -0.48947
TR50   3.46455 0.00000 -1.43506
TR51   2.97508 0.00000 -2.28286
TR52   2.28286 0.00000 -2.97508
TR53   1.43506 0.00000 -3.46455
TR54   0.48947 0.00000 -3.71792
TR55  -3.71792 0.00000 -0.48947
TR56  -3.46455 0.00000 -1.43506
TR57  -2.97508 0.00000 -2.28286
TR58  -2.28286 0.00000 -2.97508
TR59  -1.43506 0.00000 -3.46455
TR60  -0.48947 0.00000 -3.71792
TR61   4.71000 0.00000  0.00000
TR62   4.60708 0.00000  0.97926
TR63   4.30280 0.00000  1.91573
TR64   3.81047 0.00000  2.76847
```

```
TR65   3.15161 0.00000  3.50021
TR66   2.35500 0.00000  4.07898
TR67   1.45547 0.00000  4.47948
TR68   0.49233 0.00000  4.68420
TR69  -4.71000 0.00000  0.00000
TR70  -4.60708 0.00000  0.97926
TR71  -4.30280 0.00000  1.91573
TR72  -3.81047 0.00000  2.76847
TR73  -3.15161 0.00000  3.50021
TR74  -2.35500 0.00000  4.07898
TR75  -1.45547 0.00000  4.47948
TR76   4.60708 0.00000 -0.97926
TR77   4.30280 0.00000 -1.91573
TR78   3.81047 0.00000 -2.76847
TR79   3.15161 0.00000 -3.50021
TR80   2.35500 0.00000 -4.07898
TR81   1.45547 0.00000 -4.47948
TR82   0.49233 0.00000 -4.68420
TR83  -4.60708 0.00000 -0.97926
TR84  -4.30280 0.00000 -1.91573
TR85  -3.81047 0.00000 -2.76847
TR86  -3.15161 0.00000 -3.50021
TR87  -2.35500 0.00000 -4.07898
TR88  -1.45547 0.00000 -4.47948
TR89  -0.49233 0.00000 -4.68420
C
C -------Source---------------------------
C
  MODE   N
  NPS    1.25E8
  SDEF   ERG=D1 CEL=D2 POS=0 0 0 AXS=0 1 0 RAD=D3 EXT=D4 EFF=1e-4
  SI1 L  3      4      38     39     40     41
  SP1    0.3624 0.0090 0.0583 0.2183 0.1082 0.2439
  SI2 L  5    7  87I  95
  SP2    0.01111    89R
  SI3    0       5.4
  SI4   -7.62    7.62
  SP4    0       1
C
C -------PoliMi---------------------------
C
  IPOL     99 1 2 1 J 1 4 301 302 303 304       $Mixed source
  RDUM     0.001 0.001
  FILES    21 DUMN1
  DBCN
  PRDMP 2J 1
c Analog physics
  PHYS:N   J 20
  PHYS:P   0 1 1
  CUT:N    2J 0
  CUT:P    2J 0
  PRINT    10 40 50 110 126 140
c MATERIALS SPECIFICATION
c Liquid scintillator EJ-309
  M1  PLIB=02p  NLIB=60c
     1001  0.5554
     6000  0.4446
```

```
c Aluminum
  M2  PLIB=02p  NLIB=60c
     13027  1.0
c Aged Pu-O fuel core
  M3  PLIB=02p  NLIB=60c
     92235 -0.00168 92238 -0.74774 92234     -0.00002
     93237 -0.00002 94238 -0.00009 94239     -0.11416 94240     -
0.01528
     94241 -0.00049 94242 -0.00022 95241.04p -0.00181 08016     -
0.11846
c Fuel pin cladding
  M4  PLIB=02p  NLIB=60c
     26056 -0.695319   24052 -0.185391   28058 -0.096529
     25055 -0.012833   14000 -0.004681   27059 -0.000888
     42000 -0.000565   29063 -0.000565   22000 -0.000484
     13027 -0.000323    6000 -0.000242   73181 -0.000161
     15031 -0.000161    4009 -0.000081   16000 -0.000081
c Air
  M5  PLIB=02p  NLIB=60c
      7014 -0.755000    8016 -0.232000   18000.42c -0.013000
c Lead
  M6  PLIB=02p  NLIB=60c
      82208 1
c Plywood
  M7  PLIB=02p  NLIB=60c
      14000 0.3289  15031 0.0899  16000 0.0949
      17000 0.0112  19000 0.1044  20000 0.3015
      24052 0.0037  22000 0.0025  25055 0.0581
      26056 0.0049
c Styrofoam
  M8  PLIB=02p  NLIB=60c
      1001 1 6000 1
c TALLY SPECIFICATION
  FC11 Neutron fluence crossing the detector faces
  F11:N  31.3
  E11    0 999i 10 19i 20 100
  C11    0 1
  FQ11   E C
```

References

[1] Eisenhower, President Dwight D., "Atoms for Peace (speech)," 8 December 1953. [Online]. Available: <http://www.eisenhower.archives.gov/research/online_documents/atoms_for_peace/Binder13.pdf>.

[2] P. R. Lavoy, "The Enduring Effects of Atoms for Peace," Arms Control Association, December 2003. [Online]. Available: <http://www.armscontrol.org/act/2003_12/Lavoy> [Accessed 2013].

[3] Depositary Governments: Russian Federation, United Kingdom, United States, *INFCIRC/140: Treaty on the Non-Proliferation of Nuclear Weapons,* International Atomic Energy Agency Publications, 1970.

[4] C. Reed, "The Fallout of a Helium-3 Crisis. Discovery News, Earth News," 21 Feb. 2011. [Online]. Available: <http://news.discovery.com/earth/the-outfall-of-a-helium-3-crisis.htm>. [Accessed 2011].

[5] N.Ensslin, W.C.Harker, M.S.Krick, D.G.Langner, M.M.Pickrell, J.E.Stewart, "Application Guide to Neutron Multiplicity Counting," Los Alamos Report LA-13422-M, 1998.

[6] Industries., Neutron Safeguards Systems - CANBERRA, "Canberra.com," 2000. [Online]. Available: <http://www.canberra.com/products/waste_safeguard_systems/neutron-safeguards-systems.asp>. [Accessed September 2012].

[7] G. Knoll, in *Radiation Detection and Measurement, fourth ed*, New York, Wiley, 2010.

[8] Reilly, Ensslin, Smith, Kreiner, Passive Nondestructive Assay Manual - PANDA, Los Alamos, NM: Safeguards Science and Technology Group at LANL, 1991.

[9] J.F. Lemming, M.E. Anderson, "Selected Measurement Data for Plutonium and Uranium," Mound Laboratory report MLM-3009, 1982.

[10] J. Doyle, "Calorimetry," in *Nuclear Safeguards, Security and Nonproliferation: Achieving Security with Technology and Policy*, Elsevier, 2011, pp. 55-56.

[11] E.Padovani, S.A.Pozzi, S.D.Clarke, E.C.Miller, *MCNPX-PoliMi User's Manual, C00791 NYCP,* Radiation Safety Information Computational Center, Oak Ridge National Laboratory, 2012.

[12] E.C. Miller, A. Poitrasson-Riviere, A. Enqvist, J.L. Dolan, S. Prasad, M.M. Bourne, K. Weinfurther, S.D. Clarke, M. Flaska, S.A. Pozzi, E. Padovani, J.K. Mattingly, *MCNPX-PoliMi Post-Processor (MPPost) Manual, Version 2.1.0,* Radiation Safety Information Computational Center, Oak Ridge National Laboratory, 2012.

[13] S. A. Pozzi, S. D. Clarke, W. Walsh, E. C. Miller, J.L. Dolan, M. Flaska, B. M. Wieger, A. Enqvist, E. Padovani, J. K. Mattingly, D. Chichester, and P. Peerani, "MCNPX-PoliMi for Nuclear Nonproliferation Applications," *Nuclear Instruments and Methods in Physics Research, Section A,* vol. 694, pp. 119-125, 2012.

[14] A. Enqvist, C.C. Lawrence, B.M. Wieger, S.A. Pozzi, T.N. Massey, "Neutron light output response and resolution functions in EJ-309 liquid scintillation detectors," *Nuclear Instruments and Methods in Physics Research Section A,* 2013.

[15] M. Flaska, S. A. Pozzi, "Digital Pulse Shape Analysis for the Capture-Gated Liquid Scintillator BC-523A," *Nuclear Instruments and Methods in Physics Section A,* vol. 577, pp. 654-663, 2007.

[16] Eljen Technologies, “EJ-309 Data Sheet,” 2010. [Online]. Available: <http://www.eljentechnology.com/images/stories/Data_Sheets/Liquid_Scintillators/EJ309%20data%20sheet.pdf>.

[17] St-Gobain Ceramics and Plastics, "BC-523A Data Sheet.," 2008. [Online]. Available: <http://www.detectors.saint-gobain.com/uploadedFiles/SGdetectors/Documents/Product_Data_Sheets/BC523A-Data-Sheet.pdf>.

[18] M. Flaska, M. Faisal, D. D. Wentzloff, S. A. Pozzi, “Influence of Sampling Properties of Fast-waveform Digitizers on Neutron−Gamma-ray, Pulse-shape Discrimination for Organic Scintillation Detectors,” *Nuclear Instruments and Methods in Physics Research Section A*, 2013.

[19] A. C. Kaplan, M. Flaska, A. Enqvist, J. L. Dolan, S. A. Pozzi, "EJ-309 Pulse Shape Discrimination Performance with a High Gamma-Ray-to-Neutron Ratio and Low Threshold," *Nuclear Instrumentation and Methods in Physics, Section A,* vol. TBD, 2013.

[20] A. Enqvist, B. M. Wieger, L. Huang, M. Flaska, and S.A. Pozzi, R. C. Haight, H. Young Lee and C. Yen Wu, "Neutron-Induced ^{235}U Fission Spectrum Measurements Using Liquid Organic Scintillation Detectors," *Physical Review C,* vol. 86, 2012.

[21] C. C. Lawrence, A. Enqvist, M. Flaska, S. A. Pozzi, A.M. Howard, J.J. Kolata, F D. Becchetti, "Response Characterization for an EJ315 Deuterated Organic-Liquid Scintillation Detector for Neutron Spectroscopy," *Nuclear Instrumentation and Methods in Physics, Section A,* vol. TBD, 2013.

[22] M. Flaska, S.A. Pozzi, "Identification of Shielded Neutron Sources with the Liquid Scintillator BC-501A Using a Digital Pulse Shape Discrimination Method," *Nuclear Instruments and Methods in Physics Section A,* vol. 577, pp. 654-663, 2007.

[23] S.A. Pozzi, Y. Xu, T. Zak, S.D. Clarke, M.M. Bourne, M. Flaska, T.J. Downar, P. Peerani, and V. Protopopescu, "Fast Neutron Spectrum Unfolding for Nuclear Nonproliferation and Safeguards Applications," *Il Nuovo Cimento, vol. 33, N. 1, 2010.*, 2010.

[24] R. T. Klann, B. D. Austin, S. E. Aumeier, and D. N. Olsen, "Inventory of Special Nuclear Materials from the Zero Power Physics Reactor," Nuclear Technology Division at Argonne National Laboratory-West. ANL-NT-176., 2001.

[25] B. N. Laboratory, "Evaluated Nuclear Data File/B-VII.1," [Online]. Available: http://www.nndc.bnl.gov/sigma/. [Accessed 2011].

[26] S. D. Clarke, M. Flaska, S. A. Pozzi, and P. Peerani, "Neutron and Gamma-Ray Cross-Correlation Measurements of Plutonium-Oxide Powder," *Nuclear Instruments and Methods in Physics Section A,* vol. 604, pp. 618-623, 2009.

[27] C. Wagemans, in *The Nuclear Fission Process*, Boca Rotan, FL, CRC Press, 1991, pp. 492-510.

[28] H.H. Knitter, C. Budtz-Jorgensen, "Simultaneous Investigation of Fission Fragments and Neutrons in Cf-252 (SF)," *Nuclear Physics A,* vol. 490, pp. 307-328, 1988.

[29] R.C. Runkle, D.L. Chichester, S.J. Thompson, "Rattling nucleons: New developments in active interrogation of special nuclear material," *Nuclear Instruments and Methods in Physics Research Section A,* vol. 663, pp. 75-95, 2012.

[30] D. Cester, G. Nebbia, L. Stevanato, G Viesti, F. Neri, S. Petrucci, S. Selmi, C. Tintori, P. Peerani, A. Tomanin, "Special Nuclear Material Detection with a Mobile Multi-Detector System," *Nuclear Instruments and Methods in Physics Research Section A,* vol. 663, p. 55063, 2012.

[31] E. Padovani, P. Peerani, M. Da Ros and S. A. Pozzi, "Simulation of correlated counts from an Am–Li source," *Nuclear Instruments and Methods in Physics Research A,* vol. 557, pp. 599-606, 2006.

[32] A. Enqvist, M. Flaska, J. L. Dolan, D. L. Chichester, and S. A. Pozzi, "A Combined Neutron and Gamma Ray Multiplicity Counter Based on Liquid Scintillation Detectors," *Nuclear Instruments and Methods in Physics Section A,* vol. 652, pp. 48-51, 2011.

[33] J. L. Dolan, M. Flaska, S. A. Pozzi, D. L. Chichester, "Passive measurements of mixed-oxide fuel for nuclear nonproliferation," *Nuclear Instruments and Methods in Physics Section A,* vol. 703, pp. 102-108, 2013.

[34] K. Frame, W. Clay, T. Elmont, E. Esch, P. Karpius, D. MacArthur, E. McKigney, P. Santi, M. Smith, J. Thron, R. Williams, "Development of a liquid scintillator neutron multiplicity counter (LSMC)," *Nuclear Instruments and Methods in Physics Section A,* vol. 579, pp. 192-195, 2007.

[35] N. Dytlewski, N. Ensslin, J.W. Bolderman, "A Neutron Multiplicity Counter for Plutonium Assay," *Nuclear Science and Engineering,* vol. 104, pp. 301-313, 1990.

[36] International Atomic Energy Agency, “International Safeguards Glossary,” 2001.

[37] Industries., Neutron Safeguards Systems - CANBERRA, " Model JCC-31 High Level Neutron Coincidence Counter," 2009. [Online]. Available: <http://www.canberra.com/products/waste_safeguard_systems/neutron-safeguards-systems.asp?Accordion1=2 >. [Accessed April 2013].

[38] S. Gaurdini, “Performance values for nondestructive assay (NDA) techniques applied to safeguards: The 2002 evaluation by the Esarda NDA working group,” ESARDA Bulletin #32, 2004.